

**QUANTIFICATION OF MARINE SEDIMENT PROPERTIES FROM
PLANAR AND VOLUMETRIC PORE GEOMETRIES**

A Dissertation

**Submitted to the Graduate Faculty of the
Louisiana State University and
Agricultural and Mechanical College
in partial fulfillment of the
Requirements for the degree of
Doctor of Philosophy**

in

The Department of Oceanography and Coastal Sciences

by

Allen H. Reed

B.S., Humboldt State University, 1996

M.S., University of Southern Mississippi, 1999

May 2004

DEDICATION

To Frank Koopman for his ingenuity, his knack to make things work, and his ability to see the potential in the scrap pile, and for fine conversations. To Duncan Goldthwaite for his expressed love of the mountains, geology, history, a good beer, and a fine conversation. To Bubba (Edgar Poe Symmes) for his unwavering love of order, fishing, and a fine conversation. To all three men for their enthusiastic and unwavering support.

To Cathy and Sarah who rode this one out with me.

To Catherine Hagerman Reed and to Chester Wilson Ruland who left us before we were ready and seemingly way too soon.

ACKNOWLEDGEMENTS

I would like to extend a special thanks to my committee chair, Jaye E. Cable and to my committee co-chair, Clinton S. Willson who shared CT time at Argonne, devised strategies to evaluate CT images, and promoted image quality, and much needed criticism. CW and Karsten Thompson focused on the “next step”. I am grateful for the work of committee members Jeff Nunn, Samuel J. Bentley, Oscar K. Huh, Lawrence Rouse, Michael D. Richardson, and Dawn L. Lavoie. Thanks go to Eric Thorsos for a critical review of chapter 3. Paul Elmore provided verification for error estimates with a standard propagation of error analysis. The Naval Research Laboratory divers M. D. Richardson, Ricky I. Ray, Kevin B. Briggs, and Dan L. Lott collected samples. Peter Fleischer aided with resin impregnation. The R/V *Seward Johnson* crew provided field support. Avrami Grader established a baseline for image quality. Mark Rivers at GSECARS aided in CT data collection and with data processing. K. B. Briggs provided physical property measurements for porosity, grain size, permeability, and hydraulic conductivity. Nathaniel Plant provided spectral analysis. KK Mohanty set up the EMT analysis. Riyadh Al-Raoush did 3D pore size analysis in chapter 4. Les Butler and Kyungmin Ham aided with post-processing of CT volumes. Stephen Theophanis, Charles Megnin, and Dennis Lindwall with Matlab, maps, and Linux issues. Use of the Advanced Photon Source was supported by the U. S. Department of Energy, Office of Science, Office of Basic Energy Sciences, under Contract No. W-31-109-Eng-38. IEEE Oceanic Engineering. This work was funded by Jeffrey Simmen, Program Manager, under Ocean Acoustics Program of the Office of Naval Research. Thanks to Dr. Herbert Eppert and Naval Research Laboratory and support from PE#0601153N.

TABLE OF CONTENTS

DEDICATION	ii
ACKNOWLEDGEMENTS	iii
LIST OF TABLES	vi
LIST OF FIGURES	vii
ABSTRACT	xi
CHAPTER 1. INTRODUCTION	1
1.1 Importance of Porosity, Permeability, and Pore Geometry in Sands	1
1.2 Bulk Properties of Sand	4
1.3 Network Models	5
1.4 X-ray Generated Images	11
1.5 Current Research and Dissertation Objectives	15
CHAPTER 2. MATERIALS AND METHODS	17
2.1 Marine Sands: Sample Sites, Collection, Characteristics, and Preservation	17
2.1.1 Geologic Settings and Sediment Characteristics	17
2.1.2 Sample Collection and Analysis	20
2.1.3 Resin Impregnation to Preserve <i>In Situ</i> Pore Geometry	23
2.2 Image Collection and Analysis	24
2.2.1 Image Collection	24
2.2.2 Two-dimensional Image Analysis	25
2.2.2 Three-dimensional Image Analysis	26
CHAPTER 3. POROSITY, PERMEABILITY, AND HYDRAULIC CONDUCTIVITY FOR A SILICICLASTIC MARINE SAND: A COMPARISON OF DIRECT MEASUREMENTS AND IMAGE ANALYSIS	28
3.1 Introduction	28
3.2 Porometric Property Predictions from 2D Images	29
3.3 Image Analysis and Predictions from Pore Geometry	33
3.4 Effective Medium Theory for Permeability Predictions	36
3.5 Results	40
3.5.1 Traditional Measurements	40
3.5.2 Predictions from Image Analysis	41
3.6 Discussion	47
3.7 Summary and Conclusions	56

CHAPTER 4. PORE SIZE DISTRIBUTIONS, TOPOLOGICAL CHARACTERISTICS, AND PERMEABILITY PREDICTIONS FROM SYNCHROTRON X-RAY TOMOGRAPHIC IMAGES OF A MARINE SAND: INFLUENCE OF IMAGE DIMENSIONS AND RESOLUTION	58
4.1 Introduction.....	58
4.2 Sample Characteristics and Sample Analysis.....	64
4.3 Preparation of the Sample for CT Analysis	65
4.4 Pore Geometry Characterization and Effective Permeability Predictions	67
4.4.1 Two- and Three-dimensional Characterization of Pore Geometry	67
4.4.2 Permeability Predictions by Traditional and EMT Techniques.....	67
4.5 Results	68
4.5.1 Direct Measurements.....	68
4.5.2 Pore Geometry, Topology, and Physical Properties from Image Analysis	69
4.5.2.1 Homogeneity and Isotropy	69
4.5.2.2 Two-dimensional Pore Geometry and Topology	69
4.5.2.3 Three-dimensional Pore Geometry and Topology	77
4.5.2.4 Permeability Predictions from Physical Properties	81
4.6 Discussion	81
4.7 Conclusions	89
 CHAPTER 5. CONDUCTANCE OF GEOMETRICALLY REALISTIC PORE THROATS	 90
5.1 Introduction.....	90
5.2 Methods.....	94
5.3 Results.....	99
5.4 Discussion.....	109
5.5 Summary	115
 CHAPTER 6. SUMMARY AND CONCLUSIONS.....	 117
 REFERENCES	 119
 APPENDIX: COPYRIGHT PERMISSION	 128
 VITA.....	 129

LIST OF TABLES

Table 3.1 Coordinates of the SAX99 sites for which data are presented	29
Table 3.2. Values of hydraulic conductivity (K), intrinsic permeability (k), and mean grain size from cores collected at four locations within the SAX99 experiment area and at four sediment depths.....	42
Table 3.3. Average values of porosity, permeability, and tortuosity factor from measurements made on sediments from the SAX99 sites	43
Table 4.1. Permeability and porosity measurements from direct and image analysis. Permeability presented in $2D_m$ is determined from the mean of the slice-wise-determined permeabilities and $2D_t$ is determined from all the pore throat and pore body dimensions. Hazen-Shepherd permeability (and hydraulic conductivity) assumes spherical, well sorted grains. Property values were not determined (nd) in some cases. Mean grain size and mean porosity (measured) were used to make the Kozeny-Carman and Hazen-Shepherd predictions. Permeability predictions for $z = 6$ are presented as percent overestimation.....	72
Table 4.2. Pore body and pore throat sizes and distributions for the high- and low-resolution 3D and 2D images (units for the pore sizes are micrometers).....	80
Table 5.1: Average dimensions of pore throat length (T_l), pore throat radii (T_r), and pore body radii (B_r) for quartz and ooid sands collected from the marine environment. Dimensions are in micrometers. Aspect ratios of T_l/T_r , T_r/B_r (also constriction factor (Owen, 1952)), and T_l/B_r from 2D images of quartz and ooid sands.....	99
Table 5.2. Volumetric fluid flow for pore throats of commonly used and representative pore throat shapes was linear over a pressure range that spans that which would be expected for pore throats and laminar fluid flow (10^2 to 10^6 dynes/cm ²).....	107

LIST OF FIGURES

Figure 1.1. Typical configurations of network models are that the pore bodies (circles) and pore throats (connecting lines) are either all the same size (a) or have a range of pore throat radii to incorporate the conductance range that was determined to exist in the porous media (b). 9

Figure 1.2. Pore space in these images display pore paths (white lines (a) and color lines (b)) that are oriented in numerous directions. These depictions indicate that the pore paths in naturally occurring sands are much more complicated the cubic packing models of monosized spheres. That is few if any paths are parallel or perpendicular to another and as such are not represented by a square or cubic lattice. In (b) the color code is red for relatively small pore openings and violet for relatively large pore openings (pore volume and grains are not depicted). In (a) pore area is black, grains are white, and pore paths are depicted by white lines. Dimensions of (a) are $\sim 1100 \times 1100 \mu\text{m}^2$ and of (b) are $\sim 1100 \times 1100 \times 1100 \mu\text{m}^3$ 10

Figure 2.1. Ooid sediment samples were collected south of Bimini, Bahamas, which sits atop the Great Bahamas Bank across the Straights of Florida from Miami, Florida, USA. a) Ooid sediment grains depicted in this two-dimensional cross sectional image display rounded edges typical of sub-spherical particles. Ooid sediment grains are denser than the resin filled pore space and appear lighter by contrast. b) a volumetric computed tomography image of a resin impregnated ooid sample indicates that the ooids are typically ovoid. This 7.8 mm subsample was removed from the center of a 5.9 cm diameter resin-impregnated diver core using a diamond tipped coring barrel. 18

Figure 2.2. Siliciclastic sediment (principally quartz sand) samples were collected south of Fort Walton Beach, FL, USA. a) Quartz sediment grains depicted in this two-dimensional cross sectional image are primarily sub-angular and range from sub-rounded to angular. Quartz sediment grains are denser than the resin filled pore space and appear lighter by contrast. The white particles are carbonate. b) a volumetric computed tomography image of resin impregnated quartz sand sample indicates that the quartz grains have irregular and rough surfaces. This 7.8 mm subsample was removed from a 5.9 cm diameter resin impregnated diver core using a diamond-tipped coring barrel. The tonal range is from white to and black the lowest density 19

Figure 2.3. SCUBA diver (Kevin Briggs) prepares to insert a polycarbonate core tube, held between his hands, into ooid sediments south of Bimini, Bahamas. The core tube is 25-cm long, 6.1-cm in outside diameter (5.9-cm inside diameter), with a 1-mm wall thickness..... 22

Figure 3.1. Scanning electron image (SEM) of a resin-embedded core sample is used to determine pore geometry by converting (a) SEM image into (b) a binary image from which (c) a skeleton image and (d) a Euclidean Distance Map (EDM) are created. (e) Pore body/EDM and (f) pore throat/EDM images enable the quantification of pore sizes. Coordination number is determined from (c). Images are $3.5 \text{ mm} \times 3.5 \text{ mm}$; the scale bar

in (a) is 500 μm and. The binary image (b) depicts pore space (black), grains (white), and plucked grains (gray). Plucked grains are painted white prior to image analysis.....	37
Figure 3.2. Vertical distributions of sediment porosity (from water-weight loss method) and mean grain size at SAX99 indicate slight amounts of variability. The sites are (●) STMS, (◊) ARL-UT, (▼) Lopes, (□) LF, and (▲) BAMS.....	44
Figure 3.3. Porosity determined by image analysis (pixel counting) for the Lopes and ARL-UT sites. Error bars represent 1 standard deviation about the mean	45
Figure 3.4. Permeability predictions from image derived pore-size distributions using the EMT technique for the Lopes and ARL-UT sites. Error bars represent 1 standard deviation about the mean	46
Figure 3.5. Images that depict homogeneity (a & b), heterogeneity (c & d), isotropy (e & f), and anisotropy (g & h) provide a conceptual basis to relate grain and pore geometry to porometric properties. Homogeneity is exemplified in vertical (a) and horizontal (b) images from the ARL-UT 6-7 cm interval, while heterogeneity is exemplified in vertical (c) and horizontal (d) images from the Lopes 7-8 cm interval. Isotropy is exemplified by vertical (e) and horizontal (f) images from the Lopes 6-7 cm interval, while anisotropy is exemplified by vertical (g) and horizontal (h) images from the Lopes 0-1 cm interval. Image size is 3.5 mm \times 3.5 mm. (Note: all permeability (k) values are $\times 10^{-11} \text{ m}^2$). Homo- and heterogeneity are based upon image porosity and iso- or anisotropy are based upon permeability determinations.....	49
Figure 4.1. Mean grain size values for ooid sands determined at 2-cm intervals from a core collected within one meter of the resin-embedded core, which was imaged with computed tomography and analyzed with 2D and 3D image analysis algorithms	70
Figure 4.2. Porosity by water weight loss was determined at 2-cm intervals from two cores that were collected adjacent to the resin-embedded core	71
Figure 4.3a. The Representative Elemental Volume (REV) for porosity of the HR 3D sample is realized prior to reaching the minimum length ($L_x = L_y = L_z = 375$) for the sediment volume of $L_x = 375$, $L_y = 400$, and $L_z = 475$	73
Figure 4.3b. Spectral density of the ooid CT data displays a large amount of variance in the image subvolumes bounded by edges of ≤ 60 voxels (0.690 mm) with a slight increase in variance for subvolumes bounded by edges ≥ 100 voxels (1.150 mm) and for the entire volume.....	74
Figure 4.4. Two-point correlation functions indicate that the sample is isotropic, because the correlations in the x , y , and z -directions almost completely overlap. Data acquired from the high-resolution 3D sample	75

Figure 4.5. Pore body distributions from high and low resolution 3D and 2D images (a-d) display similarly shaped histograms, but a significant degree of difference in mean pore body size and pore body numbers. Pore throat distributions (e-h) also display similarly shaped histograms, but a significant degree of difference in mean pore throat size and pore throat numbers 78

Figure 4.6. Coordination number ranged from 3 to 12 in the high- and low-resolution images of volumetric ooid sample. This plot depicts data for the high-resolution sample ... 80

Figure 5.1. A binary SEM image of the sand has the skeleton (white lines) imposed on the pore space (black), which is bounded by grains (white) for the (a) ooid sand collected from Long Key, Bahamas, and (b) quartz sand collected from the south of Fort Walton Beach, FL in the Northern Gulf of Mexico..... 95

Figure 5.2. Volumetric pore space displayed as one-dimensional medial axis images for a small section (40 voxels on a side) of (a) ooid sands collected from Long Key, Bahamas, and (b) quartz sand collected from the Northern Gulf of Mexico south of Fort Walton Beach, FL. In the skeleton image the color code indicates relative cross sectional dimension with violet largest and red smallest 96

Figure 5.3. Pore throats are commonly depicted by circular cylinders. This shape is based upon the minimum cross-sectional area of the pore throat dimension as determined from the skeleton or medial axis image or in the case of mercury porosimetry from the pore entry diameter. The velocity profile is constant and parabolic (i.e., maximum flow rate at the center of the flow field and zero at the boundaries). Red depicts highest flow velocity and dark blue depicts “no-flow” conditions..... 101

Figure 5.4. Pore throats are sometimes depicted by non-circular, but radially invariant shapes: (a) square and (b) triangular cylinders. These shapes have the same inscribed circle radius. The velocity profile is constant and parabolic (i.e., maximum flow rate at the center of the flow field and zero at the boundaries). Red depicts highest flow velocity and dark blue depicts “no-flow” conditions..... 102

Figure 5.5. Pore throats are bent or curved in some cases and thus the flow direction is altered prior to reaching the adjacent pore body..... 103

Figure 5.6. Pore throats are also be depicted by radially variant shapes, such as hourglass cylinders (a-b), to account for constriction along the throat length. Within these pore throats the parabolic velocity profile is orders of magnitude higher at the constriction than at the pore body-pore throat connection due to focusing..... 104

Figure 5.7. Volumetric flow rates for pore shapes with equivalent inscribed circular cylinder, but different cross-sectional shapes for pressure differences of 10^{-3} KPa. Relative relationships of Q to pore throat radius are constant between these shapes. The curve for the bent circular cylinder follows the same curve as the straight circular cylinder and is therefore hidden in the plot 108

Figure 5.8. Conductance ratio for square, triangle, cone_1.0, cone_1.5, and cone_2.0, and bent circle pore throats to the conductance of the circle with the same radius. Circle, square, triangle, cone_1.0, and bent pore throats have a unit length of 1.0, cone_1.5 has a unit length of 1.5, and cone_2.0 has a unit length of 2.0 109

ABSTRACT

Pore geometry and topology are important determinants of sediment physical properties, such as porosity and permeability. They also influence processes that occur in the sediment, such as acoustic propagation, attenuation, and dispersion, single- and multi-phase fluid flow, and hydrodynamic dispersion. This study uses images to evaluate pore geometry and topology of ooid (subspherical particles) and siliclastic (angular quartz) sand that was collected from the marine environment south of Bimini Bahamas and Ft. Walton Beach, FL, respectively. Image analysis techniques and predictive tools enable insight into the relationships among sediment pore geometry, topology, and physical properties for these differently shaped sands. High frequency acoustics utilize short wavelength signals to evaluate sediments. Correspondingly short length scales are then needed for sedimentary property predictions, which is possible with planar and volumetric image analysis of sand. This data was compared to data obtained by direct large scale measurements (e.g., water weight loss, constant head permeability) were made. Mean porosity differed by as much as 0.04 and mean permeability showed good agreement and differed by a factor of 2. Given that the image analysis predictions were made from much smaller samples (~equivalent to the length scale of the high acoustic frequencies used) than the bulk samples, a sediment characterization at acoustically relevant length scales is possible. It was also demonstrated that for these homogeneous sands (i.e., ooids and quartz) two-dimensional pore geometry and topology are quite similar to three-dimensional pore geometry and topology (i.e., pore connectivity). Additionally it was determined that pore network models typically overestimate the topology and therefore, in order to match image and bulk predictions of sediment

properties, these models must underestimate the conductance of individual pore throats (i.e., conductive element in sand). Typically pore throats are depicted as straight cylinders. Image data suggests that pore throats are better represented by biconical shapes where conductance is as much as 3 times higher than conductance within the straight cylinders. These findings indicate that increased realism in pore throat shape (higher conductivity) and in topology (fewer pore throats) may significantly influence network model evaluations of fluid flow or acoustic propagation in marine sand.

CHAPTER 1. INTRODUCTION

1.1 Importance of Porosity, Permeability, and Pore Geometry in Sands

Fluid flow and acoustic propagation within marine sand are determined, in part, by sediment pore geometry and topology and the corresponding sediment physical properties of porosity and permeability (Biot, 1956; Bear, 1972; Dullien, 1992). Pore geometry influences acoustic detection of buried objects (Richardson et al. 2001a; Thorsos et al., 2001), maintenance of fresh water aquifers (Bell, 1981; Bell et al. 1992), mitigation of subsurface contaminants (Fetter, 1993), and recovery of petroleum and natural gas (Clark and Kleinberg, 2002; Mohanty, 2003). The relationship between these processes and pore geometry is not completely understood. However, this understanding is critical to increasing homeland security (Porter et al., 2001), fostering public health (Corsi et al., 2003), and maintaining stability in global oil markets (Schifferes, 2002). To understand the influence of pore geometry on these processes pore geometry must be quantified, mapped, and evaluated. Quantifying, mapping, and evaluating sediment pore geometry will facilitate an explicit and accurate representation of the porous media in which to simulate fluid, thermal, electrical, and acoustic transport processes (Blunt, 2001).

An Office of Naval Research Sediment Acoustic eXperiment (SAX99) was conducted to address the influence of pore geometry and sediment properties (Richardson et al., 2001a) on acoustic penetration into and propagation within a homogeneous body of marine sand (Thorsos et al., 2001). Geometrical properties, such as tortuosity and pore size distribution, and sediment physical properties, such as porosity and permeability,

were evaluated at several scales. The work to quantify these properties was done, so that bounds on their values could be incorporated into acoustic models. This would disallow application of unrealistic property values to acoustic models simply to fit experimental data with model predictions (Biot, 1956; Stoll, 1989; Thorsos et al., 2001; Williams et al., 2002).

During the SAX99 study pore geometry was quantified at several scales to determine the bounds of porosity, permeability, and tortuosity and thereby provide a clear determination of the influence of pore geometry on acoustic propagation at scales that corresponded to those of the wavelength for specific frequencies (Reed et al. 2002, Tang et al. 2002; Williams et al. 2002). It was determined that that pore and grain geometry play an increased role in determining sediment properties, sound speed ratio, and acoustic attenuation at acoustic frequencies above 100 kHz or wavelengths less than 17 mm. For instance, Williams et al. (2002) indicated that the inability of a Biot-based acoustic model to precisely predict dispersion and attenuation at high frequencies was probably small-scale (mm- to cm-scale) variability or variance in porosity and permeability (Reed et al., 2002; Tang et al., 2002) and to movement at grain contacts (Williams et al., 2002; see Biot, 1956). These findings suggest that the sediment properties that control porosity and permeability and the grain-to-grain interactions need to be quantified and incorporated into increasingly realistic acoustic models.

Pore geometry and pore scale processes were determined to significantly influence groundwater availability in numerous locations throughout the world (Bear, 1972; Fetter, 1994). This is especially true in areas with high-population density, extensive agricultural use, and extensive recreation. For instance, in Las Vegas, NV,

which is an agricultural and vacation area, water extraction greatly exceeds water replenishment. Water extraction typically exceeded water replenishment by a factor of 2 to 3 since 1946, thus, water levels have been lowered up to 90 meters within a 200-300 meter thick aquifer (Bell, 1981). Not only is groundwater more limited and harder to obtain, but also the aquifer sediments are consolidated and the storage capacity is diminished. Evidence of aquifer consolidation is subsidence of 0.75-1.5 meters in several locations (Bell, 1981; Bell et al, 1992; Poland and Davis, 1969). To increase groundwater supply and to stave off consolidation, surface water has been injected into the aquifer, which is influenced by the shapes, size, and location of the pores (Reeves and Celia, 1996).

Shape, size, and pore path lengths are known to significantly influence contaminant transport, retention, and mitigation in aquifers. For instance the Las Vegas aquifer is threatened by the introduction of point and non-point sources of pesticides, chlorinated solvents, and petroleum products (e.g., MBTE and TBA).

The relative permeability for water, oil, and gas is directly related to the sediment pore geometry. Currently, oil extraction is ~30% efficient due to oil entrapment; this occurs as oil permeability is diminished during the extraction process (Clark and Kleinberg, 2002; Mohanty, 2003). Understanding relative permeability has facilitated increased recovery of oil (Fenwick and Blunt, 1998a; Mohanty, 2003). It is believed that as pore scale network models become more realistic the recovery of oil will simultaneously increase (Blunt, 2002).

1.2 Bulk Properties of Sand

Pore scale network models require that bulk properties of the sediments be determined, so that modeling efforts are constrained, and understanding of acoustic propagation and fluid mechanics within pore space is increased. The influence of pore space on acoustic propagation, fluid mechanics, chemical transport, and petroleum recovery occurs due to heterogeneity at the microscopic scales, which may occur even within homogeneous sedimentary systems. These pores, which are arranged in an interconnected converging-diverging matrix, reflect the complexity of the bounding grain shapes (Dullien, 1992). The bulk properties determined for this sediment are porosity, permeability (or hydraulic conductivity), tortuosity, and pore conductance are strongly influenced by this variability. Porosity is the amount of void space within a volume of sediment. Permeability is a measurement of the ability of a porous media to transmit fluid. Tortuosity is the ratio of the fluid flow path to the straight-line path over this gradient squared. Pore conductance is the amount of fluid that a specific pore throat can transport; it is the underlying determinant of permeability.

Physical property measurements validate predicted physical property values, which are made by indirect measurements. Measured values for porosity, permeability, and tortuosity are typically bounded by values for cubic and hexagonal closed packing (hcp) of mono-sized, spherical beads. For these ideal systems, porosity ranges from 0.27 (hcp) to 0.48 (cubic; see p. 86 in Fetter, 1994), intrinsic permeability from 10^{-13} to 10^{-10} m² (hydraulic conductivity from 10^{-6} to 10^{-3} m s⁻¹) (see p. 98 in Fetter, 1994 and p. 136 in Bear, 1972), and tortuosity factor from 1.3 to 2.2 (Bear, 1972; Clennell, 1997). However, monosized spheres fail to depict the complexity of naturally occurring material; therefore

these values serve only as loose bounds. Evaluation of natural systems is required to constrain physical property values. In clean (i.e., <5% particles smaller than 62 μm), shallowly buried sands sediment physical properties are influenced by grain shape, sorting, and size distribution (Jackson et al., 1978; Bennett et al., 1989). Despite morphological and statistical variations within naturally occurring sands, physical properties often fall within much narrower ranges (Briggs, personal communication). Medium-sized, well-sorted marine sands tend to have average porosity values near 0.38 (Fetter, 1994) with a range of about 0.5, intrinsic permeability values about 10^{-11} m^2 (hydraulic conductivity values about 10^{-4} m s^{-1}) (Fetter, 1994) with a range of about 2 orders of magnitude, and tortuosity factors approximately equal to 1.5 (see pp. 45-46 in Carman, 1956) with a range of about 0.6.

1.3 Network Models

These sediment property values suggest that the pore geometry, which determines them, is complex. Therefore, pore geometry is often considered stochastic, fractal, and random. However, pore space geometry can also be defined or treated rigorously as geometrically definable shapes with component parts. In fact, pore space has been defined mathematically (Dullien, 1991) and treated as an analogy to electrical wiring (Fatt, 1956). That is pore space is commonly divided into junctions (nodes or pore bodies) of intersecting paths (bonds or pore throats), with the number of paths that meet at a junction termed coordination number.

Network models provide a mechanism to evaluate the influence of pore structure and topology (i.e. coordination number or connectedness of the pore space) on single- and multiphase flow (Celia et al., 1995; Blunt, 2001) in systems that contain pore bodies

connected by pore throats. To make fluid flow predictions, two similar approaches have been developed. The first approach uses electrical conductance (determined directly and mathematically) to simulate fluid conductance. The second approach makes direct predictions of volumetric fluid flow by solving the Navier-Stokes equations in the pore space.

The first network model approach is the most common and will be addressed further here. Fatt (1956a, b, c) established a hydraulic analog using an electrical circuit to simulate the transmittance and resistance of fluids within the pore space of a rock. The analog was an electrical circuit with interconnected (nodes) wires that allowed current to flow in series and in parallel; electrical resistors that were incorporated into wires (“paths”) were analogous to pore throats and electrical junctions (“nodes”) were analogous to pore bodies. The conductivity of the system was measured with an ohmmeter. This interconnected graphical treatment of pore space was a significant improvement over the single bundle of parallel and unconnected tubes. It was also an important step towards realistic depictions of the pore geometry.

The electrical analog of porous media was advanced with the development of an effective medium theory (EMT) technique (Kirkpatrick, 1973). The principle advantage of EMT over direct measurements (Fatt, 1956) is that conductivity is solved mathematically rather than empirically. EMT was implemented to accurately predict permeability in a variety of sandstones (Koplik et al, 1984; Doyen, 1988; Locke et al., 2002). EMT determines the conductance of each throat, which provides a distribution of conductivities as the pore throat sizes are variable over some range. The EMT then replaces the pore throats in the system with a single pore throat that has the same

conductance as the entire system. This pore throat is then used to determine the permeability and hydraulic conductivity of the system. This technique was also successfully used to predict permeability in marine sands (Reed et al. 2002). This work is reprinted, in part, in chapter 3 by permission of The IEEE Journal of Oceanic Engineering.

While the EMT method still finds favor in the scientific community because it is relatively simple, there is only one equation to solve, boundary conditions can be ignored, and systems of linear equations are unnecessary, EMT is limited to absolute permeability predictions. Therefore, pore-scale network models that allow pore size heterogeneity, and predict absolute and relative permeabilities from systems of linear equations, provide a valuable testing ground in which to test current theory of multiphase flow and acoustic propagation.

The basis behind these systems of linear equations is the hydraulic conductivity equation. This is essentially the same as the electrical conductivity equation, but with the addition of the dynamic viscosity of the fluid (e.g., freshwater, saltwater, or oil). The hydraulic conductivity (K) (cm/s) of a specific pore throat is given by

$$K = \frac{Ar^2}{8\mu l} \quad (1.1)$$

where A is the minimum cross-sectional area of the pore throat, r is the pore throat radius at the minimum cross-sectional area, μ is fluid dynamic viscosity (kg/(m s)), and l is the length of the pore throat. This is then used to solve the volumetric flow (Q) (m³/s) through the pore throat as

$$Q = K \frac{\Delta P}{L} \quad (1.2)$$

where ΔP (N m/s) is the pressure difference across the length (L) of the system (Bear, 1972; Fetter, 1994). The pore-scale network models are commonly based on a simple packing of monosized spheres and employ cubic network of pores and throats (King and Blunt, 1990; Reeves and Celia, 1996; Pan et al. 2001). In these models pore bodies and pore throats are a fixed distance apart, pore sizes are often the same, and pores are mapped onto a cubic lattice. The cubic lattice is derived from an idealized sediment; the sediment is modeled as a cubic packing of monosized spheres, which would have a porosity (n) of 0.48, and which would not exist in that natural environment. Also in these systems, the coordination number is generally constant (i.e., 4 in 2D and 6 3D). To increase realism in these models, a pore size distribution and a specific range of coordination numbers is supplied.

Cubic models are advantageous, because they have periodic boundary conditions. That is, the mass, momentum, or flux that occurs at one boundary is mirrored on the opposite boundary. For instance a pore throat that exits one boundary enters the opposite boundary and the fluid flux that propagates through this boundary, which facilitates the conservation of mass and fluid within the pore network. This simplicity also alludes to the fact that cubic geometry has limited realism in depicting pore throat and pore body locations, pore size distributions, correlations between pore throats/bodies, coordination numbers, and pore throat shape. Therefore this geometry lacks several components, which are known to influence pore scale processes, such as laminar flow, turbulent flow, imbibition, and drainage (Reeves and Celia, 1996, Blunt 2001).

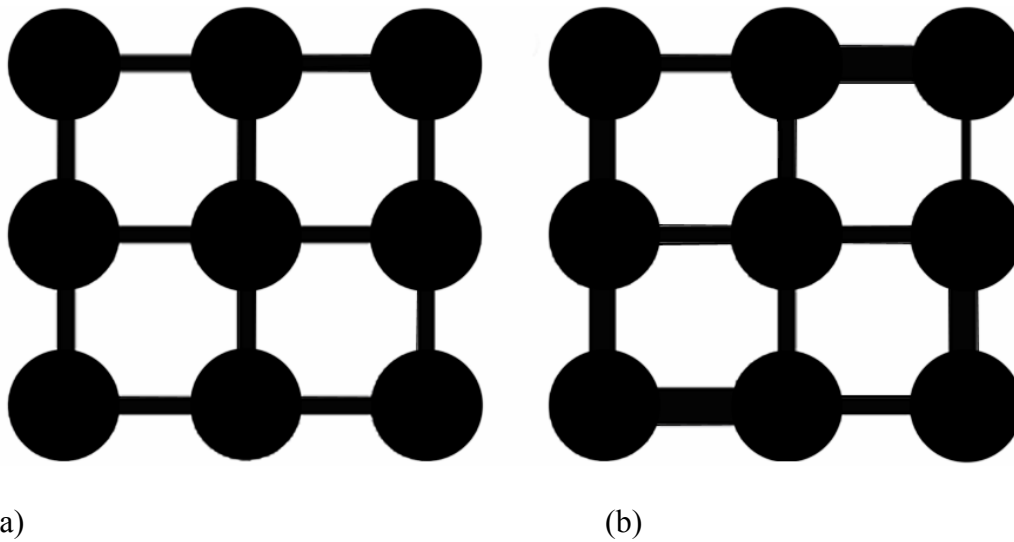


Figure 1.1. Typical configurations of network models are that the pore bodies (circles) and pore throats (connecting lines) are either all the same size (a) or have a range of pore throat radii to incorporate the conductance range that was determined to exist in the porous media (b).

A deviation from the cubic packing regime, is the hexagonal close packing (hcp) of monosized beads, which represents a fully consolidated packing (i.e., porosity is low as possible; $n = 0.26$) for this sediment type. In this system, pore bodies and pore throats would be accurately modeled by a rhombic or rhombohedral-lattice that would require pore throats to be mapped onto a honeycombed lattice without right angles.

This packing regime was exhaustively evaluated by carefully determining grain locations by Finney (1970). This work facilitated accurate determinations of pore body and pore throat locations for a network model (Bryant et al., 1993). With this model, Bryant et al. (1993) demonstrated that a correlation between pore geometry and permeability exists; after remapping the pore geometry, permeability differed by a factor of 2 (Bryant et al., 1993). This difference is significant in acoustic predictions of sound-speed dispersion and acoustic attenuation in sand (Williams et al., 2002).

The influence of pore size correlations on sediment physical properties may be even more important in natural sand in which pores are randomly distributed and non-uniform (Figure 1.2). Pore size distributions and non-uniformity suggests that pore shape variability should be realistically depicted and accurately mapped rather than forced to a square or cubic lattice. If this task can be accomplished and a realistic depiction of the sediment is acquired, then a fuller understanding of sediment transport properties in marine sands could probably be achieved (Reeves and Celia, 1996, Thompson and Fogler, 1996; Blunt, 2001).

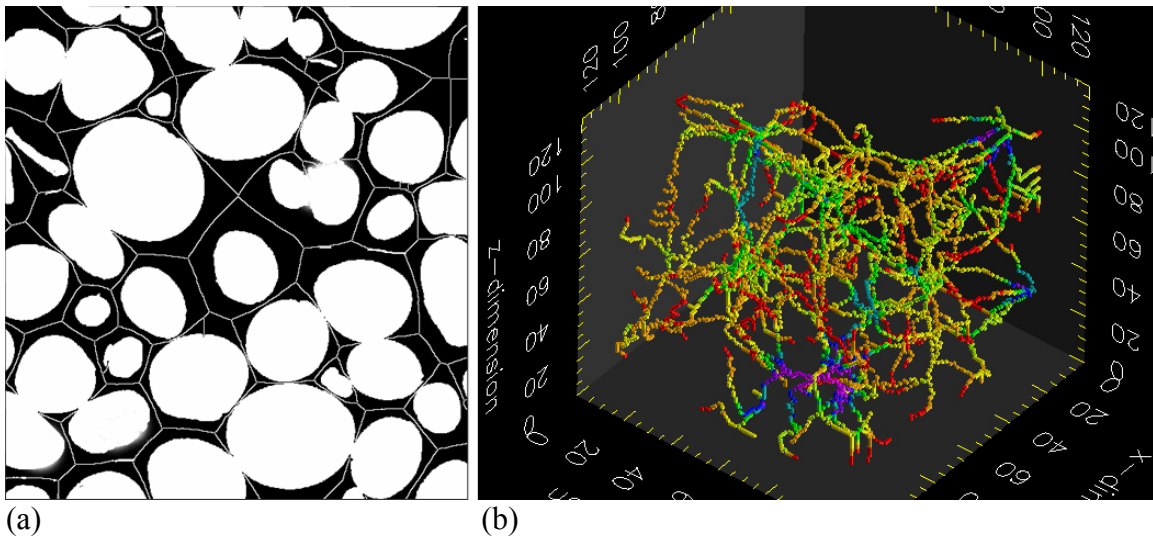


Figure 1.2. Pore space in these images display pore paths (white lines (a) and color lines (b)) that are oriented in numerous directions. These depictions indicate that the pore paths in naturally occurring sands are much more complicated the cubic packing models of monosized spheres. That is few if any paths are parallel or perpendicular to another and as such are not represented by a square or cubic lattice. In (b) the color code is red for relatively small pore openings and violet for relatively large pore openings (pore volume and grains are not depicted). In (a) pore area is black, grains are white, and pore paths are depicted by white lines. Dimensions of (a) are $\sim 1100 \times 1100 \mu\text{m}^2$ and of (b) are $\sim 1100 \times 1100 \times 1100 \mu\text{m}^3$.

Geometrically realistic network models require accurate pore space information, such as, pore throat and pore body locations, pore size distributions, correlations between pore throats/bodies, coordination numbers, and pore throat shapes. Two-dimensional

images (e.g., photomicroscopic and scanning electron microscopic) have yielded pore sizes, coordination numbers, and path geometry, which have been used in numerous studies to accurately predict sediment physical properties. Since the relationship between 2D and 3D pore geometry and topology is not well understood 2D data (i.e., pore size distributions and coordination numbers) have sometimes been discounted as non-representative of the 3D system. The relationship of 2D and 3D data (i.e., pore size distributions and topology) is now possible, since three-dimensional images are now an increasingly common. This is due to the advancement of medical computed tomography (CT), the application of CT to geophysics, and algorithms that evaluate CT image volumes (Hounsfield, 1976; Vinegar and Wellington, 1987; Lindquist, 1996).

1.4 X-ray Generated Images

X-ray generated images provide accurate realizations of the sediment system that can be used to create geometrically realistic 2D and 3D pore-scale network models. Scanning electron microscopy provides two-dimensional image of the sample surface as it is bombarded with x-rays. The x-ray source and x-ray receiver are maintained in a fixed geometry with respect to the sample. To generate information about the sample at depths below the surface, the sample surface is ground away a new surface is exposed, and an image can be collected. Ultimately the sample is destroyed. during the production of high resolution images (<10 μm pixels) It has yet to be demonstrated that 2D image data effectively corresponds to 3D image data as it is nearly impossible to reconstruct the three-dimensional sample directly or accurately by stacking two-dimensional images (Koplik et al., 1984).

Therefore, 2D data can either be used to determine 1-point (i.e., porosity) and 2-point (e.g., chord length distributions) correlation functions for the creation of 3D volumes and network models or 2D lattice models can be directly created from the available images. If the 3D structure created from 2D data does not incorporate the 3-point correlation functions (i.e., pore body/pore body, pore throat/pore throat, or pore body/pore throat), it is unlikely that it will accurately reflect the processes that determine permeability, drainage, and imbibition (Reeves and Celia, 1996, Celia et al., 1995). If a 2D lattice model is used, the topology of the sediment system is not fully represented, which indicates that the volumetric flow would also be underrepresented (Doyen, 1988; Jerauld and Salter, 1990; Lock et al., 2002). Because the difference between 2D and 3D topology is not well known, the influence of predicting sediment properties with 2D topology is also not understood.

X-ray computed tomography provides a means to capture all correlation functions that have been deemed important (Dullien, 1991; Bryant et al., 1993; Thompson and Fogler, 1996; Celia and Reeves, 1996, Blunt, 2002) by facilitating the creation of three-dimensional images in a non-destructive manner. These images are created as samples are rotated and continually x-rayed at incremental angles between a fixed x-ray tube and detector array. Specific advantages of three-dimensional images are that they maintain the 3D grain to pore relationships over the images sample to within the limits of the machine resolution. The highest resolution systems produce $\sim 10 \mu\text{m}$ voxels for 8-mm diameter ooid or quartz sand samples. This is possible with the highest resolution systems (i.e., GeoSoilEnvironment at the Applied Photon Source of the Argonne National

Laboratory or the Universal Systems HD-500 Industrial Computed Tomography System housed at the Naval Research Laboratory Stennis Space Center, MS).

In x-radiography (SEM or CT) there are two different effects (i.e., photoelectric and Compton effects) at work to scatter x-rays from the sample material. The photoelectric effect discovered by Einstein in 1905 is a destructive process in which an incident x-ray strikes and liberates an electron in an inner orbital of a molecule. An outer orbital electron replaces this electron. During this replacement process an x-ray with characteristic energy is emitted. The Compton effect, discovered by its namesake in 1934, is an elastic process where the source x-ray is partially deflected by an electron occupying the orbital of a molecule; the deflected x-ray and dislodged electron, now with lowered energy, may both be intercepted by the detector. The photoelectric effect is most important at low energies and the Compton effect is most important at high energies. Both effects are important with the HD-500 system, which emits polychromatic energy, whereas for the monochromatic and low energy sources of the APS the photoelectric effect is most important. The result of these processes is that only part of the energy that strikes the sample reaches the detector. The rest of the energy is either scattered or absorbed by the sample, which is displayed in Beer's Law,

$$I = I_0(e^{-\mu x}). \quad (1.3)$$

In equation 1.3, I is the x-ray energy intensity that reaches the detector, I_0 is the x-ray energy intensity produced at the source, x is the sample thickness, and μ is the linear attenuation coefficient of the sample (Wellington and Vinegar, 1987).

The x-rays that enable the CT image are either Characteristic or Brehmstrahlung x-rays. Characteristic x-rays are emitted in the same way as described above. In SEM,

characteristic x-ray energy is often used to identify the molecular composition of the sample materials. Bremsstrahlung x-rays are produced when the incident x-rays pass through the sample and interact with the nucleus of the molecule, but without a collision. The maximum amount of energy given off is equal to the acceleration potential (keV) of the electron source and is directly related to the deceleration of the x-ray that is incident upon the sample. For it is in the deceleration that the x-ray energy is given off. Maximum emitted x-ray energy occurs during a total deflection of the incident x-ray. The x-ray energy that reaches the image intensifier is converted to photons by the scintillator. The photons are then converted to electrical impulses by the photocathode, focused onto the digital camera array (“film”) and converted to an array of linear attenuation values. The dynamic range of pixel or voxel values can vary from 0-255 for 8-bit images to 0 to 65536 for 16-bit images and the ability to clearly differentiate the values is in part dependent upon the repetition of line scans. That is, if the sample is x-rayed at many angles (e.g., 2400) many times (e.g., 6) then the image is much clearer, due to more integration, than if the sample is x-rayed at fewer angles (e.g., 720) a couple of times (e.g., 2).

Computed tomography images are prone to several artifacts that need to be considered. These are beam hardening, star artifacts, and edge blurring. Beam hardening occurs in systems that emit polychromatic x-rays; the low energy x-rays are attenuated within the sample and higher energy x-rays penetrate the sample. The effect is that the image edges will appear more dense (i.e., whiter) than the image center. This effect can be reduced by placing an aluminum sleeve, which effectively serves to attenuate the low energy x-rays prior to them reaching the sample. Post processing algorithms also may be

used to remove beam hardening effects. Star artifacts occur if samples contain materials with vastly different attenuation coefficients (e.g., mud with pyrite). Pyrite will scatter x-rays and leave a white, star-shaped pattern. This artifact obscures details in the nearby surrounding areas. The final artifact is blurring. Blurring occurs because the linear attenuation coefficient for each voxel is an average of all the material that occupies the respective space. It is most easily reduced by increasing image resolution (e.g., increasing the image size, the bit size, or maximizing the sample area within the field of view), reducing sample size, increasing the linear attenuation of one of the materials (e.g., adding CsCl to water in the pore space), or increasing the number of angles scanned and the number of scans per each angle. By increasing the number of angles scanned and the number of times each angle is evaluated, the voxel values are effectively smoothed and the images have more contrast and less blurring.

1.5 Current Research and Dissertation Objectives

Quantifying pore geometry and modeling sediment physical properties are basic prerequisites to understanding the importance of pore geometry and pore scale transport processes in the fields of acoustics, hydrology, contaminant mitigation, and petroleum engineering. However, numerous unresolved issues exist that are related to quantifying pore geometry and modeling sediment physical properties. These issues include 1) the utility of 2D image analysis to determine small-scale (mm to cm) variability in porosity and permeability within homogeneous systems; 2) the similarity of 2D and 3D pore geometry and topology for specific image resolutions; 3) the influence and importance of pore shape on volumetric fluid flow and conductance.

The primary objectives of this work are (1) to quantify pore geometry and sediment physical properties using image analysis; (2) to establish the relationship between 2D and 3D pore geometry and topology; and (3) to quantify fluid conductance for representative pore throats. To accomplish this task, marine sediments were collected and analyzed using traditional measurements (chapter 2) in order to “ground truth” image analysis predictions for naturally occurring marine sands (chapter 3). Then 2D and 3D computed tomography images were collected from which pore geometry and topology, sediment property, and pore conductance predictions were made and compared (chapter 4). Finally, realistic pore throats were created and the conductance of each pore throat was determined using a finite element determination of volumetric fluid flow (chapter 5).

Note: portions of chapter 2 and chapter 3 were reprinted with permission of The IEEE Journal of Oceanic Engineering. Chapter 4 was submitted to Journal of Geophysical Research B: Solid Earth.

CHAPTER 2: MATERIALS AND METHODS*

2.1 Marine Sands: Sample Sites, Collection, Characteristics, and Preservation

2.1.1 Geologic Settings and Sediment Characteristics

Marine sands vary markedly from one setting to another provided sediment sources are also markedly different. The two sand samples (i.e., ooids and quartz sands) used in this study were formed by vastly different processes and were generated from vastly different sources. Ooid sand samples, such as those collected adjacent to Bimini, Bahamas (Figure 2.1), are typically autochthonous (loose translation is “formed where found”). Layers of calcium carbonate, which is extracted from upwelled seawater that is supersaturated with CaCO_3 , are precipitated over a granular nucleus (Bathurst, 1975; Wilkinson and Landing, 1978). The ooids then grow into subspherical (i.e., egg shaped or ooid; Power, 1951; Figure 2.1) sediment grains. For an ooid sand body to accumulate, the growth process must occur in shallow semi-enclosed, high-energy, basins that retain the growing ooids. Therefore, the ooids are typically found in shallow basins that are adjacent to deep ocean basins, which supply the seawater supersaturated with CaCO_3 .

The siliciclastic sand (i.e., quartz) samples were collected on the West Florida Sand sheet (south of Fort Walton Beach (Figure 2.2)) (Doyle and Sparks, 1980), which is a homogeneous surficial body of relict allochthonous quartz sands (Hyne and Goodell, 1967). The West Florida Sand Sheet is located on the continental shelf offshore from Panama City, Florida, and it extends westward across the Alabama state line. The quartz sand, which was primarily derived from the Appalachian Mountain system, was

*(c) 2002 IEEE. Reprinted, with permission, from IEEE J. Oceanic Eng., vol. 27, pp. 581-592, 2002.

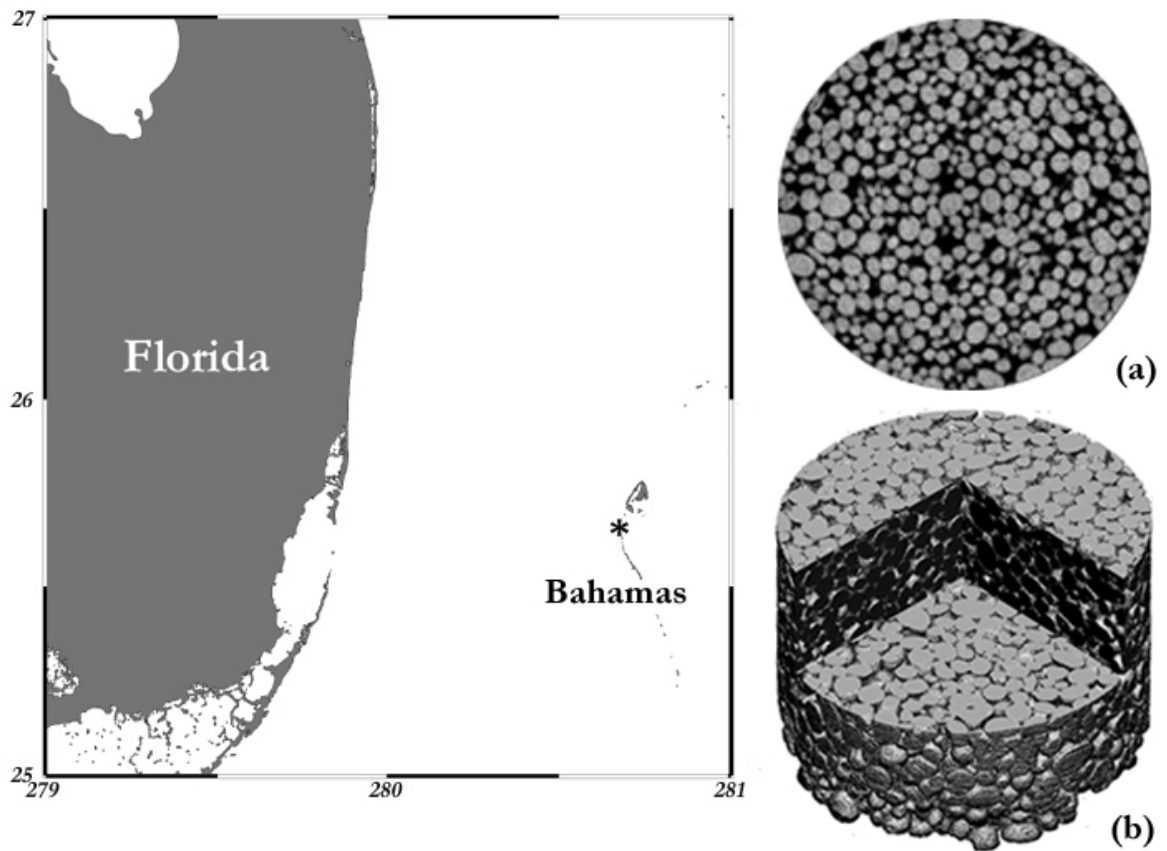


Figure 2.1. Ooid sediment samples were collected south of Bimini, Bahamas, which sits atop the Great Bahamas Bank across the Straights of Florida from Miami, Florida, USA. a) Ooid sediment grains depicted in this two-dimensional cross sectional image display rounded edges typical of sub-spherical particles. Ooid sediment grains are denser than the resin filled pore space and appear lighter by contrast. b) a volumetric computed tomography image of a resin impregnated ooid sample indicates that the ooids are typically ovoid. This 7.8 mm subsample was removed from the center of a 5.9 cm diameter resin-impregnated diver core using a diamond tipped coring barrel.

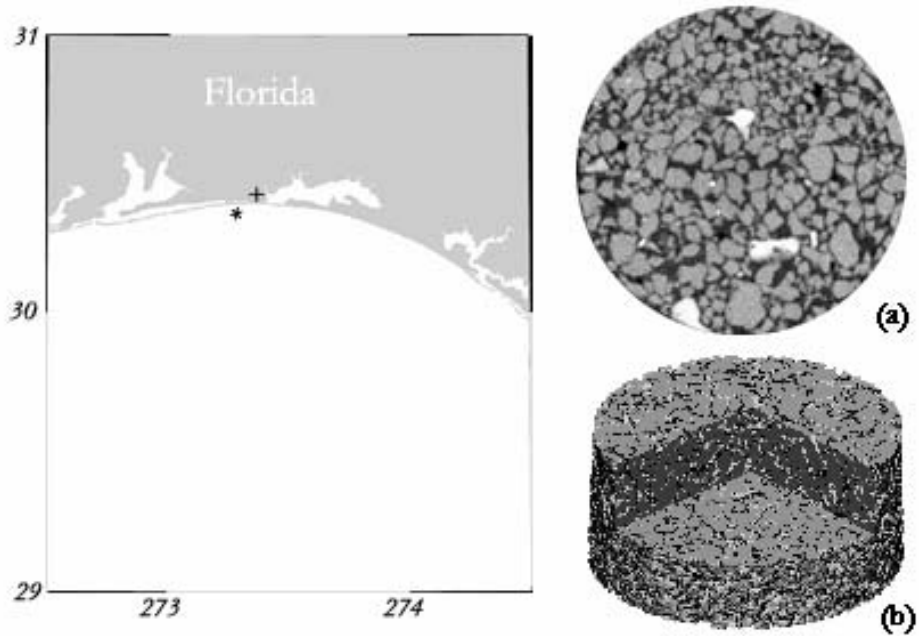


Figure 2.2. Siliciclastic sediment (principally quartz sand) samples were collected south of Fort Walton Beach, FL, USA. a) Quartz sediment grains depicted in this two-dimensional cross sectional image are primarily sub-angular and range from sub-rounded to angular. Quartz sediment grains are denser than the resin filled pore space and appear lighter by contrast. The white particles are carbonate. b) a volumetric computed tomography image of resin impregnated quartz sand sample indicates that the quartz grains have irregular and rough surfaces. This 7.8 mm subsample was removed from a 5.9 cm diameter resin impregnated diver core using a diamond-tipped coring barrel. The tonal range is from white to black with white the highest density and black the lowest density.

transported through the Apalachicola fluvial and estuarine systems during the Plio-Pleistocene period and was transported to the present location by nearshore currents (Doyle and Sparks, 1980). Currently the sand deposits at the SAX99 experimental site are part of a shoreface-connected sand ridge that is in equilibrium with hydrodynamic conditions (Hyne and Goodell, 1967; Locker and Doyle, 1992)). The result is a homogeneous sand deposit of relic quartz sand, with small percentages of relic heavy minerals (e.g., ilmenite (FeTiO_3) or rutile (TiO_2)) and biogenic carbonate (e.g., shells), and clay sediment (Hyne and Goodell, 1967; Locker and Doyle, 1992).

Individual grains display features typical of marine quartz sands (Krinsley and Doornkamp, 1973), such as linear and conchoidal fractures, pits, and grooves (Fig. 2.4). This sediment type is predominate along the coastlines from New England to Northern FL and from the Florida Panhandle through the Barrier Island system of Alabama, Mississippi, and Louisiana. The principle grain shape is sub-angular (Power, 1951; Figure 2.4), whereas the ooids are subspherical (Powers, 1951). Therefore, these grains are nearly opposite end members in the Powers (1951) roundness scale.

2.1.2. Sample Collection and Analysis

Sand samples are notoriously difficult to collect with commonly deployed devices (e.g., box cores, gravity cores, or grab samplers) in such a way that the sediment remains virtually undisturbed from the sediment/water interface to depth. This difficulty manifests itself for two primary reasons. First, as the sampling device impinges upon the sediment-water interface, water that is pushed ahead of the sampling device disrupts, suspends, and otherwise rearranges surficial sediments. Second, as the sampling device is pulled out of the seafloor with a sediment sample, overlying and interstitial water

facilitates sediment liquefaction as the core sample is jarred and vibrated toward and onto the ship. To circumvent the bow-wake and liquefaction problems, SCUBA divers carefully collected sediment samples by hand in 6.1-cm-diameter (5.9-cm ID), clear, polycarbonate, core-tubes (Fig. 2.3). In this case the divers push the tubes into the bottom as far as possible (generally about 25 cm) and then the tubes are capped on top. Next the sediment surrounding the tubes is removed by hand, a cap is placed on the bottom, and the tube is removed from the sediment, and returned to the boat by the divers. During and after collection, the diver-cores were isolated from vibration, handled carefully, and retained in a vertical position until traditional measurements (i.e., routine sediment physical/geologic measurements, such as constant head permeability, grain size, and water-weight loss porosity) were made (Richardson et al., 2001a; Tang et al., 2002) or sand was fixed in place by resin impregnation. Resin-impregnated samples were retained for imaging. From images porometric and geometrical properties were quantified using image analysis (Dullien, 1978, Doyen, 1988; White et al., 1998; Al-Raoush et al., 2002), image analysis/effective medium theory modeling was conducted to determine permeability (Kirkpatrick, 1973; Koplík, 1982; Doyen, 1988; David et al. 1990; Lock et al. 2002), and finite element modeling was performed to determine pore throat conductance (Thompson and Fogler, 1996; Sisivath et al., 2001).

Percent water content was determined gravimetrically by measuring water-weight loss after drying at 105° C for 24 hours from 2-cm interval subsamples of undisturbed diver-collected cores. Measured values of average grain density were used to calculate porosity from water content (Briggs, 1994). Porosity values were corrected for salt content.



Figure 2.3. SCUBA diver (Kevin Briggs) prepares to insert a polycarbonate core tube, held between his hands, into ooid sediments south of Bimini, Bahamas. The core tube is 25-cm long, 6.1-cm in outside diameter (5.9-cm inside diameter), with a 1-mm wall thickness

The sediment grain size distribution was measured from disaggregated samples by dry sieving with a sieve shaker for gravel- and sand-sized particles. In addition, pipettes were used for silt- and clay-sized particles (never more than 5% of total weight) with the distribution expressed as a weight percentage (Briggs, 1993) and mean grain size (mm) was estimated by a graphic method (Folk, 1965). Phi size (ϕ), which is a common descriptor of sediment grain size, is equivalent to the negative base-two logarithm of the diameter expressed in millimeters. Sediment grains fall in the sand sized fraction if the mean grain size falls in the range of 1 to 4 ϕ (1 to 0.064 mm).

Hydraulic conductivity was measured by a constant-head permeameter technique on whole cores while aboard ship within one day of core collection. For this experiment, 13-cm long cores (also 6.1-cm outside diameter) were collected such that the sediment completely filled the core liner from top to bottom. Hydraulic conductivity (K) was determined with a Soiltest K-605 combination permeameter, which was modified to

accommodate the entire 13-cm-long core (Richardson et al., 2002). For each core, five consecutive hydraulic conductivity measurements were made using surface seawater, which percolated through the core as a result of the constant hydraulic head. The intrinsic permeability (k) of the sediments is then found from Eq. 1.1 by accounting for the density and dynamic viscosity of the seawater used in the analysis. Fluid density and dynamic viscosity were calculated from temperature and salinity of surface seawater from the Bimini and SAX99 sites (Richardson et al., 2001a) at the time the measurements were made.

2.1.3 Resin Impregnation to Preserve *in situ* Pore Geometry

Several cores were collected at each site and some of these were impregnated with a polyester casting resin to preserve the pore geometry and topology of the natural sediment. The resin solidified prior to transport to the shore-based laboratory (Richardson et al. 2001a). Considerations made for choosing a suitable resin depend on the grain and pore sizes, resin viscosity (Gaither, 1953), and degree of water saturation. For these experiments a polyester casting resin was used that could be applied in water-saturated samples for medium-sized sand and could be prepared to a fairly low viscosity. The utility of multi-component polyester casting resins for binding water-saturated sands *in situ* was previously demonstrated (Brown and Patnode, 1951; McMullen and Allen, 1964; Schroeder and Jacob, 1976). These resins were found to be ideal for marine sands because they 1) attain low viscosity by mixing and without heating, 2) cure without heating, and 3) maintain constant volume during curing. To detect possible sediment volume changes during the resin-impregnation process, the sediment-water interface was marked on the outside of the cores with a 1-mm-wide line after cores were returned to the

ship and prior to resin impregnation. No changes in the position of the sediment-water (or sediment-resin) interface with respect to the 1-mm-wide line were noted after the resin cured; therefore the volumetric change in sediments due to resin impregnation was at most $\pm 0.05\%$ (based on the thickness of the line). Based on this information, the following assumptions were made: 1) the sediment volume did not change; 2) the pore volume did not change; and 3) the *in situ* pore geometry and topology were preserved.

2.2 Image Collection and Analysis

2.2.1 Image Collection

Two-dimensional images were collected from 1-cm-square blocks that were cut from each 1-cm depth interval of the resin-embedded diver-collected cores. The blocks were polished smooth and surfaces parallel and horizontal to the sediment water interface were digitally imaged with an Amray 1820 Scanning Electron Microscope (SEM) in backscatter electron mode. The “parallel” block surface images were collected in the top 1.0 mm of the indicated depth intervals, whereas the “perpendicular” block images were collected from mid-depth of the interval. Image resolution (i.e., pixel size) is $6.9 \mu\text{m}$.

Three dimensional images were collected from samples that were cut out of the resin-embedded core. A subsample was removed from the larger core by cutting a 1-cm-thick, horizontal section (a 1-cm thick \times 6-cm diameter disk) from the core, after which a subsample (0.8-cm-diameter \times 1-cm-long) was cut from the center of this disk with a diamond-tipped coring tool. The center of the disk was chosen for subsamples, because this area was farthest from the edges of the core tube and presumably within the pristine and entirely undisturbed portion of the core. The subsamples were imaged using the computer tomography facility on the GSECARS BM-13D beamline of the Advanced

Photon Source at the Argonne National Laboratory. The volumetric image was constructed and corrected using algorithms developed by GSECARS that convert CT attenuation data and sinograms to 3D volumetric images (Rivers, 1998).

2.2.2 Two-dimensional Image Analysis

Pore size distributions and coordination numbers were determined from two-dimensional images, which were converted to 1-bit bitmaps by thresholding the image to separate the sediment into a population of grains, which are white or “1” and into a population of pores, which are black or “0”. Porosity was determined for each slice as the ratio of “0” (i.e., void space) value pixels to the total number of pixels in the image.

These slices were converted to “skeleton”, or one-dimensional topological representation of the pore space and to Euclidean Distance Map (EDM) images (Russ, 1999) to quantify pore throat lengths, pore throat radii, pore body radii, tortuosity factor, and coordination number (Reed et al., 2002). Skeleton images provide a means to determine the pore body locations (i.e., the junction for pore throats), the pore throat locations (i.e., the paths that connect pore bodies), and the coordination number (i.e., the number of pore throats that join at a pore body, which by definition is ≥ 3) (Dullien, 1992). EDM images enable quantification of pore body radii, as determined by the pixel count from the node of the skeleton to the pore/grain boundary, and of the pore throat radii, as determined by the pixel count from the minima EDM along the skeleton to the pore/grain boundary. The pore throat length in the 2D images is the path length distance along the skeleton between adjacent pore bodies. The full description of this method is presented in chapter 3.

2.2.3 Three-dimensional Image Analysis

Three-dimensional analyses were used to quantify pore size distributions, coordination numbers, covariance, and tortuosity factor from the entire CT volume, which was converted to a 1-bit bitmap. Porosity determined from a 2-point correlation function was equivalent to porosity determined by voxel (3D pixels) counting, which was determined from the number of void voxels divided by the total number of voxels in the image. The binary volume image is converted to a medial axis (“skeleton”) using 3DMA (Lindquist, 1996), or a one-dimensional topological representation of the pore structure, that maintains the geometrical (i.e., distance to adjacent grains) and topological (i.e., path lengths) information of the pore space. It appears as a single line of voxels, which are each located at or near the midpoint of the pore body. Medial axis voxels are determined by successive enlargement or dilation of the grains one voxel at a time until voxels from different grain/pore boundaries intersect; this path of intersecting voxels comprises the medial axis (Lindquist et al., 1996; Lindquist et al. 1999). As such, the medial axis is a one-dimensional series of converging-diverging paths. Pore body radii are determined by locating the node or intersection of the paths within the medial axis and then successively enlarging this point spherically until a grain is contacted (Al-Raoush, 2002; Al-Raoush et al., 2002). The pore body radius is the distance between the node and the pore-grain contact. The pore throat radius is determined by enlarging all the voxels along the pore throat. Then the inscribed radial dimension of the smallest inscribed sphere is determined. From these data sets, pore size distributions are determined and the permeability is predicted as explained in detail in chapter 3. Coordination number, as in the 2D images, is assumed to be greater than or equal to 3.

Traditional and image analysis methods enable the determination of porosity and permeability. Traditional methods may be used to evaluate predictions made from image analysis. A primary advantage of image analysis techniques is that they enable predictions of porosity, tortuosity, and permeability at smaller scales, at different orientations, and allow for manipulations of the images to suit evaluator needs (i.e., heterogeneity can be incorporated into an otherwise homogeneous image by enlarging or diminishing pore throats or by truncating or eliminating paths). The capability to adjust images to address specific scenarios is quite an advantage for acoustic propagation and attenuation studies that operate at high-frequencies. At frequencies >300 kHz the wavelength of the sound pulse is on the same order as the samples used to make the image based predictions. In fact, the wavelength is approaching that of the grain scale and is much smaller than the relevant scale of the traditional measurements. In the ensuing chapter these methods will be elaborated where appropriate and discussed as necessary.

CHAPTER 3. POROSITY, PERMEABILITY, AND HYDRAULIC CONDUCTIVITY FOR A SILICICLASTIC MARINE SAND: A COMPARISON OF DIRECT MEASUREMENTS AND IMAGE ANALYSIS PREDICTIONS*

3.1 Introduction

Sediment pore space geometry is often characterized by three porometric properties: porosity, permeability, and tortuosity factor (also sinuosity) (Biot, 1956, 1962; Stoll, 1989; Williams et al., 2002). These porometric properties exert significant influence on fluid motion in sediments and therefore play a major role in determining acoustic propagation in poro-elastic media, such as marine sands (Biot, 1956, 1962; Stoll, 1989; Williams et al., 2002). The significance of these and other seafloor properties to acoustic scattering, penetration, and propagation was evaluated during the Sediment Acoustics Experiment (SAX99), which was conducted in a relatively uniform sandy sediment off the Florida Panhandle near Fort Walton Beach, FL (Figure 1.4) (Williams et al., 2002; Thorsos et al., 2001, Richardson et al., 2001a). Porometric property measurements were made using traditional geotechnical (Lambe, 1951; by Briggs, 2002), electrical resistivity (Tang et al., 2002, Wheatcroft, 2002), and image analysis methods (Ehrlich et al. 1984; Koplík, 1982; Koplík et al., 1984; Doyen, 1988; White et al., 1998; by Reed, 2002).

The primary objectives of this chapter are to quantify and compare values of porosity, permeability, and tortuosity factor at decimeter to millimeter length scales using traditional geotechnical and image analysis techniques; to assess and compare spatial homogeneity and isotropy within and among individual sites; and to evaluate the accuracy of image-based porometric property predictions.

*(c) 2002 IEEE. Reprinted, with permission from IEEE J. Oceanic Engineering, volume 27, pp. 581-592, 2002.

This chapter discusses the validity of using two-dimensional image analysis to predict three-dimensional properties; and the use of an effective medium technique to make accurate, high-resolution (centimeter-scale) predictions of permeability from two-dimensional images of resin-impregnated marine sand.

Samples of quartz sand were collected in the manner described in §2.1.1 near the site of five SAX99 acoustic measurement experiments (Thorsos et al., 2001) that were south of Fort Walton Beach, FL (Figure 1.4): Benthic Acoustic Measurement System (BAMS), Sediment Transmission Measurement System (STMS), Coastal Systems Station (Lopes), Low-Frequency (LF), and Applied Research Lab-University of Texas (ARL-UT) (Table 3.1). See Richardson et al. (2001) and Thorsos et al. (2001) for more details.

Table 3.1 Coordinates of the SAX99 sites for which data are presented

Site	Latitude (N)	Longitude (W)
STMS	30° 22.671'	86° 38.695'
ARL-UT	30° 22.648'	86° 38.695'
Lopes	30° 22.578'	86° 38.657'
LF	30° 22.806'	86° 38.700'
BAMS	30° 22.680'	86° 38.802'

Porometric properties (*i.e.*, porosity, permeability, and tortuosity factor) were determined by traditional geotechnical methods as described in the previous chapter (see Ch.2 §2.1), by image analysis measurements (Ehrlich et al. 1984, White et al., 1998) and image analysis/effective medium theory modeling (Koplik et al., 1984; Doyen, 1988) for water-saturated sand.

3.2 Porometric Property Predictions from 2D Images

Predicting three-dimensional (3D) porometric properties from two-dimensional (2D) data has been addressed by many researchers for sandstone (Ehrlich et al., 1984, Koplik,

1982; Koplík et al., 1984; Doyen, 1988; Berryman and Blair, 1987; Anselmetti et al., 1998; Hidajat et al., 2000). Two basic underlying assumptions in these studies are that the structure of the sandstone is homogeneous and isotropic and that the 2D images cover an area large enough that microscopic variability (see p. 20 in Bear, 1972) does not dominate the predictions. To obtain reliable results from 2D images, the image size should be larger than the representative elemental area (REA), which is an experimentally determined sample area within which the microscopic effects average out, the macroscopic properties are realized, and the scale commences to operate on a continuum. For areas larger than the representative elemental area, average properties are independent of the area (*i.e.*, the property of “self-similarity” applies) and reflect the values for the bulk volume. For sands that were also collected in the Northern Gulf of Mexico from the Florida sand sheet, south of Panama City FL and east of the SAX99 site, porosity was shown to be self-similar for length scales from four to eleven grain diameters as based upon a fractal analysis method (Reed et al., 2000). A representative size sample was predicted to have dimensions equivalent to four-grain diameters in order for porosity to obtain a stable, asymptotic value (Bourbie et al., 1999). This was also determined to be the minimum length scale for porosity in a system of uncemented glass beads (Clausnitzer and Hopmans, 1999). The image size required to reach a stable, asymptotic value, however, may not be the same for porosity, permeability, and tortuosity factor and may not be the same in 2D as it is in 3D (Bear, 1972). Based upon the minimum length scales reported above for porosity (Clausnitzer and Hopmans, 1999; Reed et al., 2000) the image size of 3.5 mm x 3.5 mm (~8 grain diameters or 2 times the length scales determined by previous research on similar media) was selected for this

study to ensure that an REA was achieved. Thirty images for porosity and permeability and five images for tortuosity factor were used for each site. Porometric model accuracy, whether a representative elemental area is established or not, is determined by how well model predictions based on image analysis agree with measurements made by traditional geotechnical techniques. Previous researchers have demonstrated that volumetric pore space as represented in 2D images of homogeneous and isotropic sandstone is adequate to predict porometric properties values (Ehrlich et al., 1984; Berryman and Blair, 1987). Pixel counting, network modeling, and “shortest” path (*i.e.*, streamline) algorithms are often used to predict these properties. Porosity determined from 2D images as the ratio of void space pixels to the total area (Doyen, 1988; White et al., 1998) usually predicts bulk porosity (*e.g.*, water-weight loss or helium porosimetry) to within a few percent provided the image contains a representative elemental area and the sediment is not heterogeneous. The accuracy of porosity values derived from 2D images is largely controlled by the image resolution and the segmentation algorithm used to separate the image into void and grain space (Oh and Lindquist, 1999). Segmentation can be compromised by operator bias due to different selections in the segmentation (thresholding) number (White et al., 1998). Operator control, on an image by image basis, can be advantageous as it allows for a best fit approach to the data being evaluated. This alleviates variability in images that were collected under different circumstances (*e.g.*, different days and beam stability). The primary concern is that pore/grain boundaries in the segmented image are the same as the pore/grain boundaries in the SEM image. To ensure that this was the case, SEM images were overlain by transparent segmented images and boundary alignment was determined. This eliminated gross

segmentation errors, however the pore/grain boundaries pass through individual pixels. This error, while unavoidable, can be minimized with high-resolution images. Therefore, this error produces a ± 1 pixel value error in all measurements, which can be transferred into the pore size distribution determinations and the permeability predictions.

A variety of approaches have been used to successfully predict permeability from 2D images, with emphasis on combining pore geometry quantified in 2D images with established laws of fluid flow. For example, intrinsic permeability was predicted to within a factor of 2 for the Benoist sandstone using 2D image analysis techniques (Ehrlich et al., 1991a; 1991b) to quantify pore sizes, which were incorporated into a modified “bundle-of-tubes” model (Scheidegger, 1960). Permeability was also accurately predicted for glass beads and a homogeneous sandstone (Berea) using a modified version of the Kozeny-Carman equation, which established permeability as a function of image porosity, image specific surface area, and empirically determined formation factor (Berryman and Blair, 1987). Permeability for Brent sandstone was predicted to within a factor of 3 using 3D reconstructions based upon 2D-correlation functions, a simulated annealing method, and Stokes Law (Bourbie et al., 1999). In all these cases direct permeability predictions from 2D image data required empirically or implicitly determined components, presumably because 2D pore geometry (*e.g.*, coordination numbers (connectivity), pore size distributions, formation factor, and specific surface area) does not fully reflect the 3D geometry. Permeability predictions have required components that can potentially be determined from images (*e.g.*, specific surface area), but are often determined from direct measurements instead. This may in part result from the fact that determinations of these properties from images requires

additional work, from algorithms that achieve poor approximations or are less well trusted, and which have not been proved by comparative analysis with direct determinations used by more traditional approaches.

As noted previously, the tortuosity factor in sediments is defined as the average of the squared ratio of shortest path along fluid flow streamlines to a “straight line” between the start and end points of that path (p. 111 in (Bear, 1972)). Ideally, the average would be taken over the set of all end points in the sample with a separation at least as large as the side length of the representative elemental area. In practice, the tortuosity factor is obtained by averaging over only the paths that extend the full length of the 2D image and are greater than or equal to the length of the REA (Carman, 1956; Clennell, 1987).

Tortuosity factor has been determined to vary widely depending upon the analytical method used. Specifically, tortuosity factors of 6.1 have been determined by diffusion calculations for sand sized porous media (Mair et al., 1999), whereas tortuosity factor has typically been assumed to be 1.414 based upon the concept that flow paths deviate by $\sim 45^\circ$ from the direction of the pressure gradient (Carman, 1956). Tortuosity factor as determined by image analysis probably provides the most accurate method, because the flow path geometry is determined directly from the one dimensional “skeleton” that is created along the midline of the pore space.

3.3. Image Analysis and Sediment Property Predictions from Pore Geometry

High-resolution image analyses were performed on resin-cured samples. Two 1-cm-square blocks were cut from each 1-cm depth interval. The blocks were polished smooth and surfaces parallel and horizontal to the sediment water interface were digitally imaged with an Amray 1820 Scanning Electron Microscope (SEM) in backscatter electron mode.

The “parallel” block surface images are from the top 1.0 mm of the indicated depth intervals, whereas the “perpendicular” block images are from mid-depth of the interval. Image resolution (*i.e.*, pixel size) is 6.9 μm , which is quite high with respect to the size of the sand grains in this study. The ratio of image resolution to object size is an important consideration when determining the accuracy of sediment property predictions.

Digital SEM images of 3.5 mm \times 3.5 mm areas from the polished blocks (Fig. 3.1a) were converted to binary images (a 1-bit bitmap) (Fig. 3.1b) to determine pore and grain geometry using Adobe Photoshop 5.5 equipped with the Image Processing Toolkit 3.0 (Russ, 1999). Pore sizes were quantified using a calibrated length scale in UTHSCA Image Tool 2.0 (Wilcox et al., 1989). To ensure measurements overcame the microscopic effects of small sample size, an image length of about 8 grain diameters was used (*cf.* the minimum length to predict bulk porosity is approximately equal to 4 grain diameters for homogeneous sand and glass beads (Clausnitzer and Hopmans, 1999). This area provides the highest possible resolution for porosity, permeability and tortuosity factor while maintaining a representative elemental area for “clean” sands.

Pore geometry was evaluated by converting the digital SEM image (Fig. 3.1a) into a binary image (Fig. 3.1b), in which pore pixels are black and grain pixels are white using a simple segmentation technique. Porosity (n) was determined by pixel counting

Segmenting images into the grain and pore phases can lead to inaccuracies for two reasons. First, the segmentation process employs a simple thresholding technique to achieve the best fit to the image, which is always selected by “eye” and therefore is subject to operator biases. This process allows the processor to account for variable image quality that often results from fluctuating beam intensities that occur over several

hours or days of image collection. Second, some grains, especially the highly fractured ones, are invariably plucked out of the resin during the polishing process. The depressions in the resin from which the grains were plucked are “painted” white using Adobe Photoshop 5.5. To ensure that the segmented images maintained the grain-pore boundaries a simple self-consistency test was employed using Adobe Photoshop 5.5. The opacity of the segmented image was increased, while ensuring that the pore and grain shapes were still clearly visible. The segmented images were compared to the original SEM images to ensure that the pore-grain boundaries were unchanged to within a pixel of the grain boundaries.

These binary images are then duplicated so that the medial axis (skeleton) image (Fig. 3.1c) and a Euclidean Distance Map (EDM) (Fig. 3.1d) are made from the original binary image. The skeleton image (medial axis) (Fig. 3.1c) traces the central (median) path of the pore network and facilitates quantification of coordination number and pore network interconnectivity. The skeleton image (medial axis) (Fig. 3.1c) is then segmented to obtain a pore body image (*i.e.*, the junction for pore throats - not shown) and a pore throats image (*i.e.*, the bonds that connect the pore bodies - not shown). These images are laid on top of EDM images to produce pore body/EDM (Fig. 3.1e) and pore throat/EDM images (Fig. 3.1f). Pore body radii are determined from the pore body/EDM image and pore throat radii and lengths are determined from the pore throat/EDM image. These measured pore parameters are used to determine intrinsic permeability (k) using EMT (explained in section 3.4).

An important consideration in these measurements is the associated error, which is directly proportional to the resolution of the images. Each measurement is considered

accurate to within ± 1 pixel length (~ 6.9 micrometers for a 512-x-512-pixel image). In the intrinsic permeability predictions this error translates to maximum errors of a factor of 2 above or below the calculated permeability values. Hydraulic conductivity (K) was calculated using (Eq. 1.1) from modeled values of intrinsic permeability (k) (explained in section 3.4).

3.4 Effective Medium Theory for Permeability Predictions

An effective medium technique (EMT) was used to predict permeability in SAX99 sands. This technique accounts for the variable pore sizes and the average coordination number of the pore network to determine an effective pore structure, which has the conductivity of the whole system (e.g., Koplik et al., 1982; Doyen, 1988; David et al., 1990; Locke et al., 2002). This method was used to predict the permeability of quartz sand in this chapter as well as of ooid sands in Ch. 4. Initially developed to study random resistor networks (Kirkpatrick, 1973), which serve as good analogies of pore networks in sedimentary rocks (Fatt, 1956; Blunt and King, 1991), EMT is used to determine an average conducting parameter for heterogeneous disordered media (media with variable pore geometries) from the statistics of local conducting elements (David et al., 1990). Doyen (1988) demonstrated that EMT can be used to successfully predict permeability of Fontainebleau sandstone from pore geometry quantified in 2D images. His successful approach was adapted to predict permeability from high-resolution 2D images of SAX99 sands. An abbreviated version of the EMT used in Doyen (1988) and adopted for this study is described below. EMT assumes the bulk hydraulic conductivity is determined by the geometry and interconnectedness of the pore space, because the rock frame (or sediment grains in this case) does not conduct fluids. Thus the hydraulic

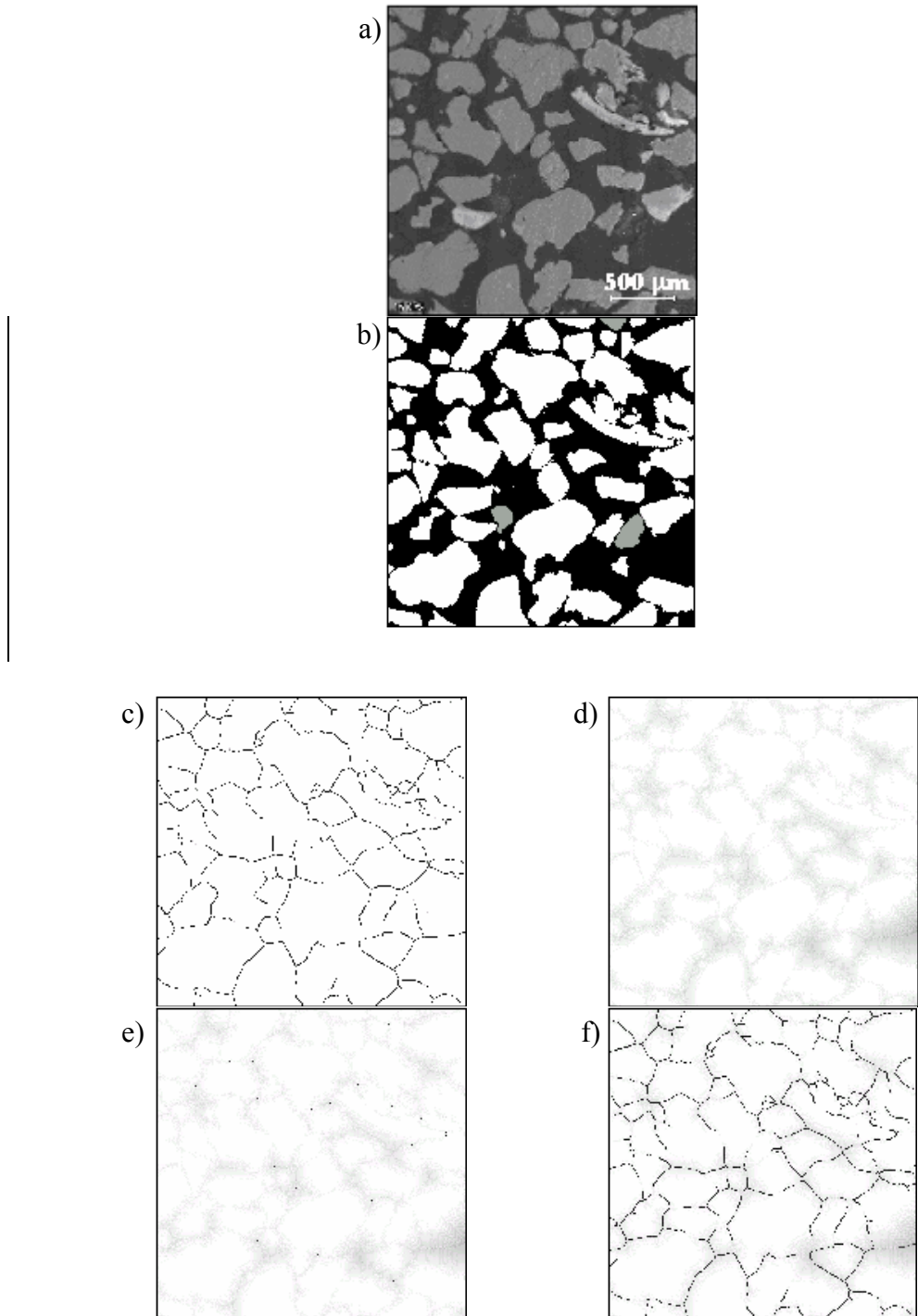


Figure 3.1. Scanning electron image (SEM) of a resin-embedded core sample is used to determine pore geometry by converting (a) SEM image into (b) a binary image from which (c) a skeleton image and (d) a Euclidean Distance Map (EDM) are created. (e) Pore body/EDM and (f) pore throat/EDM images enable the quantification of pore sizes. Coordination number is determined from (c). Images are 3.5 mm × 3.5 mm; the scale bar in (a) is 500 μm. The binary image (b) depicts pore space (black), grains (white), and plucked grains (gray). Plucked grains are painted white prior to image analysis

the system is related to total porosity, pore body and pore throat size, cross-sectional area of pore throats, coordination number, and tortuosity factor. The pore network is considered an interconnected and randomly directed grouping of cylindrical “tubes” and, in keeping with the laws for flow in circular cylinders, the cross-sectional area of the pore throats (or “tubes”) is the primary geometrical determinant of the fluid flow.

EMT assumes sediments contain a heterogeneous, non-correlated distribution of pore throats that are highly disordered. The goal of the EMT prediction is to replace the distribution of pore throat radii by a single effective pore throat radius r^* , and the objective is to determine r^* such that the total fluid flow through the pore network is unchanged for a given external pressure difference. In doing this, it is convenient to introduce the hydraulic conductance $g(r)$ (Koplik et al., 1982) for a cylindrical pore throat of radius r defined by

$$g(r) = \mu Q / \Delta P . \quad (3.1)$$

In (3.1) the volumetric flow rate Q depends on the throat radius, but that is not indicated explicitly. The hydraulic conductance for a straight, cylindrical pore throat of radius r and length l is given by

$$g(r) = \frac{\pi r^4}{8l} . \quad (3.2)$$

In this equation l is assumed to be a constant proportional to the mean grain diameter. This assumption probably overestimates the actual pore throat lengths for all sediments that exist in a closed packing.

We assume the probability distribution function of pore throat radii $n_i(r_i)$ has been determined in the form of a histogram, where r_i denotes the i th radius interval, and where $n_i(r_i)$ denotes the probability that the pore radius is within the i th interval. Then the effective pore throat radius r^* for EMT is given by the following equation (Kirkpatrick, 1972),

$$\sum_i n_i(r_i) \frac{g(r^*) - g(r_i)}{g(r_i) + [(z/2) - 1]g(r^*)} = 0, \quad (3.3)$$

which is solved iteratively to obtain r^* . Equation 3.3 is solved in MS® Excel using the “Goal Seek” function under Tools by using Newton’s method for solving the zero of a function. That is a guess is made and a solution is obtained. The derivative of this solution is obtained. From the ratio of the solution to the derivative an error is obtained. The error is subtracted from the initial guess to produce a new guess, and the process is repeated until an acceptable solution is obtained. In (3.3) z is the average coordination number (always greater than 3) for all the pore bodies; variability in z has been determined to exert a small influence in this calculation. It has been determined that conductivity values increase very gradually with increasing coordination numbers (Koplik et al., 1982). This was also demonstrated for other sandstones, such as Berea (Jerauld and Salter, 1990). The difficulty that Doyen (1988) and many others have faced is whether the coordination number determined from 2D images is representative of the coordination number in the bulk volume. Rather than use the number that was determined from the images Doyen (1988) used a value of 6 to agree with a value that is commonly used (King and Blunt, 1990; Pan et al. 2001; Jerauld and Salter, 1990). In this study the average value (i.e., $z = 3$) obtained from the 2D images was used.

Once r^* has been determined by self-consistency from Eq. 3.3, it is possible to solve for the permeability using Eq. 3.4 by replacing r by r^* and A by the area $\pi \langle r_{pc}^2 \rangle$, which represents the average pore space over which the conduction is occurring. In this case $\langle r_{pc}^2 \rangle$ is the spatial average of the square of the pore channel radius. Permeability in natural sediments is also related to sediment porosity (n) and tortuosity factor (T), which accounts for the deviation in the path length direction from normal. These parameters determined from 2D images can be incorporated into the following expression for permeability (Doyen, 1988):

$$k = \frac{n}{8T} \frac{r^{*4}}{\langle r_{pc}^2 \rangle}. \quad (3.4)$$

A tortuosity value of 1.5 was used in equation 3.3 for all permeability predictions, because this was the average measured value from several images collected from the SAX99 samples.

3.5 Results

3.5.1. Traditional Measurements

Hydraulic conductivity measured in the upper 13-cm from cores collected at the ARL-UT, BAMS, STMS, LF, and Lopes locations at the SAX99 site averaged $3.6 \times 10^{-4} \pm 0.7 \times 10^{-4} \text{ m s}^{-1}$, which corresponds to an intrinsic permeability of $3.29 \times 10^{-11} \pm 0.60 \times 10^{-11} \text{ m}^2$ (Table 3.2). All values are reported as mean \pm 1 standard deviation. At the STMS site permeability values measured at depths below 13-cm are slightly higher, likely due to an increase in the number of shell particles in those depth intervals. SAX99 sediment is well sorted, medium sand ranging from a mean diameter of 0.29 to 0.56 mm (Fig. 3.2(a)). Sediment shape based on the Power's roundness scale (1953) is sub-rounded to sub-

angular. Sediment porosity averaged 0.373 ± 0.007 ($\pm \sigma$) for all SAX99 sites (Table 3.3) and displayed only slight variability (Fig. 3.2(b)). In every case that follows, the mean values are given \pm one standard deviation (σ).

3.5.2. Predictions from Image Analysis

Sediment porosity (n) (from pixel counting) averaged 0.398 ± 0.029 (range = 0.336 to 0.478) in the top ten centimeters below the seafloor at the Lopes and ARL-UT sites (Table 3.3; Fig. 3.3). Intrinsic permeability (k) at the Lopes and ARL-UT sites averaged $2.78 \times 10^{-11} \pm 1.01 \times 10^{-11} \text{ m}^2$. Hydraulic conductivity at the Lopes and ARL-UT sites averaged $2.93 \times 10^{-4} \pm 0.74 \times 10^{-4} \text{ m s}^{-1}$ (Table 3.3; Fig. 3.4). Values of permeability in 2 intervals (0-1 and 2-3 cm) at the Lopes site and one interval (0-1 cm) at the ARL-UT site imply slight anisotropy. However, standard deviations for all other values of permeability at the Lopes (1-2 and 4-10 cm) and ARL-UT (1-10 cm) sites overlap, indicating that the sediments are fairly isotropic with respect to permeability (Fig. 3.3). Permeability predictions vary less at the Lopes site than the ARL-UT site below 5 centimeters below the seafloor. Tortuosity factor averaged 1.49 ± 0.09 in the top ten centimeters below the seafloor at the Lopes and ARL-UT sites (Table 3.3) with a range of 1.35 to 1.60 ($n = 20$). This is a reasonable tortuosity factor for sands in the SAX99 study site (Jackson et al., 1978) and for sands in general (Carman, 1956; Bear, 1972). Tortuosity factor is slightly variable in vertical and horizontal sections within and between the Lopes and ARL-UT sites.

The mean value of porosity determined by the water-weight loss technique is significantly lower (Student's t -test for equal variances) than those determined by the image analysis technique. The mean value of permeability, determined by constant head

Table 3.2. Values of hydraulic conductivity (K), intrinsic permeability (k), and mean grain size from cores collected at four locations within the SAX99 experiment area and at four sediment depths

Location	Sediment Depth (cm)	K (10^{-4} m s^{-1})	k† (10^{-11} m^2)	Mean Grain Size (phi)	Mean Grain Size (mm)
Lopes	0-13	3.9	3.4	1.43	0.37
Lopes	0-13	4.4	4.0	1.43	0.37
BAMS	0-13	3.3	3.1	1.32	0.40
BAMS	0-13	3.2	3.0	1.32	0.40
LF	0-13	4.2	3.8	1.22	0.43
LF	0-13	4.2	3.8	1.22	0.43
ARL-UT	0-13	3.9	3.6	1.29	0.41
ARL-UT	0-13	2.9	2.7	1.29	0.41
ARL-UT	0-13	4.0	3.3	1.29	0.41
ARL-UT	0-13	1.8	1.7	1.29	0.41
STMS	0-13	3.9	3.3	1.29	0.41
STMS	0-13	3.0	2.9	1.29	0.41
STMS	0-13	3.4	3.3	1.29	0.41
Average	0-13	3.6	3.3	1.32	0.40
STMS	20-33	5.1	5.1	1.09	0.47
STMS	34-45	4.8	4.7	1.02	0.49
STMS	43-55	4.0	4.0	1.14	0.45

†The conversion from K to k is not a constant proportion, because the calculation of k from (1) is dependent upon dynamic viscosity and fluid density, which change with varying temperature of surface seawater and therefore differed for measurements made on different days.

Table 3.3. Average values of porosity, permeability, and tortuosity factor from measurements made on sediments from the SAX99 sites

Direct Measurements					
Site	Porosity (<i>n</i>)	$\pm \sigma$	Permeability (10^{-11} m^2)	$\pm \sigma$ (10^{-11} m^2)	No tortuosity factor measurements were made
STMS ^a	0.373	0.008	3.29	0.33	
ARL-UT ^b	0.371	0.006	2.93	0.83	
Lopes ^c	0.371	0.008	3.69	0.28	
LF ^d	0.372	0.007	3.83	0.03	
BAMS ^d	0.377	0.007	3.07	0.05	
Image Analysis Determinations					
	Porosity (<i>n</i>)	$\pm \sigma$	Permeability (10^{-11} m^2)	$\pm \sigma$ (10^{-11} m^2)	Tortuosity factor <(L _s /L) ² >
ARL-UT (hor.) ^e	0.393	0.024	2.91	1.13	1.54
(vert.) ^e	0.399	0.018	2.85	1.10	1.45
Lopes (hor.) ^e	0.394	0.017	2.79	0.49	1.45
(vert.) ^e	0.405	0.019	2.57	0.97	1.51

^a 5 cores for porosity and 3 cores for permeability, ^b 8 cores for porosity and 4 cores for permeability, ^c 1 core for porosity and 2 cores for permeability, ^d 2 cores for porosity and 2 cores for permeability, ^e 30 images for each porosity and permeability measurement and five images for each tortuosity measurement

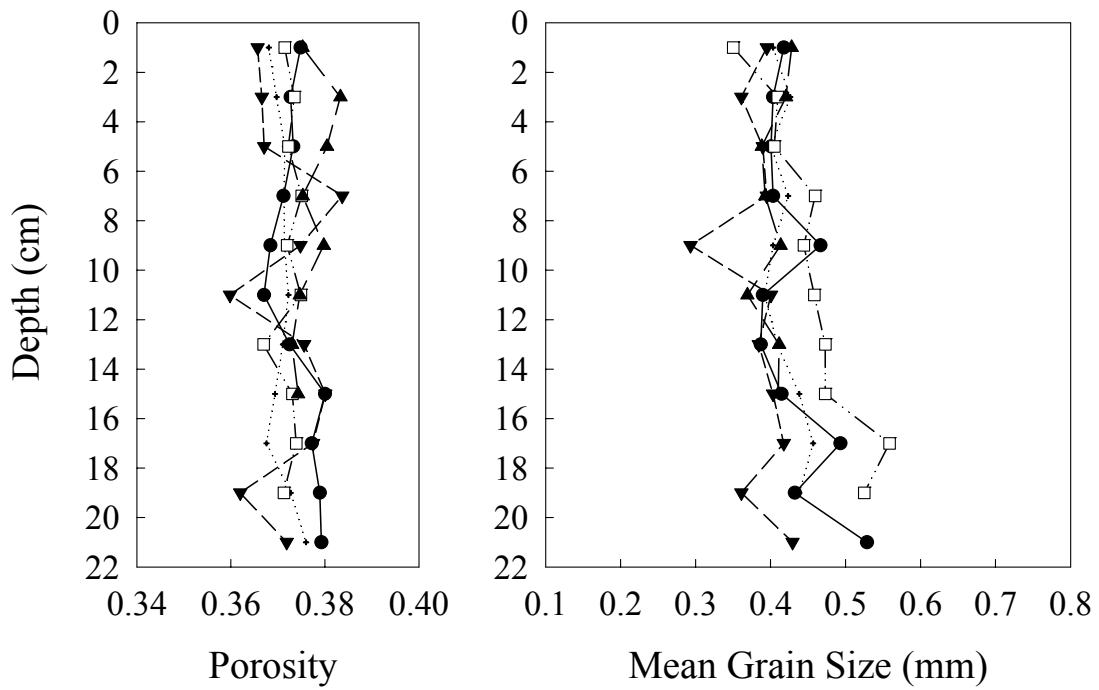


Figure 3.2. Vertical distributions of sediment porosity (from water-weight loss method) and mean grain size at SAX99 indicate slight amounts of variability. The sites are (●) STMS, (○) ARL-UT, (▼) Lopes, (□) LF, and (▲) BAMS.

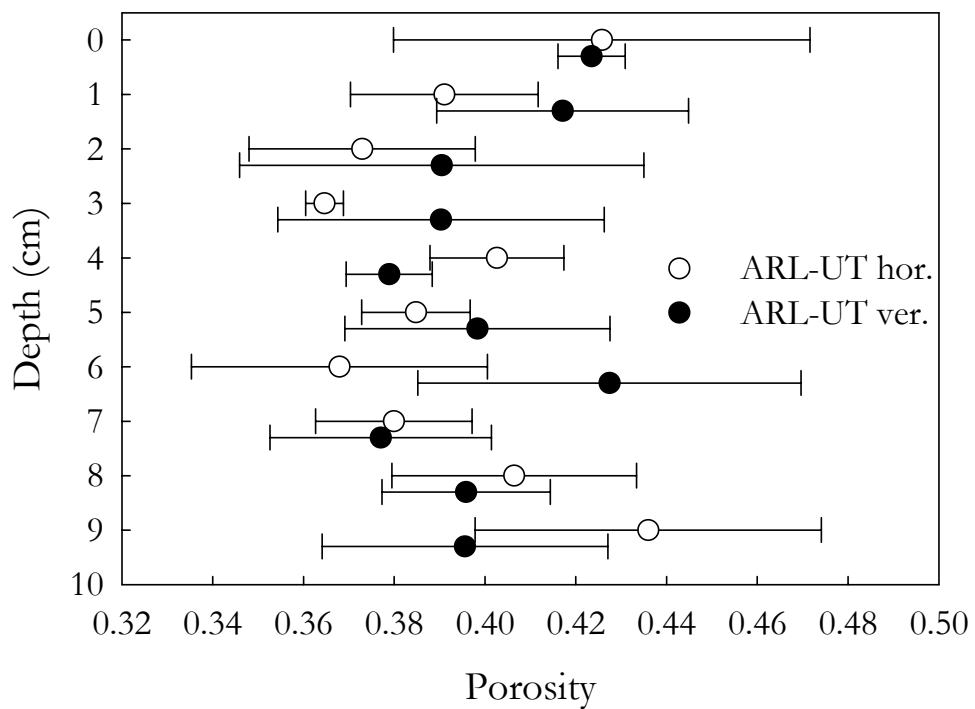
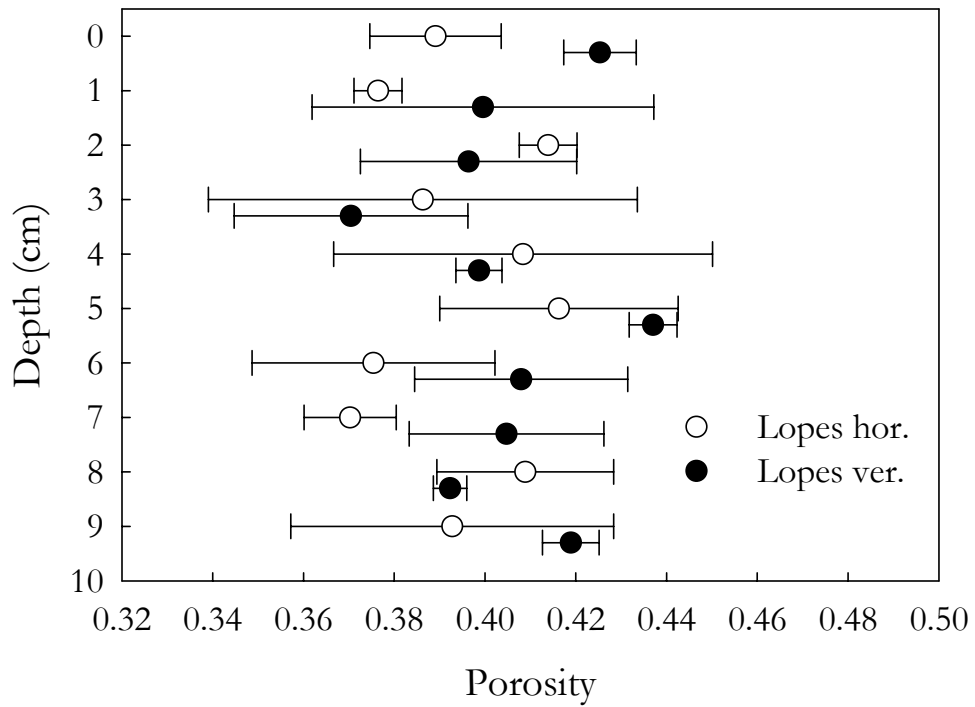


Figure 3.3. Porosity determined by image analysis (pixel counting) for the Lopes and ARL-UT sites. Error bars represent one standard deviation about the mean.

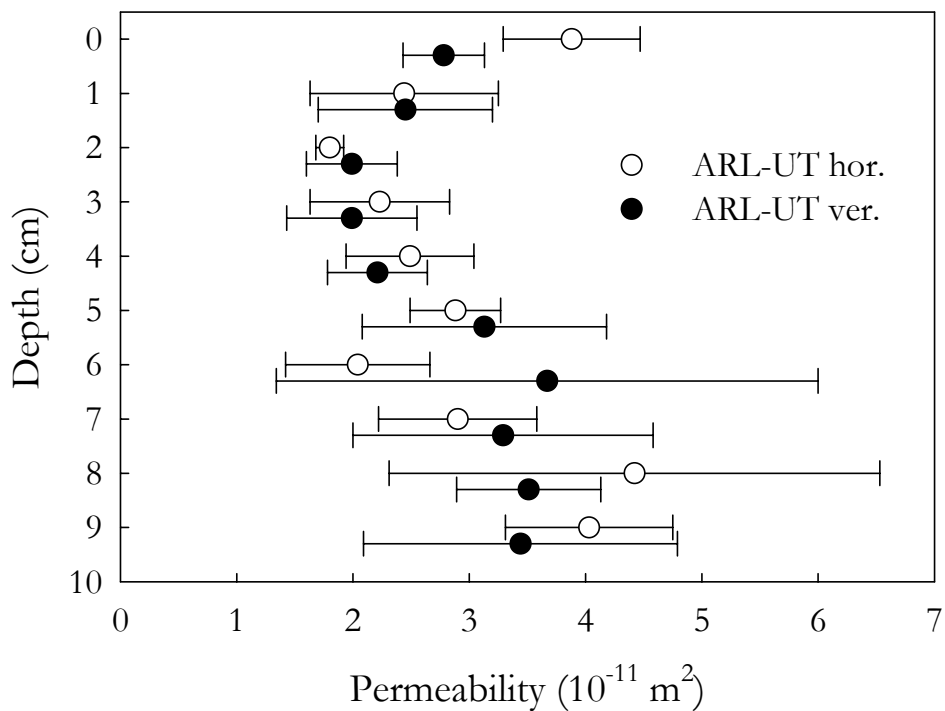
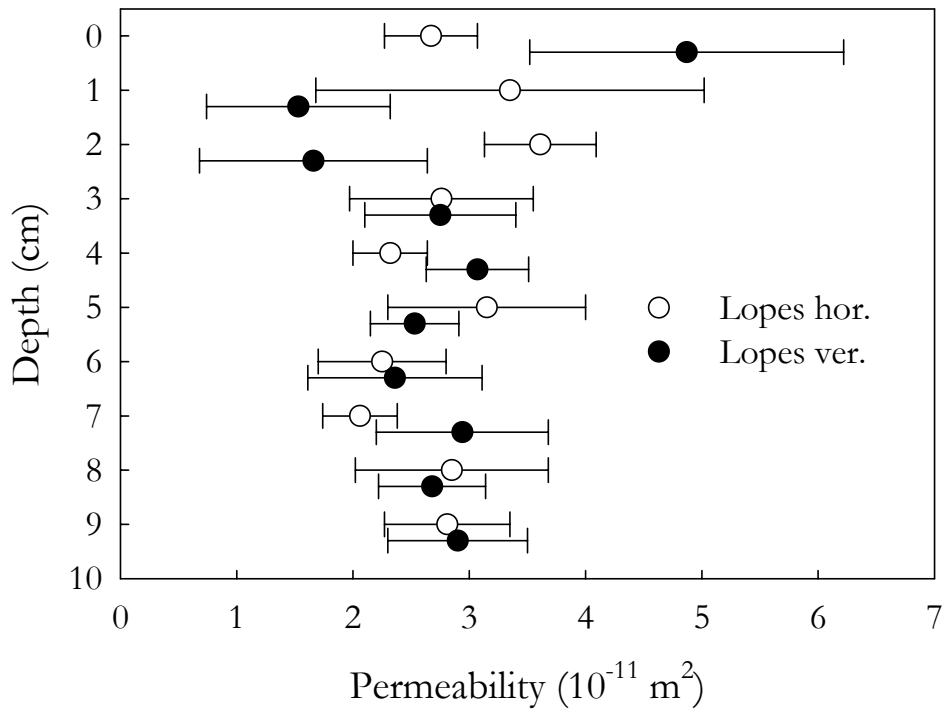


Figure 3.4. Permeability predictions from image derived pore-size distributions using the EMT technique for the Lopes and ARL-UT sites. Error bars represent one standard deviation about the mean.

permeameter measurement, is significantly higher than the mean values determined by image-analysis and EMT.

A principle objective of the SAX99 experiment was to characterize variability in sedimentary fabric and sediment properties (Richardson et al., 2001a). Variability in sediment fabric is produced by variations in grain size, sorting, consolidation, and packing, which can result in differences in pore size distribution, tortuosity, porosity, and permeability. Most images depict homogeneous and isotropic sedimentary fabric, but some heterogeneity and anisotropy are also present, especially in sediments very near the surface. To provide examples of the pore and grain size variability at discrete depth intervals several images are depicted in Figure 3.5. The porosity values for the homogeneous images (Figs. 3.5(a) and (b)) are within 0.006, whereas for the heterogeneous images porosity values differ by more than 0.08 (Figs. 3.5(c) and (d)). The pore sizes in the interval of isotropic permeability are roughly equivalent, corresponding to permeability values that differ by only $3.0 \times 10^{-13} \text{ m}^2$ (Figs. 3.5(e) and (f)). Whereas for the anisotropic sediments, as exemplified by images taken from the 0-1 cm interval of the Lopes site, the average pore sizes are more disparate (Figs. 3.5(g) and (h)), which results in a statistically significant difference of $3.26 \times 10^{-11} \text{ m}^2$ in predicted permeability values.

3.6. Discussion

Laboratory measurements of porosity and permeability are routine geotechnical characterizations of marine sediments. Issues associated with sample disturbance during sediment collection and transport, as well as water loss prior to weighing the sample, has generated criticism by some authors who question the accuracy of these measurements

for sands (Bennett et al., 2002; Wheatcroft, 2002). Laboratory measurements of porosity and permeability scale with lower frequencies and not to the higher frequencies.

Therefore, new and higher resolution approaches to measuring these sediment physical properties are needed. One such new approach is image analysis of resin-impregnated sands. Resin impregnation is required to maintain pore and grain geometry of the in situ sediment for the small samples used in image analysis. Without resin impregnation the sediment pore structure probably would be unrepresentative of the in situ sediment. That is, the sediment pore structure would reflect the changes that occurred after the core collection, but it would be indeterminate what the change would be. This change could either be consolidation of the sediment during transport due to vibration or unconsolidation of the sediment during shaking. The result of the sediment impregnation is that the in situ pore structure was maintained as best possible. In a future study, saturated sediment cores of various diameters (e.g., 1, 2, 3, and 6 cm diameters) will be imaged with computed tomography and then the core will be impregnated with polyester casting resin. The resin will be allowed to cure and then the core will be imaged. The two cores will be evaluated to determine if resin impregnation increases the sediment volume or pore space. A great advantage of this imaged-based technique is that it provides porometric properties over scales much finer than traditional laboratory methods and provides values of porometric properties at spatial scales or wavelength relevant to high-frequency acoustics. A second important advantage is that the porometric property of interest can be evaluated from a plane that is normal to the incident acoustic energy or “ray” path. This is particularly important in anisotropic sands or ones that have a large range of variability.

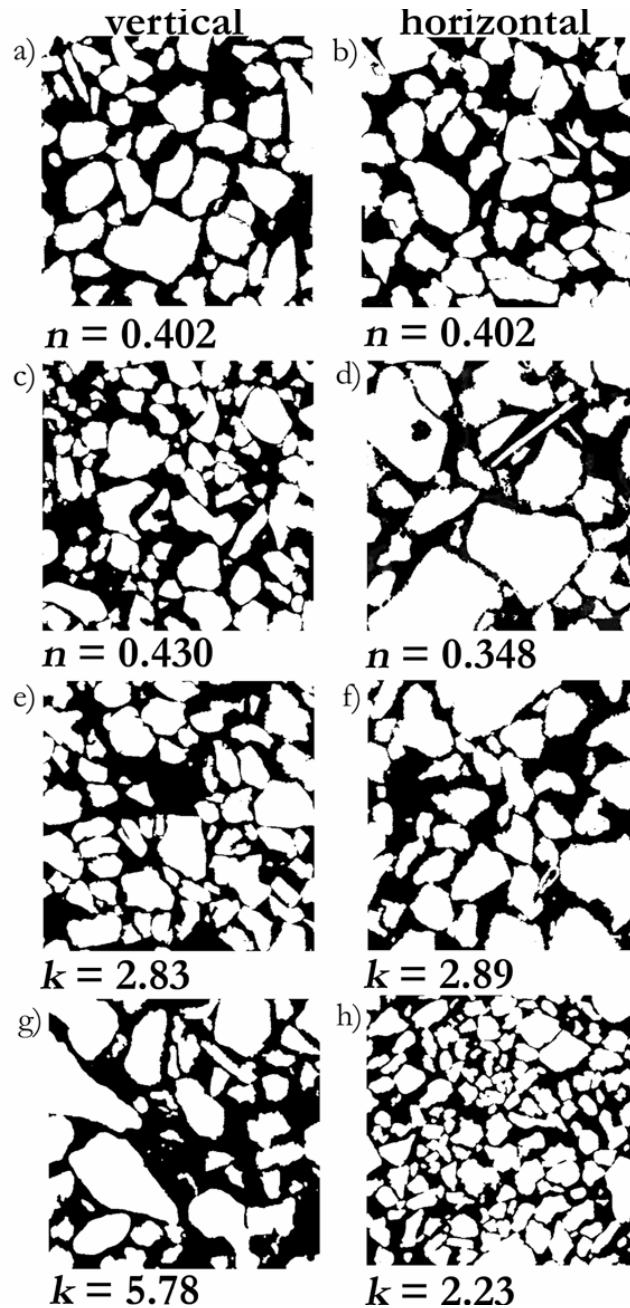


Figure 3.5. Images that depict homogeneity (a & b), heterogeneity (c & d), isotropy (e & f), and anisotropy (g & h) provide a conceptual basis to relate grain and pore geometry to porometric properties. Homogeneity is exemplified in vertical (a) and horizontal (b) images from the ARL-UT 6-7 cm interval, while heterogeneity is exemplified in vertical (c) and horizontal (d) images from the Lopes 7-8 cm interval. Isotropy is exemplified by vertical (e) and horizontal (f) images from the Lopes 6-7 cm interval, while anisotropy is exemplified by vertical (g) and horizontal (h) images from the Lopes 0-1 cm interval. Image size is 3.5 mm \times 3.5 mm. (Note: all permeability (k) values are $\times 10^{-11}$ m²). Homo- and heterogeneity are based upon image porosity and iso- or anisotropy are based upon permeability determinations

Porosity values determined by traditional geotechnical methods have lower mean, narrower ranges, and less variability than porosity determined by image analysis/pixel counting, which is not entirely surprising because the resin impregnation based techniques operate at scales that approach the pore scale (10s of micrometers) where a greater amount of variability could be expected. The lower values of porosity determined by traditional measurements as compared to image analysis measurements have been noted in other studies (Berryman and Blair, 1987; Doyen, 1988) and are likely the result of differences in the techniques, but a difference simply due to the natural variability of the sediment cannot be completely ruled out. However, the similarity of porosity values among the 5 sites where traditional water-weight-loss measurements were made (Table 3.2) suggests that natural variability in the bulk sediment (*i.e.*, larger volumes of 2-cm thick 6-cm diameter samples) is not the cause. Segmentation effects (*i.e.*, over or underestimating the pore volume or areas) may occur and slightly adjust the porosity up or down. The degree to which the porosity is adjusted up or down depends on the threshold value, the modality of the curve, where the threshold value falls on the curve, and the contrast of the image. For SEM images the contrast is sharp; pore space and grains are easily differentiated and porosity values differ very slightly for large differences in threshold numbers. For instance, a threshold number set to 117 can be adjusted up or down 5 values, with the porosity value still maintained. This is not the case for CT images, which have indistinct pore/grain boundaries and therefore require a more complicated thresholding technique (Oh and Lindquist, 1999). Greater variability in the estimates of porosity based on image analysis compared to traditional measurements probably exists due to differences in measurement scale between these two

techniques. It is unlikely that small-scale heterogeneity (*i.e.*, differences in grain sizes and total pore volume) evident in 12.25 mm² image area can be resolved in the much larger (28 cm³) volumes used for water weight-loss porosity.

There is considerable speculation on the reason for differences in porosity measured by traditional and image analysis methods in sandstone (Berryman and Blair, 1987; Doyen, 1988; Ehrlich et al., 1991b, White et al., 1998; Reed et al., 2000; Lock et al. 2002). Associated problems with segmentation include a failure to realize a representative elemental area, and sample heterogeneity. These issues also apply to unconsolidated sands found in SAX99 as well as other sand sediments, in addition to the effects of sample disturbance that are prevalent in many sampling techniques used for the collection of non-cohesive sediments such as sand. The potential problems associated with segmentation can be evaluated by comparison of grain boundaries before and after segmentation. As discussed previously, the segmentation of the SEM image is accurate to within a pixel, which translates to a maximum error of ± 0.02 . Also as discussed previously, images of SAX99 sands contain at least 8 grain diameters, which should be sufficient to achieve a representative elemental area for a homogeneous sand sample (Clausnitzer and Hopmans, 1999). However, the greater variability of imaged-based porosity compared to water-weight-loss porosity suggests that considerable small-scale variability exists (based upon evaluation of 120 images) at millimeter scales and an individual image is insufficient to reliably determine mean bulk porosity at larger scales. The combination of porosity from multiple images (30 horizontal and 30 vertical images per site) reduced the standard deviation to 0.005 and makes the combined image porosity

measurement comparable in size to the elements used for the water-weight-loss techniques.

The representative elemental size was achieved for individual images and the variability found in image-based analyses reflects small-scale variability present in SAX99 sediment at the millimeter scale, which is clearly depicted in Figure 3.5. It has also been suggested that resin impregnation may somehow disrupt sediment structure or that image analysis may not realize a representative elemental area given that the sediments may be heterogeneous at high resolution (here: 3.5 mm × 3.5 mm). To ensure that sediment structure and stability were maintained during impregnation, the sediment volume was monitored. Given that the total-core sediment volume did not change (at most 1 mm in length) in any substantial way, we assume that pore volume, pore sizes, and pore size distributions were not changed by the resin-impregnation process. Our resin-impregnation technique, which uses a direct replacement of water with resin so that the pore spaces are saturated throughout the fluid replacement, maintains pore pressures, and eliminates the increase of inter-granular stress that is associated with drying the sediments.

Traditional geotechnical measurements of porosity are subject to a different sort of criticism. Gravimetric measurements may underestimate porosity due to water loss associated with drainage and evaporation, especially during sectioning or sub-sampling. Comparisons between porosity for subsections and whole cores differ by an average of less than 0.003 (Briggs, 2002) suggesting that sectioning, if done carefully, does not result in significant water loss. Both resin/image processing techniques and traditional laboratory techniques may suffer interstitial water loss from disturbance during core

collection. This water loss should be greatest in the upper centimeter of sediment where disturbance (*e.g.*, compaction or densification) of loosely packed sediment is probably the greatest (Wheatcroft, 2002). Wheatcroft (2002) collected known volumes of sediment from 4-7 cm below the surface during SAX99 experiments in order to calibrate resistivity probes. These porosity measurements (0.37 ± 0.02) based on water-weight loss from a known volume of sediment eliminated the effects of sediment disturbance during transport and water-weight loss during laboratory manipulations, but the procedure may still compact sediment during core insertion. These measurements also excluded sediments near the sediment-water interface, which are potentially most susceptible to disturbance. The nearly identical values of porosity measured by the water-weight-loss technique used in this paper and those in (Wheatcroft, 2002) lend credence to the water-weight-loss technique.

The degree to which sediment is packed greatly impacts the sediment porosity. Maximum and minimum densities for SAX99 sediments were determined using standard American Society for Testing and Materials (ASTM, 1983) laboratory vibratory densification techniques on dried sediments. The maximum density for representative sample of tightly packed SAX99 sand (2071 kg m^{-3}) corresponds to a porosity of 0.368, which is slightly higher than the minimum image porosity of 0.336. The minimum density for loosely packed SAX99 sand (1938 kg m^{-3}) corresponds to a porosity of 0.447, which is lower than the maximum porosity determined by image analysis of 0.478.

Relative density (D_r) in percent is defined as

$$D_r = 100 \frac{e_{\max} - e}{e_{\max} - e_{\min}}, \quad (3.5)$$

where e_{max} and e_{min} are the maximum and minimum values of void ratio measured from the laboratory vibratory densification technique and e is the *in situ* void ratio. The minimum and maximum sediment densities correspond to e_{max} and e_{min} , respectively. Void ratio is related to porosity by $n = e/(1+e)$. The mean image-based porosity corresponds to a relative density of 65%. Given the range of porosities measured by water-weight-loss techniques (0.356 – 0.397) relative densities range between 66-112% with a mean relative density of 94%. If the water-weight-loss measurements are correct or slight underestimates of porosity, *in situ* sediments must be near maximum density. Underestimates of porosity would be due to compaction during core collection and water loss by drainage or evaporation (*e.g.*, 0.003 to 0.01) during sectioning. The greater relative density range of image-based porosity with respect to water-weight loss porosity is reasonable considering the differences in sample size. Relative density determinations could also be high due to the fact that maximum and minimum void ratios were determined on dry samples. Frazer (1935) demonstrated that porosity values may be 0.005 lower for subaqueously deposited and compacted samples. In spite of these problems, this study demonstrates that the mean *in situ* porosity for SAX99 sediments is probably between the values determined by water-weight loss and image processing methods (0.37 – 0.40). The inability to unambiguously determine a mean porosity value for SAX99 sands by these different methods suggests that further work is needed to resolve disparities in porosity measurements that result from these and other techniques.

Mean permeability determined from traditional geotechnical methods is significantly higher (a difference of $0.51 \times 10^{-11} \text{ m}^2$) than the mean value predicted by image analysis/EMT modeling. While the mean permeability values determined by traditional

and image analysis/EMT modeling methods are statistically different, the differences may be within the absolute measurement error of the two techniques and thus may not be physically significant. Errors in image analysis determination of porosity or pore size distribution may over- or underestimate total pore space available for fluid flow and permeability due to errors in segmentation (thresholding). The error in the porosity value can be bounded by eroding (decreasing) or dilating (increasing) the image pore space by one pixel at the pore-grain boundary and then calculating the image porosity as previously defined for each image. If the errant porosity value obtained by this process (± 0.02) is directly incorporated into (Eq. 3.4) the consequent error in permeability is on the order of $\pm 0.125 \times 10^{-11} \text{ m}^2$ (or $\pm 5\%$). If pore spaces were inaccurately segmented to produce pore sizes that are all either too large or too small (± 1 pixel), then permeability predictions would have a maximum error of 100%, which is not considered large for sands (Berryman and Blair, 1987; Ehrlich et al., 1991b; Hidajat et al., 2000) in which permeability can easily range four orders of magnitude (Fetter, 1994).

Tortuosity factor is an important determinant of transport in sediments and accurate determination of this property will aid in the prediction of fluid transport and acoustic propagation. Tortuosity factor measured by image analysis of SAX99 sediments ranged between 1.35 and 1.59 for individual images with a mean of 1.49 ± 0.09 . This value of tortuosity factor is higher than the value 1.40 that is obtained from the formation factor (F) determined from resistivity measurements for the same sediments (Tang et al., 2002) using the commonly employed relationship $T = Fn$ (Clennell, 1997), which relates tortuosity factor to the formation factor (F) and porosity (n). Image-based determination of tortuosity factor leads to very similar values compared to the prediction of tortuosity in

sands (1.5) (Jackson, 1978) in which the deflections in the streamlines are assumed to be about 45° (Carman, 1956) for nearly spherical particles (*e.g.*, glass beads).

3.7 Summary and Conclusions

Sediments at the SAX99 site appear homogeneous and isotropic from 100s of meters to a few millimeters. This large-scale homogeneity (within cores and among sites) reflects that SAX99 experiments were conducted in sediments that were well sorted evenly distributed sand most likely from the crest of a single shoreface-connected ridge. Sediments on this ridge are apparently in equilibrium, or quasi-steady state, with current hydrodynamic conditions (*e.g.*, waves and currents; Richardson et al., 2001a), which apparently create a uniform surficial deposit. Variability and anisotropy in porometric property measurements measured at the scales of the image analysis, especially in the upper 2-cm of sediment, may be due to small-scale hydrodynamic forcing (*e.g.*, grain fractionation and winnowing) and bioturbation. The large-scale homogeneity generally allows for comparison of acoustic experimental results between different sites within the SAX99 experimental site. However, small-scale variability must be characterized to facilitate high-frequency acoustic modeling subject to spatial volume heterogeneity.

The comparison between traditional and image-based values of sediment porosity and permeability demonstrates that image analysis coupled with effective medium theory can quantify sediment porosity and permeability with good accuracy at resolutions that are unobtainable with traditional measurements. In addition, the image-based analysis allowed the direct measurement of tortuosity factor within non-cohesive sediment. Tortuosity factor, an important input to acoustic poro-elastic propagation and scattering models, has been determined using these techniques, yet it is virtually unobtainable with

traditional measurements. These techniques quantify porometric property data, which demonstrates the nature of fine scale sediment volume heterogeneity within a large-scale homogeneous sand body.

CHAPTER 4. PORE SIZE DISTRIBUTIONS, TOPOLOGICAL CHARACTERISTICS, AND PERMEABILITY PREDICTIONS FROM SYNCHROTRON X-RAY TOMOGRAPHIC IMAGES OF A MARINE SAND: INFLUENCE OF IMAGE DIMENSIONALITY AND RESOLUTION

4.1 Introduction

The relationships between sediment pore space and fluid transport are complex due to the variable nature of the pore geometry (i.e., pore size and distribution) and topology (i.e., coordination numbers). Therefore quantification of pore geometry and topology in natural sand is necessary before the development of geometrically realistic porometric models and, thus, is quite valuable in the evaluation of hydraulic processes with pore-scale models that depend on these parameters. Pore geometry and topology influence modeling of hydraulic conductivity, permeability (Pan et al., 2001), hydrodynamic dispersion (de Arcangelis et al., 1986), multi-phase flow (Fenwick and Blunt, 1998; Hilpert and Miller, 2001), and acoustic propagation (Biot, 1956, 1962; Stoll, 1989; Williams et al., 2002). Quantification of pore geometry and topology in natural sand, however, is a complex problem (Lindquist et al. 1996; Liang et al., 2000) because the features that comprise the pore space are small (micrometer-scale), three-dimensional, and concealed by sediment grains.

The difficulty in quantifying pore geometry and topology of naturally occurring marine sands has led to the development of numerous pore-scale models that are based upon idealized geometry with highly correlated pore structures. This depiction provides a highly simplified representation of naturally occurring sands or sandstones (Fatt, 1956; Jerauld and Salter, 1990; Dillard and Blunt, 2000). In these idealized sediments, pore geometry is modeled as a system of interconnected, equally spaced pore bodies and pore

throats (i.e., a ball and stick configuration *sensu* Jerauld and Salter, 1990), which is constrained to a 3D cubic (Dillard and Blunt, 2000) or 2D square lattice (Fatt, 1956). The topology of the cubic lattice is also constrained so that the number of pore throats connecting to each pore body is set to 6, as would be the case for pore space bounded by perfectly spherical, mono-sized grains in a cubic packing (Jerauld and Salter, 1990; Pan et al., 2001). A coordination number of 6 has also been determined for a random placement of pore bodies on a 2D plane using a Delauney tessellation (Blunt and King, 1990). More realistic models of bulk (volumetric or 3D) sediments have used a random packing of monosized spheres (e.g., a hexagonal close packing) (Finney, 1970) for which the geometric and topological properties were carefully measured and are known. Packing zones for monosized beads have been determined to be nonuniform, dependent upon initial grain set up, and faulting that occurs during inclination of the sediment bed (Drake, 1990).

For the case of the Finney pack, Bryant et al. (1993) addressed the importance of correlation between pore throats by altering correlations in pore geometry and thus the pore geometry and topology. This transformation yielded permeability predictions that varied by a factor of 2, which indicates that correlations between pore bodies and pore throats along a flow path within this idealized sediment system impact permeability and hydraulic conductivity. These predictions are not surprising, because variation in pore sizes and topology influences conductivity of a flow path. This is also true because the cross-sectional area and the length of the flow path vary in this system. Conductivity and flow path influence such processes as drainage and imbibition, which are subject to the correlations of pore throats and pore bodies respectively (Reeves and Celia, 1996).

Similarly, it has been determined that pore body and throat correlations are important aspects to realistically representing imbibition curves in pore-scale networks where grain size distributions and porosity are matched (Hilpert et al., 2003). These pore geometry correlations become more significant as the pore-scale heterogeneity increases, such as would be expected in natural sediments, which have a grain size distribution with non-spherical and non-uniform shaped grains.

In these sediment models, solutions to volumetric flow equations are solved between adjacent pore bodies through the pore throats by

$$Q = g\Delta P, \quad (4.1)$$

where Q is the volumetric flow rate ($\text{m}^3 \text{s}^{-1}$), g is the hydraulic conductance ($\text{m}^4 \text{s kg}^{-1}$), and ΔP is the pressure difference ($\text{kg m}^{-1} \text{s}^{-2}$) across the pore throat. The hydraulic conductance for a cylindrical pore throat given by

$$g = \frac{\pi r^4}{8\mu l}, \quad (4.2)$$

is a function of pore throat length (l), pore throat radius (r), and dynamic viscosity of the fluid (μ) (Sisivath et al. 2001). It is assumed that there is no net flow in a pore body, $\sum Q_{ij} = 0$, such that the flow into a pore body (i) equals the flow out of the pore body (j), mass and momentum are conserved, and the system achieves steady state. From a system of linear equations determined from (Eq. 4.1), volumetric flow for the entire system can be solved.

To accurately determine the influence of pore geometry and topology on volumetric flow in naturally occurring sediment systems, pore sizes and topology need to be quantified and mapped or explicitly reconstructed (Blunt, 2001). The maps then serve as

the housing for pore-scale network models to predict fluid transport, so that the important correlations of pore throats to pore bodies and pore throats to pore throats can be maintained (Bryant et al., 1996). These methods can be broken down into two basic categories. In the first method, porosimetry (pore size distributions) of the porous media (e.g., lithified or unconsolidated sand) is quantified by measuring the volume of liquid (e.g., mercury or water) that drains from a sediment system at different incremental pressures over a period of time. The pressure required to displace water and allow air to fill the pore space can then be related to the average pore diameter. In the second method, 2D or 3D image data is collected (e.g., scanning electron microscopy or computed tomography, respectively) and pore geometry and topology are quantified. Two important differences in these methods are that the porosimetry methods provide information only about the narrowest constrictions leading into an area of the pore space (i.e., a cluster of pores) and neglects the larger pores within the cluster that is surrounded by smaller pores, whereas image analysis provides information on all pores within the area/volume limits of the image to the limits of the image resolution. Direct comparison of pore size distributions from porosimetry and 2D image analysis methods for the same sample indicates that large differences in pore size distributions and mean pore size values are likely (Dullien, 1975). The resulting difference in average pore throat diameters would effect predictions of hydraulic conductance (conductance scales as the fourth power of the pore throat radius: see Eq. 4.2) and volumetric fluid flow (Eq. 4.1). Also, porosimetry does not provide important information about pore sizes along a specific path, the converging-diverging nature of the pore throats, the number of pore throats that intersect a pore body, and the path length that the fluid travels. Furthermore,

for individual estimates porosimetry evaluates much larger sample volumes than image analysis. For example, $\sim 45 \text{ cm}^3$ sample of sand may be analyzed by porosimetry, whereas 0.064 to 1 cm^3 (computed tomography) and 0.16 cm^2 (SEM) samples of sand are commonly analyzed using image analysis (Lindquist et al., 1996; Dullien, 1991), so that the size of the image sample exceeds the minimum size required for bulk sediment property predictions to be accurate (Bear, 1972).

Prior to the development of high-resolution CT, image analysis of pore geometry and topology has been applied only to 2D images of sand samples. However, due to the increasing availability of high-resolution CT systems image analysis of sand samples from 3D images is becoming more common. Furthermore, increased capabilities in 3D image analysis offers an opportunity to compare 2D and 3D image analysis results and to assess the validity of pore geometry and topology determinations made from 2D images. Previous 2D image studies used comparisons between permeability predictions and direct measurements to imply that 2D images accurately reflected volumetric pore size distributions (Ehrlich et al., 1984; Doyen, 1988; Reed et al., 2002; Lock et al. 2003). While accurate predictions of sediment physical properties for quartz sand have been made from 2D planar slices (Reed et al., 2002), the similarities between 2D and 3D pore size distributions and 2D and 3D coordination numbers have not been evaluated for marine sands. Moreover, whether 2D and 3D geometry are similar and whether 2D and 3D topology are quite different in marine sand has not been adequately evaluated. In fact, the similarity between 2D and 3D pore geometry has been implied and the dissimilarity between 2D and 3D pore topology has been assumed without the determinations of pore geometry and topology for the same sample.

Three-dimensional images of sedimentary systems can be obtained with high-resolution micro-CT systems, such as the Advanced Radiation Sources (GSECARS) beamline at the Argonne National Laboratory. This system enables the collection of data that is directly constructed into volumetric images of the pore-grain structure and which maintain pore structure correlations to within the limit of the system resolution ($\sim 10 \mu\text{m}$ for an 8-mm diameter cylinder of ooid sand embedded in polyester resin). Image resolution is determined by X-ray attenuation, which is controlled by the voltage and amperage capability of the CT system, density and atomic number of the sample material, and size of the sample. X-ray attenuation is given by Beer's Law as,

$$I = I_o e^{(-\nu x)}, \quad (4.3)$$

where I is the X-ray energy reaching the imaging system, I_o is the X-ray energy produced at the source, ν is the linear attenuation coefficient (determined by density and atomic number), and x is the sample thickness. The highest resolution systems resolve features on the order of $10 \mu\text{m}$ for geologic samples that are approximately less than 1-cm in diameter, whereas other commercially available systems with different configurations (e.g., different powers, apertures or spot sizes, detector arrays) may achieve lower resolutions (Van Geet et al. 2001; Wevers et al., 2001); of these medical CT systems achieve the lowest resolution ($\sim 440 \mu\text{m}$), which is typically unsuitable for identifying pore geometry.

Adequate image resolution is a key determinant of high-quality pore geometry and topology data. Because the influence of image resolution on predictions of pore geometry, topology, and predicted permeability have not been determined for marine sands, a relationship between CT sample resolution and the robustness of permeability

and fluid flow predictions has not been established. The objective of this chapter is to evaluate the impact of dimensionality (2D vs. 3D) and resolution (low vs. high) on pore geometry, topology, and predicted permeability for a homogeneous and isotropic sand sample comprised of sub-spherical particles.

4.2. Sample Characteristics and Sample Analysis

Ooid sediments collected near Long Key, Bahamas (25° 26.85' N; 79° 11.99' W), are sub-spherical, sand-sized carbonate particles of marine origin that formed as successive layers of carbonate precipitated over a central nucleus or pre-existing layers of carbonate (Fig. 2.1). Whereas geometry of individual ooid grains is similar (i.e., ovoid but not angular) to that of spherical beads, the bulk structure of the ooid sediment system is probably more complex; ooid sand grains are packed in a disordered array that results from granular irregularities (e.g., non-uniform ovoid shapes and some inclusions of angular shells), biological activity, and grain size distribution (Figs. 2.1 and 4.1).

Ooid sediments were collected for physical property and high-resolution image analysis by scuba divers so that *in situ* properties of the ooid sediment system were preserved as much as possible as detailed in Ch. 2.1.2. Sediment physical properties were determined using traditional methods as detailed in Ch. 2.1.1.

4.3. Preparation of the Sample for CT analysis

Pore structure of the *in situ* sediments was preserved while aboard ship by embedding the whole core with polyester casting resin within 24 hours of core collection as discussed in Ch. 2.1.1. This resulted in an immobilized sample of ooid sand embedded in a matrix of polyester resin within the plastic core liner. A 0.8-cm-diameter- \times -1-cm-long subsample was cut from the center of a 1-cm disk, which was 5-6 cm below the

sediment water interface for CT imaging. The center of the disk is the area least influenced by potential sediment disturbance that occurs along the core wall during the insertion of the core into the seafloor. The subsample removed from the interval 5-6 cm below the sediment-water interface was chosen because porosity values in two adjacent cores did not vary to any appreciable degree, which suggests that the sediments in the adjacent cores was fairly well consolidated (i.e., approaching maximum density packing) at this depth (Fig. 4.2).

This subsample was then imaged by computer tomography at the GSECARS BM-13D beamline at the Advanced Photon Source, Argonne National Laboratory, where volumetric images with 11.5- μm resolution were produced (i.e., voxels have equal x, y, and z dimensions). The 11.5- μm image was constructed using algorithms developed by GSECARS that convert CT attenuation data and sinograms to 3D volumetric images (Rivers et al., 1999). A low-resolution 23.0- μm image was created by converting eight adjacent 11.5- μm voxel cubes from a high-resolution image into a single 23.0- μm voxel.

4.4 Pore Geometry Characterization and Effective Permeability Predictions

4.4.1. Two- and Three-dimensional Characterization of Pore Geometry

Two- and three-dimensional analyses were used to determine pore size distributions and coordination numbers for a CT image of an ooid sediment volume. The volume was segmented or converted to a binary image where void space is assigned a value of “0” and grain space is assigned a value of “1” using the indicator kriging algorithm contained in the 3DMA software package that is based upon the bimodal distribution of CT attenuation values (Lindquist, 1996; Oh and Lindquist, 1999).

Two-dimensional image analysis was used to determine pore size distributions and coordination numbers for individual slices, which were “peeled” from the CT volume along the *XY* plane. Porosity was determined for each slice as the ratio of “0” (i.e., void space) value pixels to the total number of pixels in the image (White et al., 1998). These slices were converted to “skeleton” images (one-dimensional topological representation of the pore space, *after* Russ, 1999), and to Euclidean Distance Map (EDM) images so that pore throat lengths, pore throat radii, and pore body radii could be determined (Wilcox et al., 1989; Reed et al., 2002). Skeleton images were evaluated to fit the scheme presented by Dullien (1992) so as to determine pore body locations (i.e., the junction of pore throats), pore throat locations (i.e., the paths that connect pore bodies), and coordination number (i.e., the number of pore throats that join at a pore body, which is always greater than or equal to 3). EDM images allow quantification of pore body radii, determined as the pixel count from the node of the skeleton to the pore/grain boundary, and of the pore throat radii, determined as the pixel count from the minima EDM along the skeleton to the pore/grain boundary. The pore throat length in the 2D images is the path length along the skeleton between adjacent nodes, minus the adjacent pore body radii.

Three-dimensional analyses were used to determine pore size distributions and coordination numbers from the entire CT volume. Porosity was determined from a 2-point correlation function, which is equivalent to voxel counting, where porosity is equal to void voxels in the volume divided by the total number of voxels in the volume. The binary volume image is converted to a medial axis (“skeleton”) that maintains the geometrical and topological information of the pore space. The skeleton appears as a

single line of voxels that are each located at or near the midpoint of the pore body. Medial axis voxels are determined by successive expansion of the grain boundaries, one layer of voxels at a time, until voxels from different pore boundaries intersect. According to Lindquist et al. (1996), the voxels intersect along the medial axis (“skeleton”), which is comprised of converging-diverging one-dimensional paths. Pore body radii are determined by locating the node in the medial axis and then successively enlarging this point spherically until a grain is contacted (Al-Raoush, 2002; Al-Raoush et al., 2002). The pore body radius is the average distance between the node and the pore-grain contact. The pore throat radius is similarly determined. Medial axis voxels are expanded radially and the radial dimension of the smallest sphere inscribed between grains is determined. The coordination number is also determined from the medial axis as the number of pore throats that intersect a pore body and it is always greater than or equal to 3 (see Lindquist et al., 2000). From these pore size distributions and coordination numbers absolute permeability is predicted.

4.4.2. Permeability Predictions by Traditional and EMT Techniques

Permeability, an important measure of transport properties in porous media, is determined by the pore geometry and topology of porous media. Moreover, permeability has been correlated to mean grain size, sorting, and textural maturity (Shepherd, 1989) as well as to porosity (Carman, 1956; Bear, 1972; Dullien, 1992). More recently permeability determinations that are based on the pore geometry and topology of the media have been made from network models. For example, an Effective Medium Theory (EMT) technique (see Ch. 3.4) has been used to quantify permeability for sandstones and marine sands from porosity, pore body size, pore throat sizes, and coordination numbers

(Kirkpatrick, 1973; Koplík, 1982; Koplík et al., 1984; Doyen, 1988; David et al., 1990; Lock et al., 2002; Reed et al., 2002).

In addition to the EMT technique, permeability was determined by two other methods using commonly obtained index properties of porosity and grain size.

Permeability was estimated by the Kozeny-Carman equation (Carman, 1956; Bear, 1972),

$$k = \frac{n^3}{(1-n^2)} \frac{d^2}{180}, \quad (4.4)$$

where n is porosity of the sample as determined from the water-weight loss technique and d is the mean grain size. Permeability was also determined by a derivation of the Hazen equation (Shepherd, 1989) for beach-dune sands,

$$k = Cd^j \frac{\mu}{\rho g}, \quad (4.5)$$

where C is a shape factor used for well-rounded sands (Shepherd, 1989), d is mean grain size, j is an exponent appropriate for grain shape and grain sorting (e.g., $j = 2$ for round and well sorted sand grains).

4.5. Results

4.5.1. Direct Measurements

Ooid sediments from the Long Key site used in this study are well sorted, medium-sized, rounded, carbonate sand (Powers, 1955) with a mean grain diameter ($\pm 1 \sigma$) of 0.337 ± 0.122 mm (Figs. 4.1 and 4.2). The mean fractional porosity ($\pm 1 \sigma$) for the ooid sand was 0.370 ± 0.007 and the mean fractional porosity of the 5-6 cm interval was 0.366 (Fig. 4.3; Table 4.1). (Because sediment porosity was determined at 2-cm intervals, the 5-6 cm CT sample should correspond to the 4-6 cm interval sample.) Hydraulic

conductivity in the top 13 cm of sediment averaged ($\pm 1 \sigma$) $4.51 \times 10^{-4} \pm 0.177 \times 10^{-4} \text{ m s}^{-1}$, which corresponds to a mean intrinsic permeability ($\pm 1 \sigma$) of $3.80 \times 10^{-11} \pm 0.149 \times 10^{-11} \text{ m}^2$ (Table 4.1).

4.5.2. Pore Geometry, Topology, and Physical Properties from Image Analysis

4.5.2.1. Homogeneity and Isotropy

An understanding of sample homogeneity and isotropy is required to make reliable volumetric sediment property predictions from 2D images (Ehrlich et al., 1984). homogeneity was determined on the high-resolution (HR) subvolumes (length of the cube edge = 12, 25, 50, 75, 100,....., 325) by voxel counting and spectral analysis of the CT-measured volume. The subvolume porosity is computed as the length, L_i , for a given side of the cube by iteration until the computed values reached an asymptotic value of 0.3650 ± 0.0100 ($n = 10$) at a length of 50 voxels. The stabilization of the value of the subvolume porosity prior to reaching the full dimension of the cube indicates that a representative elemental volume (Bear, 1972) was achieved (Figure 4.3a). Furthermore, the spectral analysis shows that variance increases only slightly from $L \approx 50$ voxels to the full sample dimension (Figure 4.3b). In addition to homogeneity, sample isotropy was determined; isotropy was determined by calculating the 2-point autocorrelation functions in the x , y , and z directions using the 3DMA software package (Lindquist, 1996). All three 2-point autocorrelation functions are equivalent and, therefore, the sample is isotropic (Fig. 4.4).

4.5.2.2 Two-dimensional Pore Geometry and Topology

Analysis of pore geometry in 2D images was used to quantify porosity, pore body radii, and pore throat radii and lengths. Porosity averaged 0.35 from the HR2D slices and

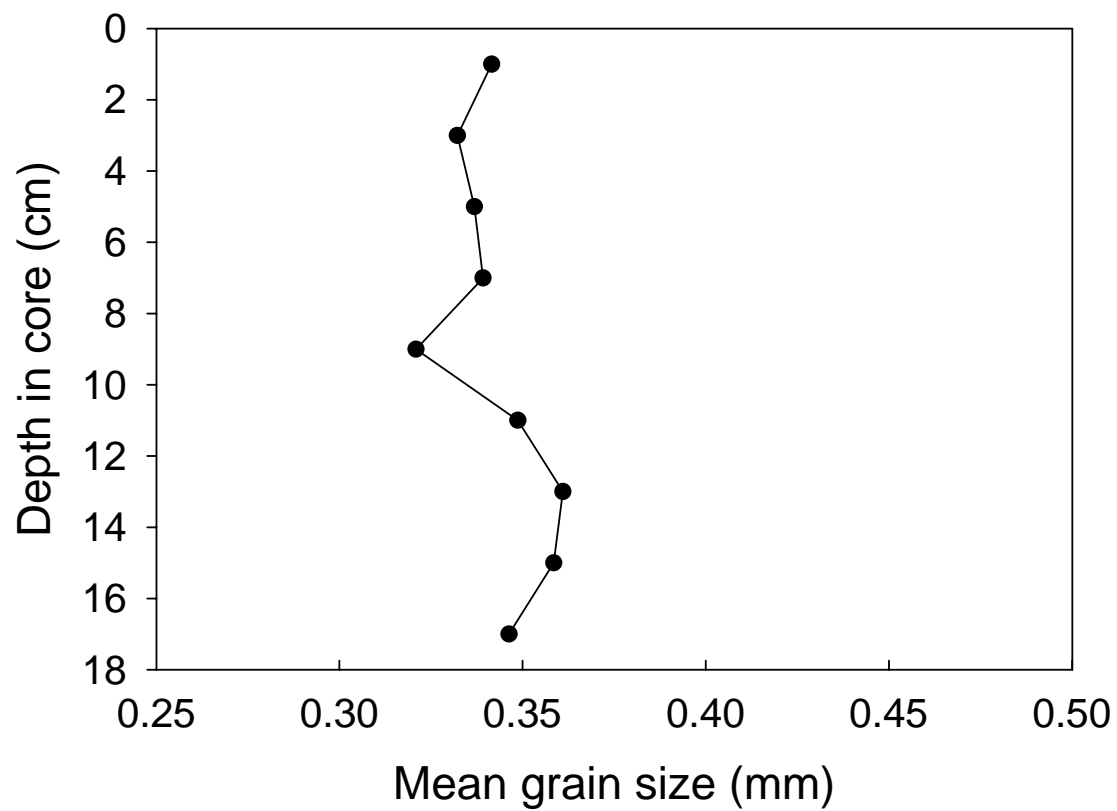


Figure 4.1. Mean grain size values for ooid sands determined at 2-cm intervals from a core collected within one meter of the resin-embedded core, which was imaged with computed tomography and analyzed with 2D and 3D image analysis algorithms

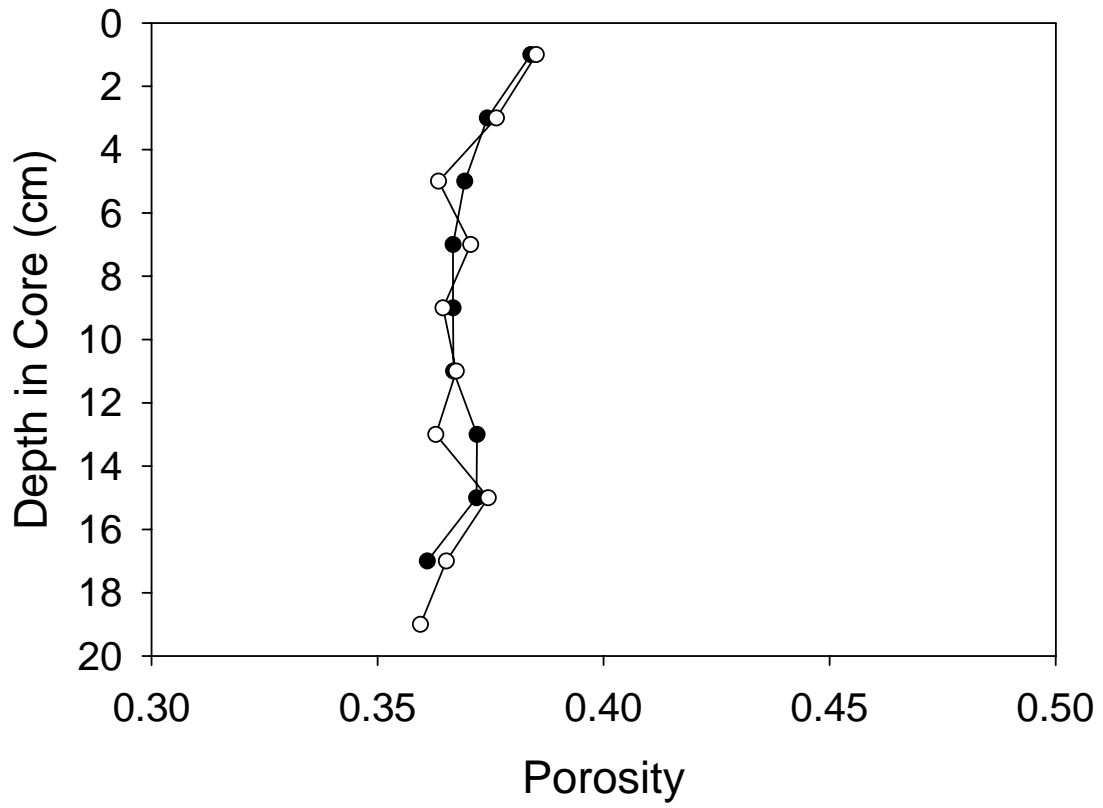


Figure 4.2. Porosity by water weight loss was determined at 2-cm intervals from two cores that were collected adjacent to the resin-embedded core

Table 4.1. Permeability and porosity measurements from direct and image analysis. Permeability presented in $2D_m$ is determined from the mean of the slice-wise-determined permeabilities and $2D_t$ is determined from all the pore throat and pore body dimensions. Hazen-Shepherd permeability (and hydraulic conductivity) assumes spherical, well sorted grains. Property values were not determined (nd) in some cases. Mean grain size and mean porosity (measured) were used to make the Kozeny-Carman and Hazen-Shepherd predictions. Permeability predictions for $z = 6$ are presented as percent overestimation.

Sample	$k (x 10^{-11} m^2) \pm \sigma$	$K (x 10^{-4} m/s) \pm \sigma$	$n \pm \sigma$	$k (z = 6)$
Lab Measurement	3.80 ± 0.149	4.51 ± 0.177	0.366 ± 0.004	nd
EMT Prediction (11.5 μm image resolution)				
3D	9.71	11.5	0.365	46.7 %
$2D_m$	6.99 ± 1.32	8.29 ± 1.56	0.35 ± 0.021	nd
$2D_t$	6.54	7.76	0.35	46.6%
EMT Prediction (23 μm image resolution)				
3D	35.6	42.2	0.381	16%
$2D_m$	44.7 ± 11.0	53.0 ± 13.1	0.39 ± 0.019	nd
$2D_t$	39.5	46.9	0.39	49.1%
Kozeny-Carman	6.48	7.68	0.3664	nd
Hazen-Shepherd	10.66	12.35	0.3664	nd

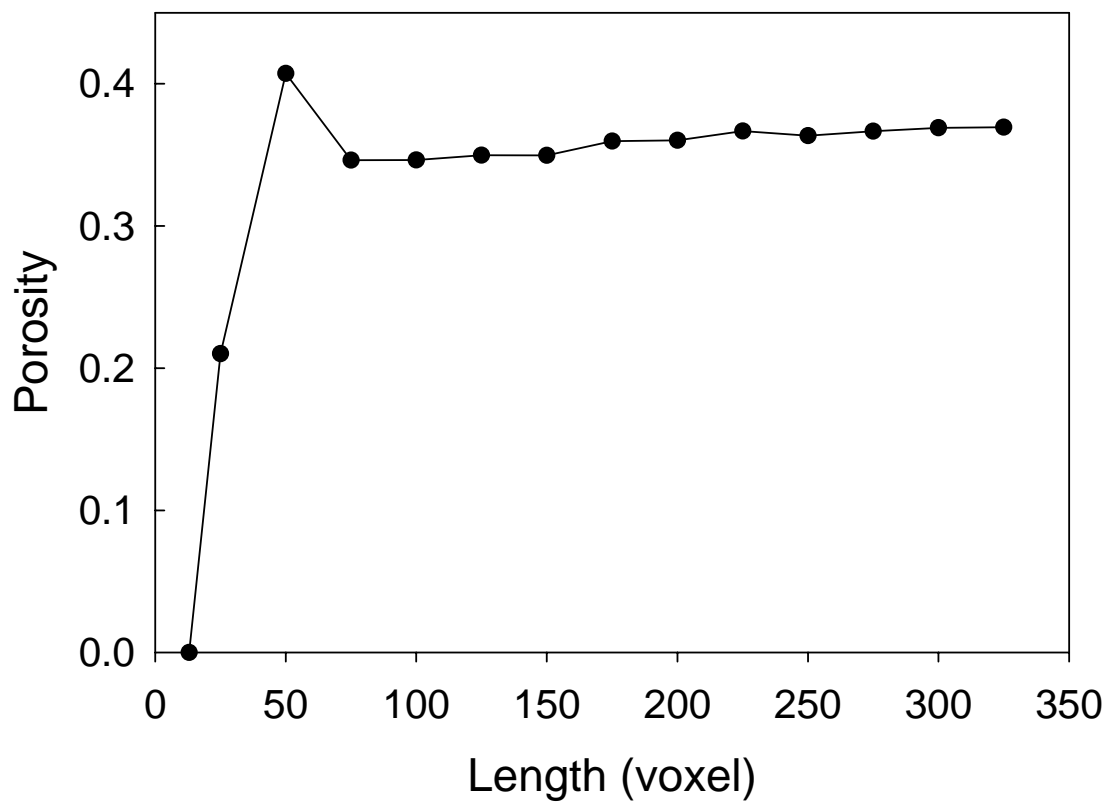


Figure 4.3a. The Representative Elemental Volume (REV) for porosity of the HR 3D sample is realized prior to reaching the minimum length ($L_x = L_y = L_z = 375$) for the sediment volume of $L_x = 375$, $L_y = 400$, and $L_z = 475$.

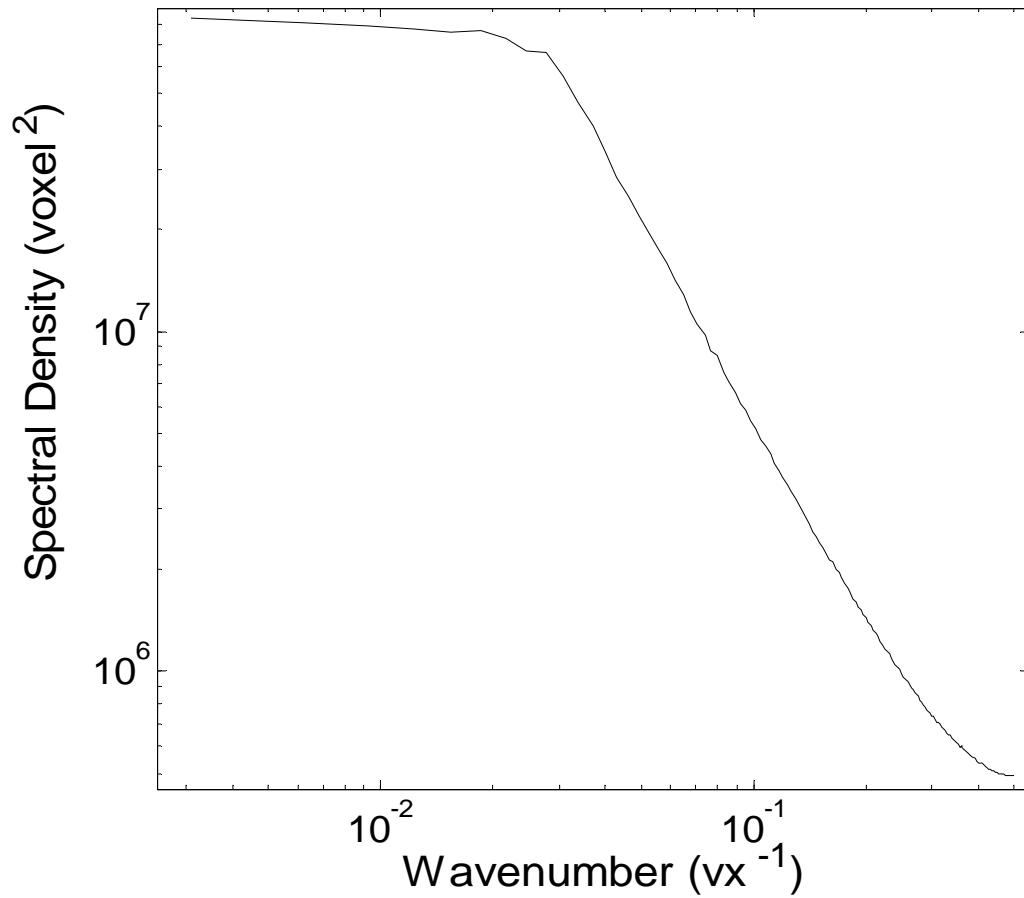


Figure 4.3b. Spectral density of the ooid CT data displays a large amount of variance in the image subvolumes bounded by edges of ≤ 60 voxels (0.690 mm) with a slight increase in variance for subvolumes bounded by edges ≥ 100 voxels (1.150 mm) and for the entire volume.

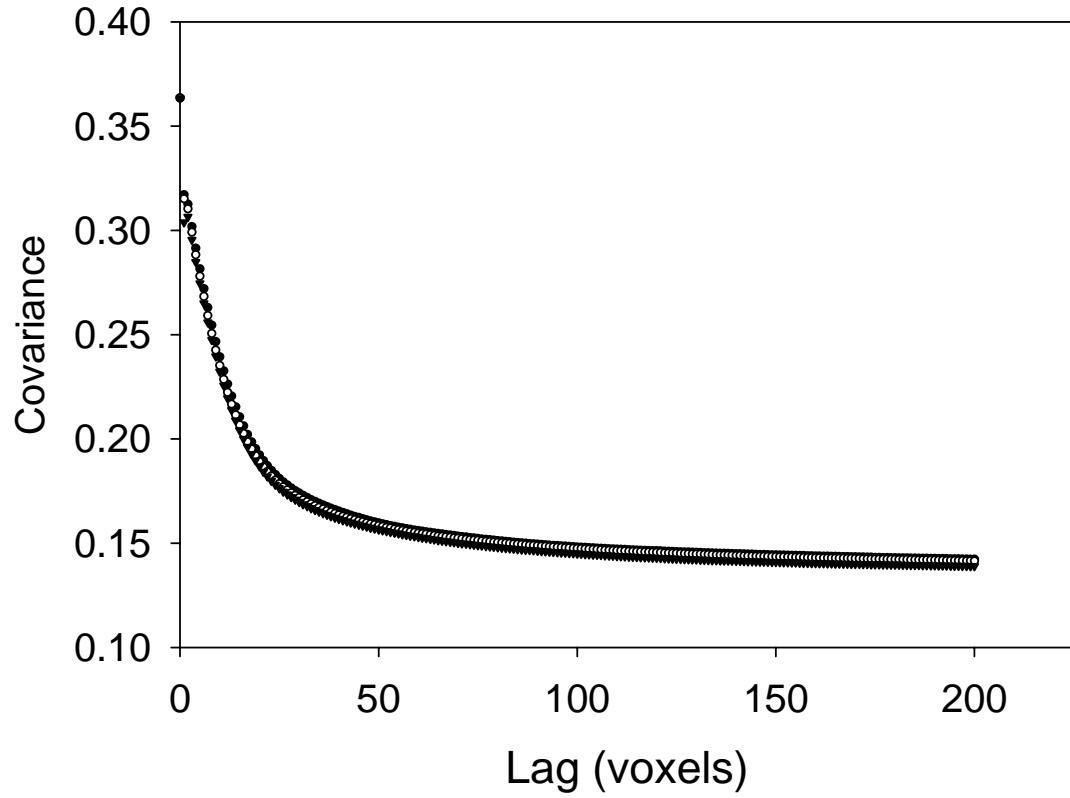


Figure 4.4. Two-point correlation functions indicate that the sample is isotropic, because the correlations in the x , y , and z -directions almost completely overlap. Data acquired from the high-resolution 3D sample

averaged 0.39 from the low-resolution (LR) 2D slices (Table 4.1). These estimates remain within the bounds of porosity values (0.33 to 0.47) typically expected for clean sands (Bear, 1972, p. 46; Fetter, 1994, p. 86).

The pore body radii distributions expected from the high-resolution 2D and low-resolution 2D images (Fig. 4.5b and 4.5d) have similar variances, means, and modes, but different median sizes (Table 4.2). Another difference between these two data sets is that there are 3 times as many pore bodies in the high-resolution sample than in the low-resolution sample (Table 4.2). Distributions of pore throat radii for the high-resolution and low-resolution samples have similar variances. However, the mean, median and mode for the distribution of pore throat radii are higher in the low-resolution sample than in the high-resolution sample by a factor of 1.3, 1.6, and 2, respectively (Table 4.2). The mean pore throat length is slightly higher in the low-resolution images than in the high-resolution images (Table 4.2). As a consequence of the shorter pore throats in the high-resolution images, there are 3.8 times as many pore throats in the high-resolution images than in the low-resolution images (Table 4.2).

For the topological characterization of the pore space, coordination numbers were determined. The average coordination number for the high-resolution and low-resolution 2D images was determined from all the coordination numbers obtained from the images for that specific data set. The average coordination number for the high-resolution 2D and low-resolution 2D samples was 3; the highest coordination number for any pore body in these images was 4, which occurs in less than 1% of the pore bodies.

EMT permeability predictions made from high-resolution and low-resolution images are directly related to mean pore throat values. Predictions of permeability were lower

for the high-resolution sample ($k_{HR} = 6.99 \times 10^{-11} \text{ m}^2$) and closer to the experimental value ($k = 3.80 \times 10^{-11} \text{ m}^2$) than for the LR sample ($k_{LR} = 44.7 \times 10^{-11} \text{ m}^2$; Table 4.1).

4.5.2.3 Three-dimensional Pore Geometry and Topology

Two-point correlation functions were used to calculate the volumetric porosity for the 3D images (Fig. 4.5). The porosity value for the high-resolution image ($n = 0.365$) is lower than the value for the low-resolution image ($n = 0.381$; Table 4.1). The primary difference in the pore body (Figs. 4.5a and 4.5c) and pore throat size distributions (Figs. 4.5e and 4.5g) is that the high-resolution 3D distribution is bimodal while the low-resolution 3D distribution is unimodal. This discrepancy between high-resolution and low-resolution pore size distributions is due to a higher frequency of pore bodies and pore throats in the 11.5- μm bin than in the adjacent 23.0 μm bin within the high-resolution 3D distribution. Although the mean pore throat lengths are approximately the same in the low-resolution and high-resolution images, the variance for the high-resolution throat lengths is quite a bit broader than that of the low-resolution images (Table 4.2). Due to transformation of a high-resolution (11.5 μm) to a low-resolution (23.0 μm), the mean pore body and pore throat sizes increase by $\sim 50\%$ and the number of pore bodies and pore throats decreases by $\sim 45\%$ (Fig. 4.5).

In addition to the differences indicated for pore geometry, there are slight differences in the topology between the high-resolution and low-resolution and between the 3D and 2D images. The coordination number is lower for the high-resolution sample ($z = 3.9$) than for the low-resolution sample ($z = 4.3$). Assuming that coordination numbers cannot be less than 3, the range of coordination numbers is from 3 to 12 for the 3D images and is much broader than the range of coordination numbers in the 2D images

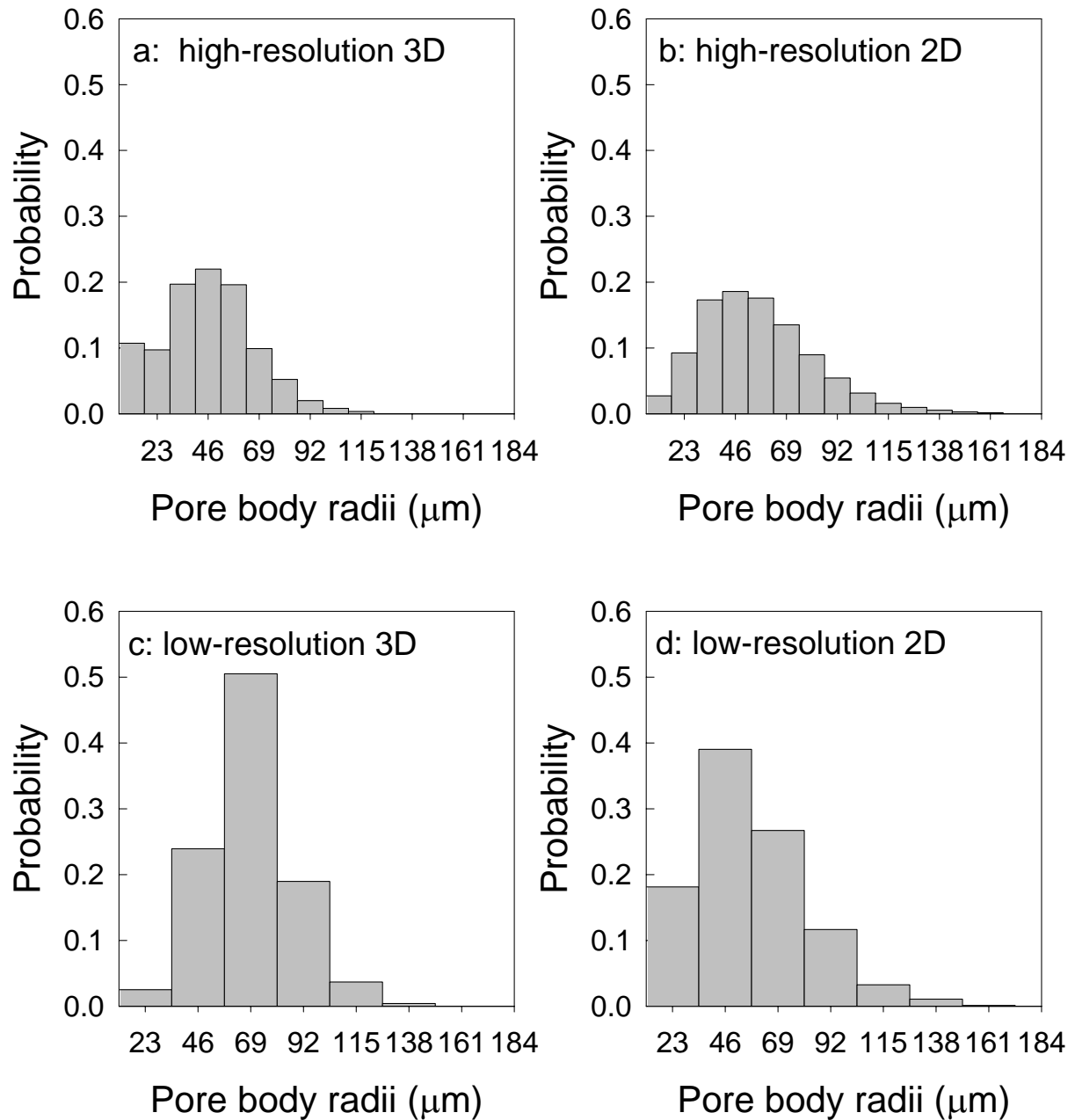


Figure 4.5. Pore body distributions from high and low resolution 3D and 2D images (a-d) display similarly shaped histograms, but a significant degree of difference in mean pore body size and pore body numbers. Pore throat distributions (e-h) also display similarly shaped histograms, but a significant degree of difference in mean pore throat size and pore throat numbers. (figure continued on next page)

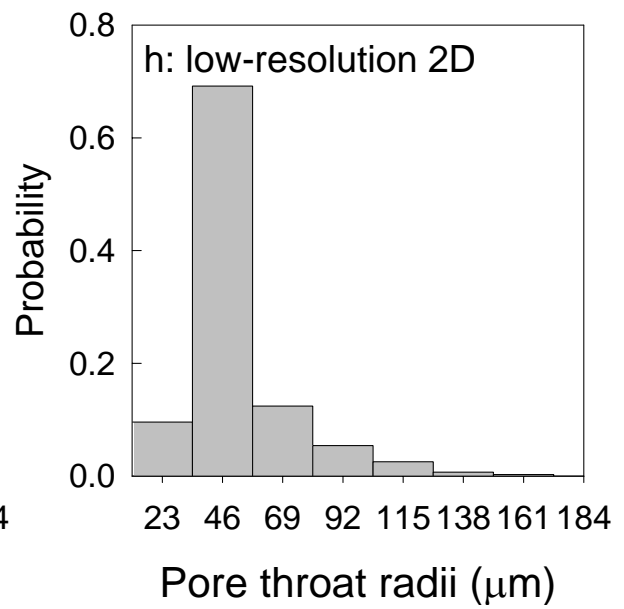
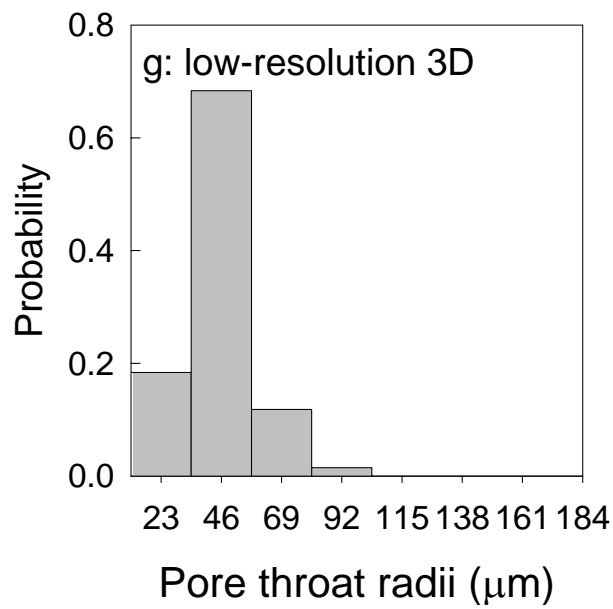
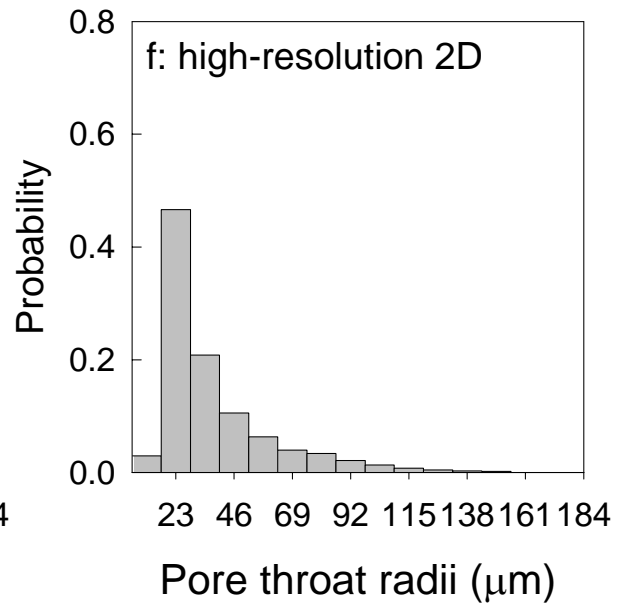
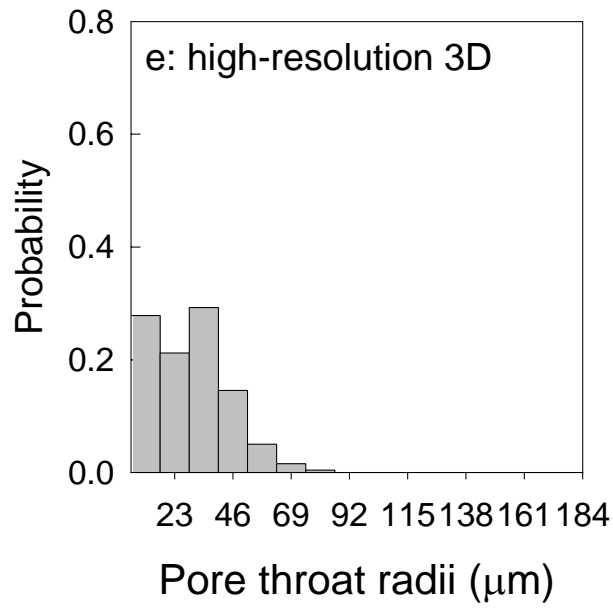


Table 4.2. Pore body and pore throat sizes and distributions for the high- and low-resolution 3D and 2D images (units for the pore sizes are micrometers)

Sample	mean	($\pm \sigma$)	median	mode	number
Pore Body Radius					
HR3D	45.8	20.8	46	46	10911
HR2D	56.4	25.6	57.5	46	88642
LR3D	68.7	19.5	69	69	4977
LR2D	56.7	25.4	46	46	29208
Pore Throat Radius					
HR3D	29.3	15.0	34.5	34.5	24013
HR2D	38.0	23.5	23	23	167520
LR3D	45.1	13.8	46	46	13089
LR2D	51.8	20.2	46	46	49452
Pore Throat Length					
HR3D	323.7	282.3	257.8	115.6	24013
HR2D	168.9	122.3	141.5	31.5	167520
LR3D	321.7	140.6	299.0	277.8	13089
LR2D	201.1	155.5	167.4	32.4	49452

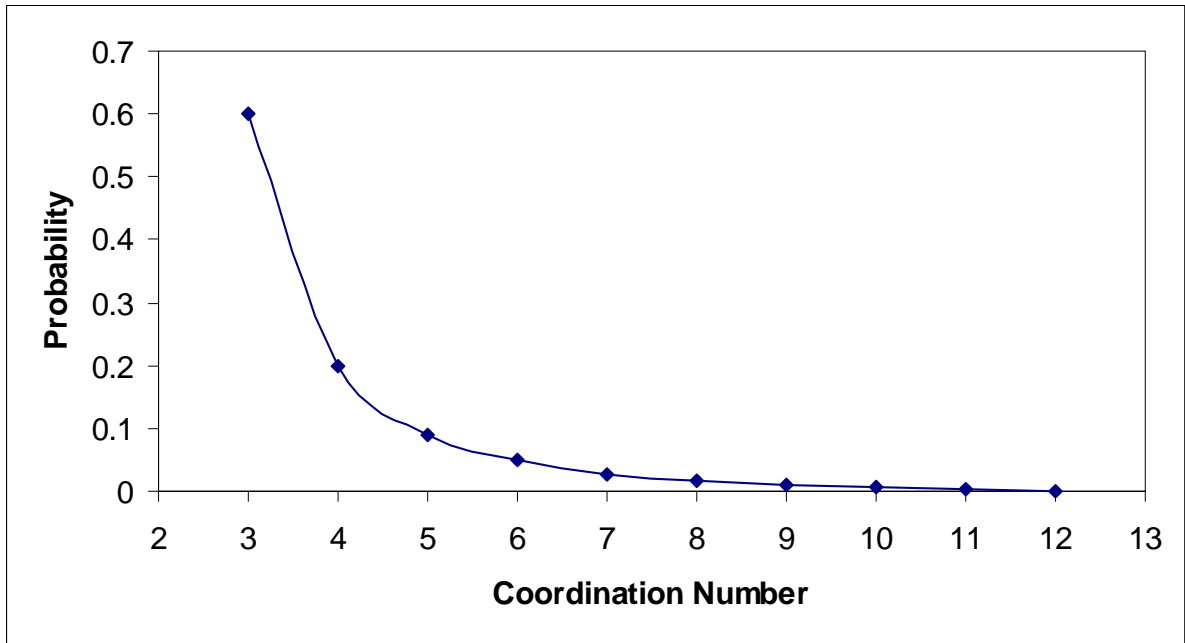


Figure 4.6. Coordination number ranged from 3 to 12 in the high- and low-resolution images of volumetric ooid sample. This plot depicts data for the high-resolution sample.

for which the probability that the coordination number was three for a pore body was 0.99 (Figure 4.6).

The EMT permeability predictions are related to the pore throat size and coordination numbers. For instance, the average permeability prediction for the low-resolution image ($k_{LR} = 35.6 \times 10^{-11} \text{ m}^2$) is more than 3.5 times higher than the prediction for the high-resolution image ($k_{HR} = 9.71 \times 10^{-11} \text{ m}^2$). Note that from Table 4.1, both high-resolution predictions are higher than the experimentally measured permeability ($k = 3.80 \times 10^{-11} \text{ m}^2$).

4.5.2.4 Permeability Predictions from Physical Properties

Permeability predictions based upon porosity and grain characteristics of the sediment interval exhibit disparate results, depending on whether the Kozeny-Carman equation (Eq. 8) or the Hazen method (Eq. 9) are used. The permeability prediction ($k = 6.48 \times 10^{-11} \text{ m}^2$) using the Kozeny-Carman equation is roughly equivalent to the EMT predictions based on the high-resolution 2D image data ($k = 6.54 \times 10^{-11} \text{ m}^2$): a factor of 2 higher than the constant-head permeability determination ($k = 3.80 \times 10^{-11} \text{ m}^2$). The permeability value calculated with the Hazen method is $10.66 \times 10^{-11} \text{ m}^2$, which is quite similar to the 3D EMT prediction where $k = 9.6 \times 10^{-11} \text{ m}^2$ (Table 4.1).

4.6. Discussion

Quantifying sediment bulk properties of permeability, hydraulic conductivity, and porosity and correlating values of these properties to sediment geometry, is critical to understanding and predicting fluid transport phenomena and acoustic propagation (Bear, 1972, Stoll, 1989; Williams et al., 2002). Determining bulk properties from pore geometry and topology quantified in 2D images has been demonstrated for sedimentary

rocks (Doyen, 1988; Lock et al., 2003), quartz sands (Reed et al., 2002) and now ooid sands. Micrometer-scale imaging and analysis of pore geometry and topology enable high-resolution (mm to cm scales), bulk property predictions that are comparable to traditional experimental data collected using hydraulic methods (Lambe, 1952). This is an important step in the determination of variability in sediment structure that occurs within bulk sediment systems and influences the physical phenomena of the larger system (Drake, 1990).

Bulk sediment properties have been predicted previously from pore geometry and topological data that were obtained from 2D images and EMT technique (Kirkpatrick, 1973; Koplík et al., 1984). The 2D approach is popular for several reasons, not the least of which is the relative abundance of 2D imaging capabilities, such as Scanning Electron Microscopy and photomicroscopy. Other reasons for the popularity of the 2D approach over the 3D approach include the large number of algorithms to quickly quantify 2D data (Lock et al., 2002). With the recent increase in 3D imaging and analytical techniques (Lindquist et al., 1996; Wevers et al., 2000; Liang et al., 2000), it is timely to evaluate the similarities and differences between 2D and 3D pore geometry and topology. This has been accomplished in this study by comparing the influence of image dimensionality on pore geometry and topology data by comparing data in a single volumetric image to data retrieved from multiple 2D images, which were removed from the 3D image.

For ooid sediments similarities and differences in the 2D and 3D pore geometry and topology for the high- and low-resolution images are distinct and quantifiable. For example, the mean values for the 2D and 3D pore body and pore throat sizes are similar for a given resolution, indicating that 2D image data is highly representative of the 3D

structure on an average basis. However, it is apparent that a significantly higher number of pore throats and pore bodies are enumerated from the high-resolution 2D image analysis than from the high-resolution 3D image analysis. This discrepancy results from successive over-counting of pore throats and pore bodies in the adjacent (z-direction) 2D images. In contrast pore throats and pore bodies are counted only once in the 3D image. This discrepancy occurs with the 2D image analysis, because each slice is separated by $11.5\ \mu\text{m}$ in the z-direction is evaluated as an independent sample, consequently pore bodies, which have an average size of $46\ \mu\text{m}$ (Table 4.2) are counted 4.5 times and pore throats, which have an average size of $29\ \mu\text{m}$ (Table 4.2) are counted 3.4 times. Thus 8 times the number of pore bodies and throats are counted in the 2D images than in the 3D images. Over-counting pore bodies and pore throats is also prevalent in the low-resolution 2D images, where 4 times as many pore bodies and 3.5 times as many pore throats appear in the 2D images than in the 3D image. The differences between high-resolution and low-resolution 2D images is due to the finer slice spacing between successive high-resolution 2D slices than between successive LR 2D slices ($11.5\ \mu\text{m}$ vs. $23\ \mu\text{m}$). Consequently, approximately twice as many pore bodies and pore throats are counted in the high-resolution 2D images than in low-resolution 2D images.

In addition to the differences in pore body and throat numbers, differences due to image dimensionality occur in the calculation of the pore throat length, which is an important parameter when considering laminar and parabolic flow where the flow scales inversely with the length of the pore throat. Pore throat length values would also be an important consideration in acoustic applications, such as acoustic propagation in porous media, and in hydrologic applications, such as hydrodynamic dispersion. Average pore

throat lengths are more than 50% longer in the 3D images than in the 2D images. This difference suggests that the 2D images are not capturing the tortuous nature of the pore throats, which are reconstructed in 3D images to extend out of the 2D plane. Because the tortuosity of the pore throats may be underestimated in 2D images, important consequences must be considered for modeling hydraulic conductance, linear flow velocities, and hydrodynamic dispersion from parameters determined from 2D images. These differences suggest that pore body and pore throat correlations should be determined from 3D images rather than from 2D images.

Coordination numbers are different in 2D and 3D images, but more similar than expected based on observed differences in pore bodies and throats. Average 2D coordination numbers for the ooid sand are about one less ($z = 3$ for 2D and $z = 4$ for 3D) than the average 3D coordination number. Typically, coordination numbers determined from 2D images are replaced with coordination numbers of $z = 6$ that occur in a sphere pack (Doyen, 1988; Lock et al., 2002). For example, Doyen (1988) determined coordination numbers from 2D images to be 3 for different samples of Fontainebleau sandstone having a range of porosities from 0.07 to 0.22. The coordination numbers were adjusted upwards by Doyen (1988) to correlate with increasing porosity by relying on the assumption that higher-porosity, homogeneous samples have larger pore body sizes and higher coordination numbers. According to this assumption, the lower coordination number for the sandstone with porosity of 0.22 was replaced with $z = 6$, which is the coordination number for a monosized sand in a cubic packing. Lindquist et al. (1999) in a 3D analysis of Fontainebleau sandstones determined coordination numbers to range from 3.37 to 3.79 for sandstone with a porosity range from 0.075 to 0.22.

Therefore, the coordination number determined by Doyen (1988) (i.e. $z = 3$) from the 2D images for the same sandstone was closer to the coordination number determined by Lindquist et al. (1999) from the 3D images than to the coordination number for a cubic packing of monosized spheres (i.e. $z = 6$). Moreover, the coordination number for Berea sandstone was determined to be 3.49 from 2D images by Koplik et al. (1982). These values of coordination number less than six are notable for several reasons: Coordination numbers are determined to be $z = 6$ in 2D Delauney tessellations (Blunt and King, 1990); are often set to six in pore-scale network models of rocks and ideal sediment systems (Doyen, 1988; Bryant et al., 1993); and are widely considered to be in the range of $4 \leq z \leq 10$ (Jerauld and Salter, 1990).

The coordination number may be directly proportional to the porosity of the media. In a 3D evaluation, Lindquist et al. (2000) found that the coordination numbers ranged from 3.37 to 3.79 in Fontainebleau sandstone with fractional porosity values ranging from 0.075 to 0.22. In a comparison of 3D images of our ooid sand and the Fontainebleau sandstone the coordination number of the ooid sand exceeded the highest coordination number of the sandstone by 0.11 and 0.49, for high-resolution and low-resolution images, respectively. Also, the fractional porosity values of the ooid sand exceeded those of the highest fractional porosity in the sandstone by 0.145 and 0.16 for high-resolution and low-resolution images, respectively. Furthermore, the coordination numbers appear to be directly proportional to the porosity in the homogenous ooid sand. This proportionality is evident in the differences observed in low-resolution and high-resolution 3D images. Values of both porosity and coordination number are higher in the low-resolution images than the values of porosity and coordination number for the high-

resolution images (i.e., 0.38 and 4.3 vs. 0.365 and 3.9). This trend is also in accord with the fact that the mean pore body size in the low-resolution 3D image is larger than the mean pore body size in the high-resolution 3D image, which may suggest that larger pore bodies, which occupy more volume, have a greater probability of being intersected by pore throats and consequently a larger coordination number.

Pore size distributions as determined from high-resolution and low-resolution data differ because of different resolutions. In the low-resolution data, the pore size distribution shifts to larger numbers because the small pore bodies and pore throats present in the high-resolution data are unresolved. The network models using the distribution derived from the low-resolution images would fail to account for the influence of smaller pores on fluid flow properties and, as a consequence, potentially overestimate factors promoting fluid flow such as the permeability and effective porosity. For the smaller pores to be included in the pore size distribution they need to be mapped in a 3D volume, so that correlations can be determined between small and large pore bodies. Thus, at low resolution these correlations, which are vital to make good predictions of the multiphase flow phenomena, would be lacking.

The X-ray Computed Tomography used in this study provides a method for obtaining high-resolution information about the sediment pore-scale heterogeneity (i.e., pores of variable sizes and shapes), which can not be measured using conventional techniques. The meaning of “high-resolution”, however, is far from established and it may be merely referring to the limitations of the imaging instrument and the size of the objects of interest. Therefore, some bounds need to be established that define “high-resolution”. Although we can not discern the division between low and high resolution in

this investigation, we can establish that the coarser resolution of 23.0 μm was insufficient, in that the derived pore size distributions provided less accurate permeability predictions based on the observation that the LR predictions were an order of magnitude higher than the averaged measured value. An additional issue associated with small sample size is whether the permeability prediction for bulk sediment volume ($\sim 3.6 \times 10^6 \text{ mm}^3$) is the same as that for the CT image volume ($\sim 100 \text{ mm}^3$). We established that the porosity over the bounding 2-cm intervals was the same porosity as the interval chosen for the CT analysis. Then we determined that the CT image was a representative elemental volume (REV), which means that the variance in the pore space, though great at minimal dimensions, decreases and then achieves stability at the full dimension of the CT sample. Establishing an REV at a length L that is much smaller than the sample used in these evaluations indicates that porometric properties were not changing significantly at the spatial scale of the pore geometry and topology determinations. This is a critical factor not only in assessing the validity of the permeability prediction, but also in addressing the validity of the pore size distributions and topological characterization from which the permeability prediction is made. This current study was limited to one sample and therefore can not account for cm-scale heterogeneities that occur in marine sands and which could produce significant permeability differences (Reed et al., 2002).

Permeability predictions made using the EMT technique from high-resolution pore geometry provide comparable permeability predictions to those made from more easily obtained grain property (i.e., mean grain size and shape factor) and porosity data. The subspherical shape of the ooid grains probably is a key factor in the success of the predictions from Kozeny-Carman and Hazen methods, because previous permeability

predictions made from these methods for angular sand were an order of magnitude higher than hydraulically measured values (Reed et al., 2002). The prediction made using the EMT method for the angular sand, however, was accurate within a factor of 2 of the hydraulically measured values. This difference in predictive capability for dissimilar grains, suggests that the simplicity of the ooid grains and the resulting packing characteristics renders them suitable to making reliable permeability predictions by the EMT, Kozeny-Carman, and Hazen methods, but that use of K-C and Hazen methods for predicting permeability in sediments with more complex grain geometry is problematic.

These efforts facilitate our understanding of the relationship between microscopic pore geometry and macroscopic processes and provide insight into the limitations of the commonly used imaging and analysis tools. Quantifying pore geometry and topology is a critical component in the establishment of network models, which effectively account for the influence of pore-scale heterogeneities on flow processes such as imbibition, drainage, hydraulic conductivity, and hydrodynamic dispersion. Pore-scale variability that occurs at micrometer scales is evident in both the 2D and 3D pore size distributions. The variability in pore size distributions and coordination numbers is due to localized heterogeneities, which suggests porous media should not be modeled universally as uniformly distributed pore body and pore throats with a constant coordination number of 6 (Jerauld and Salter, 1990; Pan et al., 2001) and that the variability in pore body radii, pore throat radii, pore throat length, and coordination number should be essential parts of a geometrically accurate pore network. The geometrically accurate pore network will necessitate use of high-resolution images that will provide a powerful tool for testing current theories that apply to processes such as acoustic propagation and attenuation at

pore/grain boundaries as well as hydrodynamic phenomena of imbibition, drainage, and dispersion.

4.7. Conclusions

Pore body and throat size distributions from homogeneous and isotropic sands that were impregnated with polyester casting resin and sub-cored for high-resolution CT analysis, provide successful permeability predictions when images of sufficiently high resolution (voxel size of 11.5 μm) are used. Image voxel size ideally may need to be on the order of one-third the mean pore size to provide reliable permeability predictions. Permeability predictions made from pore size distributions obtained from slightly lower resolutions (voxel size of 23 μm) provide predictions that are an order of magnitude higher than the hydraulically measured permeability. Permeability predictions were higher yet when made from a derivation of the Kozeny-Carman equation where only the porosity and grain size are known or from the modified Hazen-Shepherd equation, which requires porosity, grain size, and grain shape factor. Average coordination numbers ($z = 4$) determined for 3D images of higher porosity materials such as subspherical marine sand are within the range of coordination numbers determined for Fontainebleau and Berea sandstones, but are lower than the coordination numbers ($z = 6$) commonly used in network models.

CHAPTER 5. CONDUCTANCE OF GEOMETRICALLY REPRESENTATIVE PORE THROATS

5.1 Introduction

Fluid transport and acoustic propagation within porous media are governed by geometric irregularities in the shapes and dimensions of the pore throats, which conduct fluid and propagate sound. Typically fluid transport and acoustic propagation are related to sediment physical or bulk properties, which are determined at large length scales or within large volumes where the processes are continuous and local heterogeneities that exist at the pore scale have long since averaged out (\gg REV which is ≈ 8 grain diameters; Clausnitzer and Hopmans, 1999). However, these physical properties and continuum processes are controlled by microscopic scale (\sim one-seventh the mean grain diameter) heterogeneities within the pore space. These small-scale features, which are loosely categorized as pore shape geometry, influence acoustic attenuation, multiphase fluid flow, chemical transport, and sediment lithification. However, extracting pore geometry data to realistically depict pore shapes within spatially accurate pore scale network models is a challenging problem (Thompson and Fogler, 1996; Man and Jing, 2000; Blunt, 2001). This challenge primarily exists because most pore network models incorporate idealized pore shape geometries (e.g., circular cylinders) that are based upon pore entry size distributions (e.g., mercury porosimetry). These pore entry diameters may not represent the actual pore size distribution and cannot represent individual pore shapes (see Dullien, 1978). The primary justification for this commonly used approach is that model predictions can be matched to empirical determinations by randomly increasing pore throat conductances within the network. To advance research in pore shape

characterization and to address problems peculiar to porous media, accurate pore space representations are required (Patzek and Silin, 2001; Reeves and Celia, 1996; Dillard and Blunt, 2000). These representations should incorporate essential features of the pore geometry (e.g., corner angles in pore throats) (Patzek and Silin, 2001; Thompson and Fogler, 1996; Man and Sing, 2000; Sisivath et al, 2001), which may be readily extracted from 2D and 3D images. Because we seek to extract representative, yet simplified structures from these images determining the key features of individual pores, applying these features to the pore throats in network models, and then making fluid flow predictions is a challenging and important research agenda (Blunt, 2001).

A primary factor that is related to pore shape, pore geometry, and pore connectivity is the manner in which sound, fluid, and chemicals are dispersed or focused. Acoustic propagation at high frequencies is influenced by physical properties (i.e., permeability, porosity) and the underlying pore geometry (i.e., pore sizes and shapes), which influences pore fluid oscillations and direction of acoustic propagation, such that pore-scale heterogeneities promote attenuation of the acoustic signal (Biot, 1956b; Stoll, 1989; Williams et al., 2002). Biot models account for pore shape influences by incorporating a theoretical pore shape parameter that is loosely related to permeability (or conductance), yet due to problems in determining this parameter explicitly, this parameter becomes a factor that is used to fit attenuation measurements to model predictions (Biot, 1956; Stoll, 1989). To increase rigor in a Biot-based acoustic model, pore size was constrained by porosimetry data, which is pore-entry size distribution data (Yamamoto and Turgut, 1988). This was an important and progressive development, but porosimetry and image analysis provide different data (Dullien, 1978). Porosimetry that is based upon pressure

jumps is limited to pore entry diameter data or breakthrough data. It does not provide information about the variability in the pore throat. Image analysis provides pore diameter data along the entire pore, which is necessary for evaluating changes in volumetric flow within a given pore throat or porous media. In multiphase flow, pore shape (e.g., radially variant or invariant) and pore boundaries (e.g., corner angles) control displacement and migration of multiple fluids (e.g., capillary fingering or fluid replacement). However, in simple cylindrical pore tubes only a single fluid can exist as a continuum. To enable multiphase flow simulations, pore throats are depicted by tubes with corner angles (e.g., squares, triangles) (Dillard and Blunt, 2000; Patzek and Silin, 2001; Patzek and Kristensen, 2001). This enables evaluation of 2- and 3-phase flow where a wetting fluid (i.e., the one that adheres to the sediment grains, such as water) is displaced by a non-wetting fluid (e.g., oil or NAPL) (Reeves and Celia, 1996, Thompson and Fogler, 1997; Fenwick and Blunt, 1998; Dillard and Blunt, 2000; Patzek and Silin, 2000) or a gas (Oren et al., 1992, Soll et al., 1993 a and b; Hui and Blunt, 2000). In a development to maintain residual pore water values “rough” pore throats (e.g., star shaped) were constricted (Man and Jing, 2000) to a minimum at the midpoint of the pore throat. These features (i.e., pore shape roughness and pore constrictions) potentially influence sediment lithification during cementation processes (Patzek et al., 1997), probably because these features influence flow rate at nano- and micrometer scales (Kitanidis and Dykaar, 1997; Sisivath et al., 2002). It was found that electrical resistivity was significantly greater for a large constriction factor (i.e., the ratio of cross sectional areas at the pore throat opening to the pore throat minimum; sensu Owen, 1950; Jordan

and Campbell, 1986; Lock et al., 2002). It is probable that acoustic attenuation would correlate with the constriction factor in a similar manner.

It thus becomes important to isolate pore structure in the media, quantify the geometry, and predict the conductance from representative pore shapes. Since important aspects of the pore geometry, specifically the pore body radius and the pore throat minimum radius, can be determined with current imaging techniques and algorithms (Chapters 3 and 4; Baldwin et al., 1996, Liang et al., 2000; Lindquist et al, 2000; Al-Raoush et al., 2002). Incorporating one or both of these radial dimensions into commonly used pore shapes will aid in realistic assessments of flow processes and the influence that commonly used pore shapes have on interstitial processes. Thus these pore shapes can be evaluated to determine the best pore shapes to use when modeling these processes (Sisivath et al., 2001; Patzek and Silin, 2001; Patzek and Kristensen, 2001; Thompson and Fogler, 1996; Blunt, 2001). Pore geometries that have drawn pore throats as bi-conical tubes (Reeves and Celia, 1996) or hyperbolic venturi (Thompson and Fogler; 1996) with a “star-like” cross sectional tube that is constricted at the midpoint (Man and Jing, 2000) provide increasing amounts of realism to the pore shapes. While bent pores exist in porous media they are not treated in the current lattice based network models, so that they represent an unresolved problem. The difficulty in dealing with increasingly complex pore throat shapes is to obtain accurate conductances when exact solutions are not known.

In this chapter, pore throats are constructed from image data, a finite element method (FEM) is used to determine conductivity for these geometrically representative pore throats, and pore throat conductance is determined from the volumetric flow rate

solutions. The primary objective is to display that a method and means exists to accurately determine conductance for realistic pore geometries as determined from images of marine sand.

5.2 Methods

Marine sands represent a challenging sampling problem, because sample collection often disrupts the in situ grain arrangement or packing. This disruption of the in situ grain arrangement has been found to change the pore volume by 3-5% in marine sand packs. The sand packs were loosely packed, scanned with CT, and then packed or consolidated and scanned with CT. The difference in the pore volume was 3-5% (unpublished data). And while this may seem to be an insignificant factor in certain modeling applications, it is significant in acoustic correlations between field measurements (e.g., acoustic) and theoretical predictions that incorporate sediment properties (e.g., porosity, permeability, pore scale heterogeneity). Consequently this much error becomes an important factor (Williams et al., 2002). To ensure that the pore shapes are representative of the in situ sediment system, divers carefully collected cores by hand and cores were impregnated with a polyester casting resin (see Chapter 3). Impregnation of the core enabled the removal of ‘cemented’ sediments from the larger core for analysis with scanning electron microscope (Chapter 3) or computed tomography (Chapter 4). Once images were collected, the pore shapes were characterized from skeleton (Doyen, 1988; Lindquist, 1996; Liang et al., 2001) or medial axis images to produce qualitative information about pore throat convergences.

Qualitative assessment of pore shapes Figure 5.1 (Scanning Electron Microscopy) and Figure 5.2 (Volumetric Medial Axis)) and quantification of pore data (see Chapter 3)

was used to determine pore throat length/pore throat radius and pore body radii/pore throat radii aspect ratios from more than ten thousand pore body radii and pore throat radii and lengths. From these determinations the representative pores in this study were chosen to have pore throat lengths of 100, 150, and 200 micrometers in length; the pore throat radii ranges were chosen to be 20, 30, 40 and 50 micrometers; and the pore body radii were fixed at 50 micrometers. This provides a range of pore body/pore throat aspect ratios (also “constriction factor” (sensu Owen, 1950)) of 1, 1.25, 1.67 and 2.5. Pore conductance for these shapes can be determined by implementing a FEM scheme to solve the unidirectional volumetric flow rate by application of the Navier-Stokes equation for Cartesian coordinates in the z -direction:

$$\rho \left(\frac{\partial w}{\partial t} + u \frac{\partial w}{\partial x} + v \frac{\partial w}{\partial y} + w \frac{\partial w}{\partial z} \right) = -\frac{\partial P}{\partial z} + \rho g + \mu \left(\frac{\partial^2 w}{\partial x^2} + \frac{\partial^2 w}{\partial y^2} + \frac{\partial^2 w}{\partial z^2} \right). \quad (5.1)$$

where u , v and w are the flow velocities in the x -, y -, and z -directions respectively, ρ is the fluid density, and t is time.

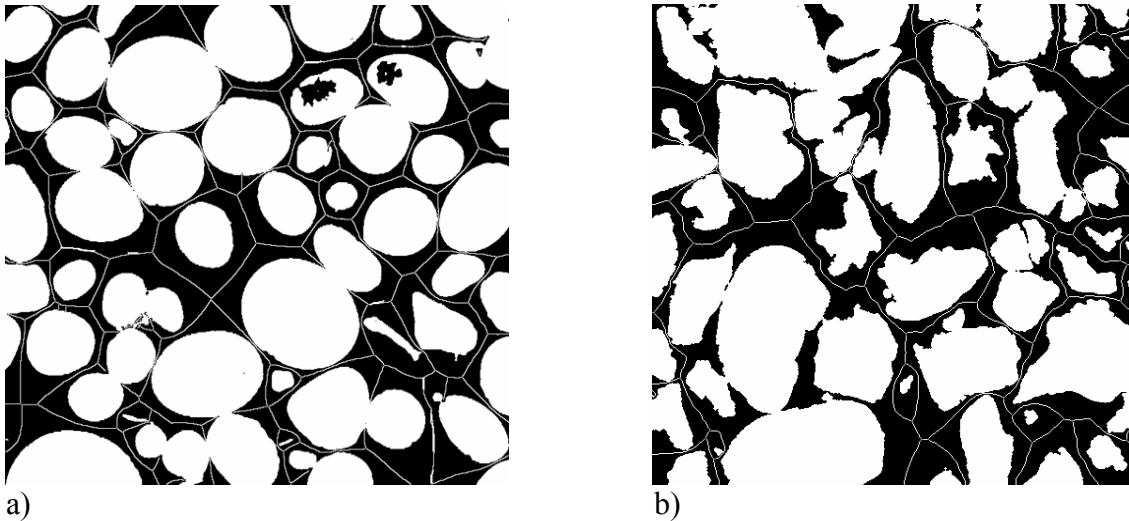


Figure 5.1. A binary SEM image of the sand has the skeleton (white lines) imposed on the pore space (black), which is bounded by grains (white) for the (a) ooid sand collected from Long Key, Bahamas, and (b) quartz sand collected from the south of Fort Walton Beach, FL in the Northern Gulf of Mexico.

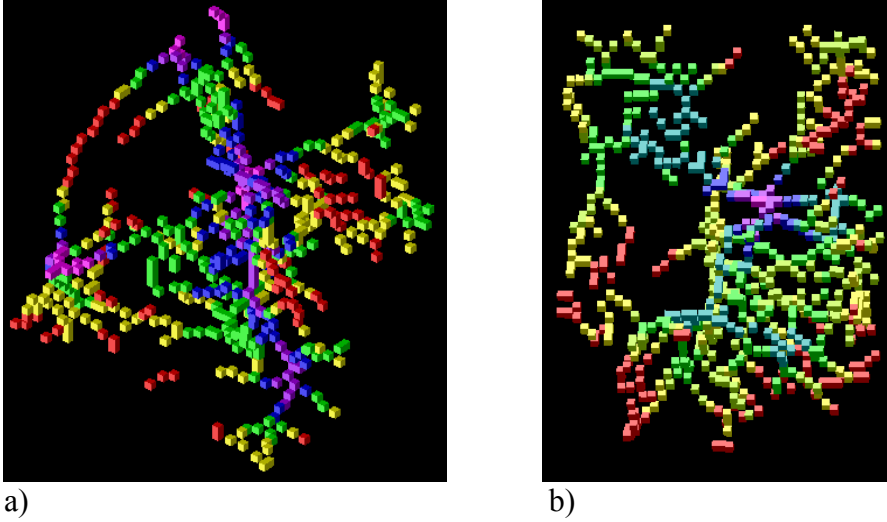


Figure 5.2. Volumetric pore space displayed as one-dimensional medial axis images for a small section (40 voxels on a side) of (a) ooid sands collected from Long Key, Bahamas, and (b) quartz sand collected from the Northern Gulf of Mexico south of Fort Walton Beach, FL. In the skeleton image the color code indicates relative cross sectional dimension with violet largest and red smallest.

For slow, laminar, and creeping flow (i.e., Reynolds's numbers are less than 10) that does not vary with time, equation 5.1 simplifies to

$$\mu \left(\frac{\partial^2 w}{\partial x^2} + \frac{\partial^2 w}{\partial y^2} \right) = - \frac{\partial P}{\partial z} + \rho g . \quad (5.2)$$

Because the pressure difference (dP) and the throat length (dz) are fixed in these representations and there are no body forces, Equation 5.2 is further simplified to Poisson's equation,

$$\frac{\partial^2 w}{\partial x^2} + \frac{\partial^2 w}{\partial y^2} = \frac{1}{\mu} \frac{\Delta P}{L} . \quad (5.3)$$

In these equations ρ is the fluid density, w is z-component of flow, and μ is the fluid dynamic viscosity. FEMLAB, a finite element problem solver with a built in Computer Design Program (CDP) for drawing various shapes, is incorporated into

Matlab was used to draw simple representative pore shapes and then solve the volumetric flow rate (Q) (Eq. 5.2). The integral volumetric flow rate at the outflow was obtained as the representative flow for the established pore throat for the following boundary conditions; (1) fluid flow was straight in and straight out; (2) a fixed pressure difference was supplied across the length of the pore throat; and (3) a no-slip boundary condition was imposed on the pore throat walls. The Reynolds's numbers for these systems ranged from 1 to 6. Fluid density and dynamic viscosity were supplied as subdomain conditions. The pressure difference, fluid density, and fluid dynamic viscosity were scaled to the dimensions of the pore throats (*i.e.*, micrometer scale). Supplied pressure differences ranged from 0.1 to 100 kPa (10^{-4} to 1 atmospheres), which was imposed to replicate potential pressures differences across the pore throat as well as to ensure that the flow was laminar. Conductivity for this specific pore throat geometry was determined by

$$g = Q/\Delta P \quad (5.3)$$

where conductivity of the pore throat (g) is proportional to the integral volumetric flow rate (Q) at the exit of the pore throat, and inversely proportional to the pressure difference (ΔP) across the pore throat.

The values obtained from these solutions were compared to the exact conductance for circular (Eq. 5.4), square (Eq. 5.5), and triangular (Eq. 5.6) cylinders (Bear, 1972, Sisivath et al., 2001) to determine the accuracy of the solution. Error estimates were then determined for each shape by calculating the difference between the FEM conductance and the exact conductance divided by the exact conductance. These are presented on a

percent basis after conductance error was multiplied by 100%. The exact conductance of a circular tube is

$$g = \frac{\pi r^4}{8\mu l}, \quad (5.4)$$

where r is the pore throat radius and l is the pore throat length. Adapted from work by Sisivath et al. (2001) in which the conductance for various 2D cross-sectional shapes was determined. The exact conductance of a square tube would be

$$g = \frac{0.422l_e^4}{12\mu l}, \quad (5.5)$$

and the exact conductance of a triangular tube would be

$$g = \frac{\sqrt{3}l_e^4}{320\mu l}, \quad (5.6)$$

where l_e is the edge length and μ and l were defined previously.

The conductance of representative pore throats was then determined from these equations for circular, square, and triangular pore throats where the ratio of pore length (l) to pore throat radius(r) was incorporated and the pore throat radius was constant over the entire length of the pore throat (*i.e.*, the constriction factor was equal to 1). The volumetric flow rate was also determined through these shapes (Eq. 5.3) and the conductance values for each shape as determined by the two methods were compared. Based upon the accuracy of the solutions (error ranged from 0.01-2.53%) it was then deemed reasonable to use this same procedure to determine conductance of constricted pore throats (*i.e.*, hourglass shapes) for which exact equations have not been determined. The primary difference between the hourglass shape and the other shapes (*i.e.*, circle, square, and triangle) was that the constriction factor ranged from 1 to 2.25 for the

hourglass shape, but was constant at 1 for the other shapes. Constriction factor was determined from pore throat and pore body radii quantified in 2D images of ooid and quartz sand.

5.3 Results

Qualitative analysis of the skeleton overlay on the pore space from the 2D images indicates that the pore throats converge to a minimum dimension away from the pore body and then diverge from the minimum to the adjacent pore body. This finding is substantiated from the medial axis image collected from the CT images, where pore body cross sections are typically larger than pore throat cross sections. Quantitative analysis of pore throat lengths, pore throat radii, and pore body radii indicates that pore throat lengths are 3 to 6 times the pore throat radii (average 4 to 5) and pore body radii 1 to 2 times the pore throat radii (averaged 1.4 to 1.5) (Table 5.1). In the case where the mean pore body radii was 1 times the mean pore throat radii, the pore throat can be represented by a straight cylinder.

Once the pore throat shapes were defined it was determined that the flow was laminar for all cross-sectional shapes as indicated by symmetric and parabolic flow patterns. As expected, within the radially invariant pores fluid flow velocity displays a constant parabolic profile along the length of the throat (Figures 5.3a, b, c). The bent pore throat (same radial dimension and length as the circle pore throat) has the same flow velocity as the circle pore throat for each pressure difference. In contrast, the fluid flow within the the hourglass pores is approximately 2.0 times slower at the inflow and outflow than it is at the constriction. Specifically in the case of the three biconical pore throats with lengths of 100, 150, and 200 μm , the velocity at the central portion of the constriction is

Table 5.1. Average dimensions of pore throat length (T_l), pore throat radii (T_r), and pore body radii (B_r) for quartz and ooid sands collected from the marine environment. Dimensions are in micrometers. Aspect ratios of T_l/T_r , T_r/B_r (also constriction factor (Owen, 1952)), and T_l/B_r from 2D images of quartz and ooid sands

Quartz sands										
T_l	166	164	156	153	120	166	145	142	155	155
T_r	38	42	46	42	35	38	36	41	41	41
B_r	58	67	70	61	64	58	57	61	61	62
T_l/T_r	4.4	3.8	3.4	3.6	3.4	4.4	4.0	3.4	3.8	3.8
B_r/T_r	1.5	1.6	1.5	1.5	1.8	1.8	1.6	1.5	1.5	1.5
T_l/B_r	2.9	2.5	2.2	2.5	1.9	2.9	2.5	2.3	2.5	2.5
$\langle T_l/T_r \rangle$	3.8 ± 0.4 (mean ± 1 σ)									
$\langle B_r/T_r \rangle$	1.4 ± 0.1 (mean ± 1 σ)									
$\langle T_l/B_r \rangle$	2.5 ± 0.3 (mean ± 1 σ)									
Ooid Sands										
T_l	123	169	160	157	152	136	151	153	157	156
T_r	22	37	37	25	34	29	31	35	35	34
B_r	51	55	54	43	35	29	53	48	47	48
T_l/T_r	5.6	4.6	4.3	4.5	4.5	4.7	4.8	4.4	4.4	4.6
B_r/T_r	2.3	1.5	1.5	1.8	1.0	1.0	1.7	1.4	1.3	1.4
T_l/B_r	2.4	3.1	3.0	3.7	4.3	4.7	2.9	3.2	3.3	3.2
$\langle T_l/T_r \rangle$	4.6 ± 0.4 (mean ± 1 σ)									
$\langle B_r/T_r \rangle$	1.5 ± 0.4 (mean ± 1 σ)									
$\langle T_l/B_r \rangle$	3.4 ± 0.7 (mean ± 1 σ)									

Once the pore throat shapes were defined it was determined that the flow was laminar for all cross-sectional shapes as indicated by symmetric and parabolic flow patterns. As expected, within the radially invariant pores fluid flow velocity displays a constant parabolic profile along the length of the throat (Figures 5.3a, b, c). The bent pore throat (same radial dimension and length as the circle pore throat) has the same flow velocity as the circle pore throat for each pressure difference. In contrast, the fluid flow within the hourglass pores is approximately 2.0 times slower at the inflow and outflow than it is at the constriction. Specifically, the three biconical pore throats (lengths of 100, 150, and 200 μm), the maximum velocity is 2.89 (Fig. 5.5a), 2.35 (Fig. 5.5b), and 2.77 (Fig. 5.5c) times as fast as flow at the entry or exit of the same pore throat.

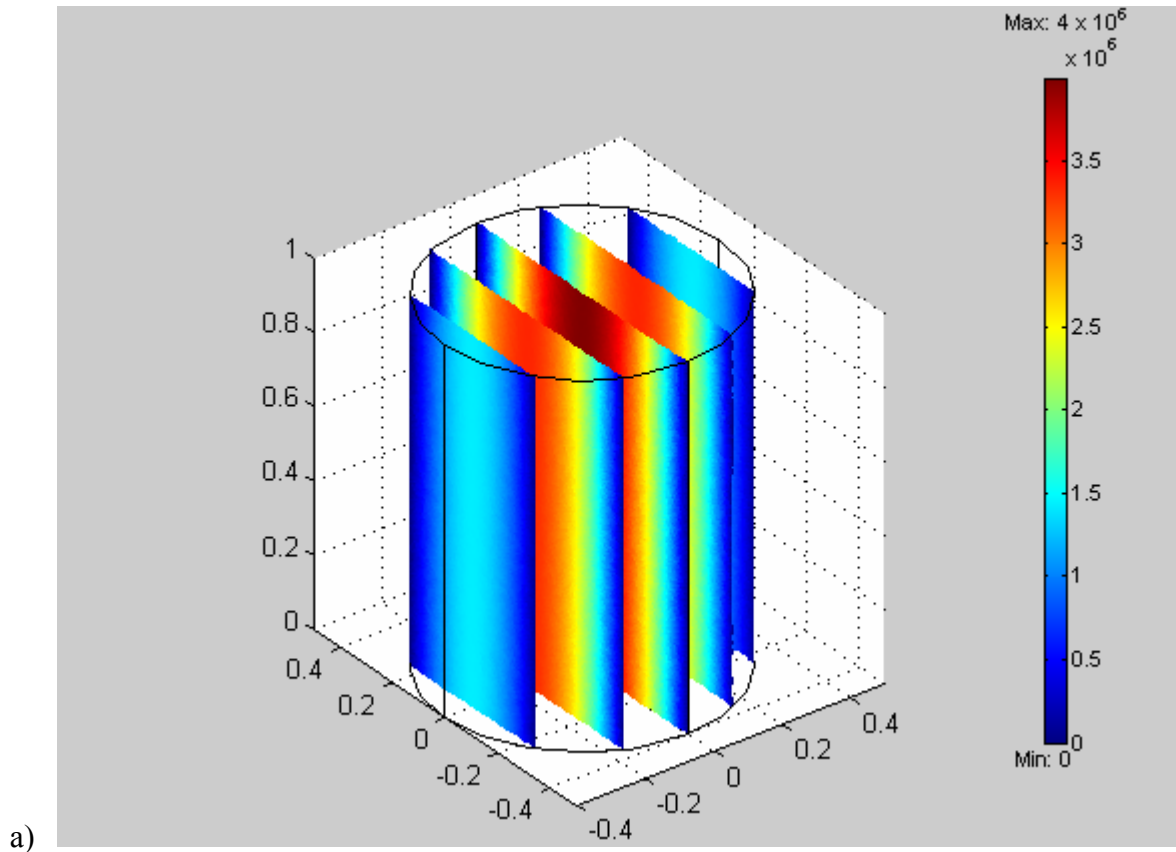


Figure 5.3. Pore throats are commonly depicted by circular cylinders. This shape is based upon the minimum cross-sectional area of the pore throat dimension as determined from the skeleton or medial axis image or in the case of mercury porosimetry from the pore entry diameter. The velocity profile is constant and parabolic (i.e., maximum flow rate at the center of the flow field and zero at the boundaries). Red depicts highest flow velocity and dark blue depicts “no-flow” conditions.

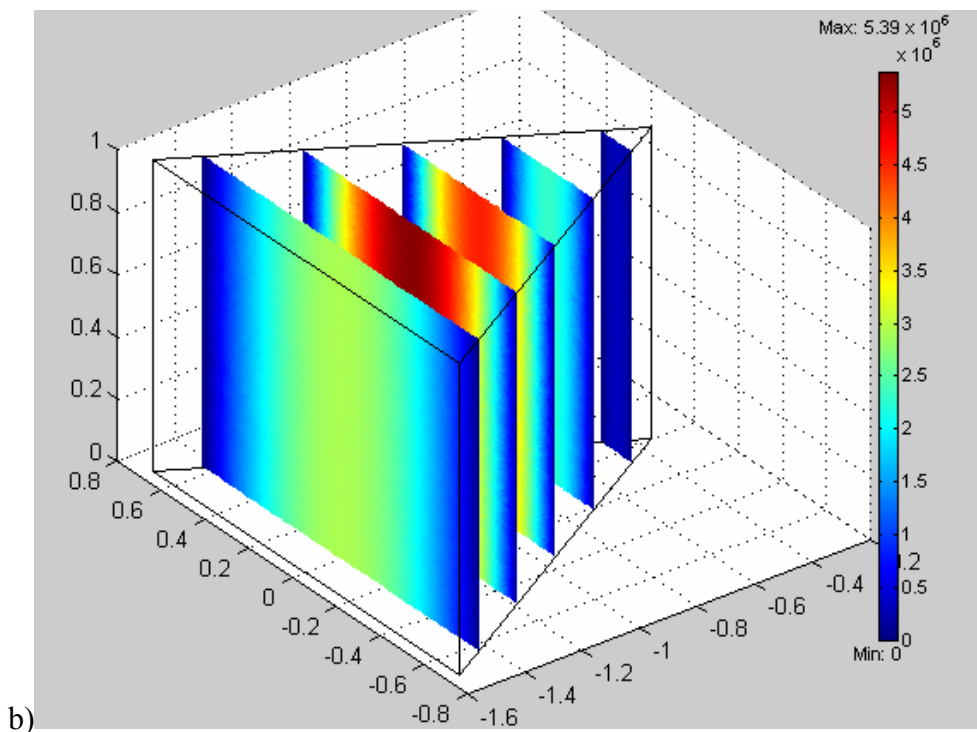
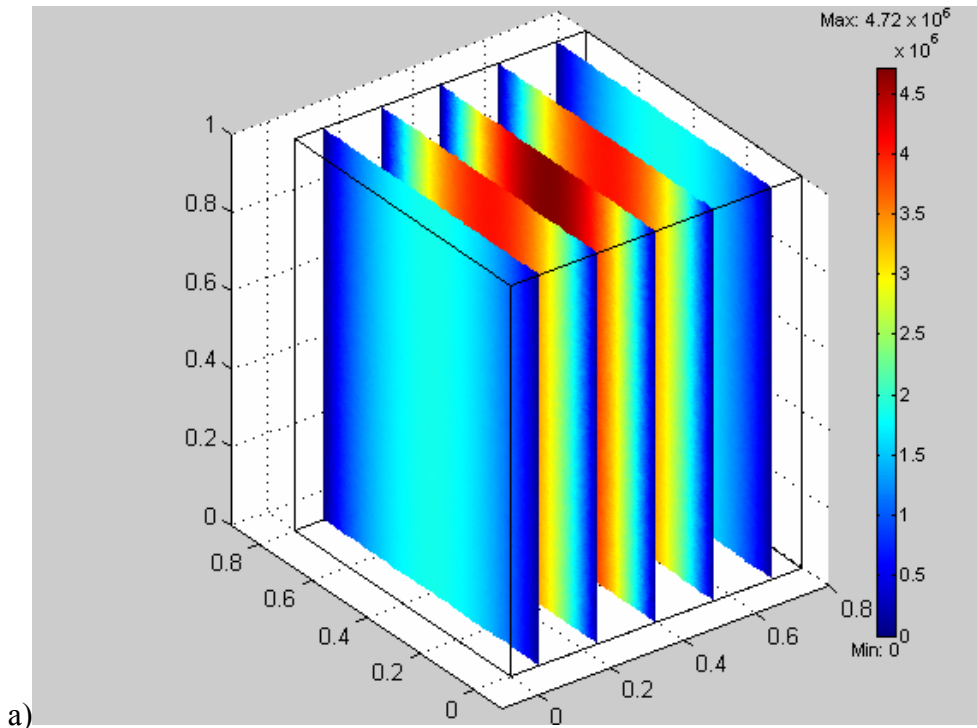


Figure 5.4. Pore throats are sometimes depicted by non-circular, but radially invariant shapes: (a) square and (b) triangular cylinders. These shapes have the same inscribed circle radius. The velocity profile is constant and parabolic (i.e., maximum flow rate at the center of the flow field and zero at the boundaries). Red depicts highest flow velocity and dark blue depicts “no-flow” conditions.

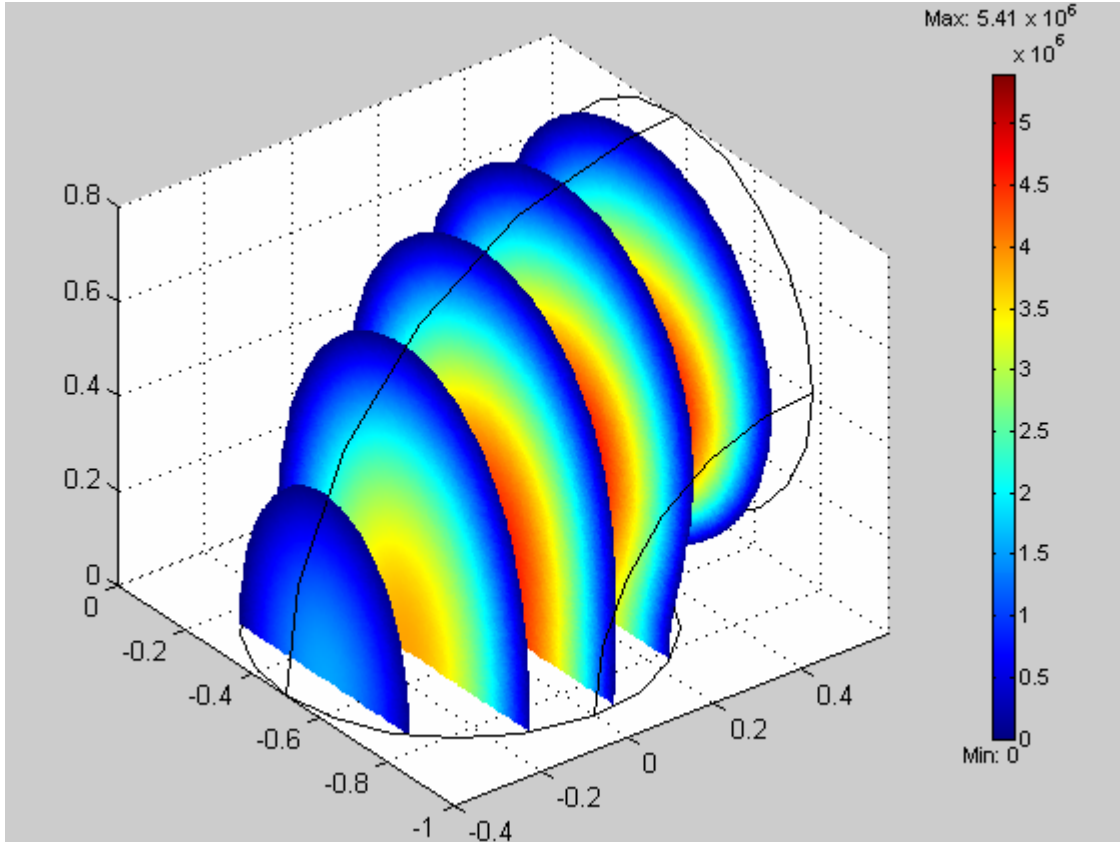


Figure 5.5. Pore throats are bent or curved in some cases and thus the flow direction is altered prior to reaching the adjacent pore body.

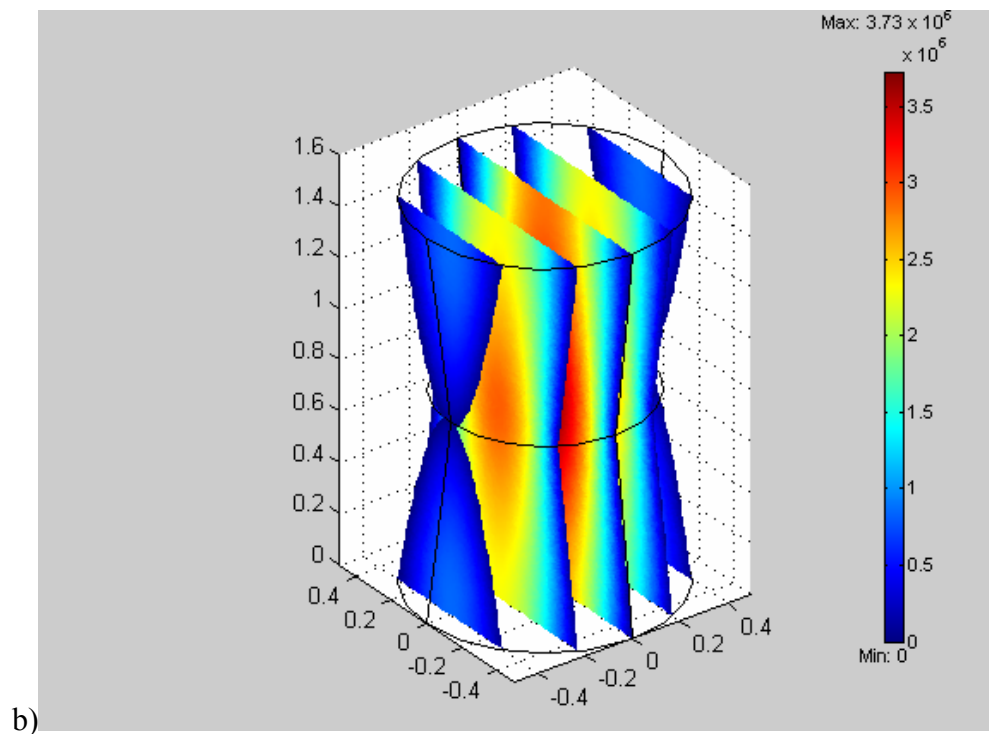
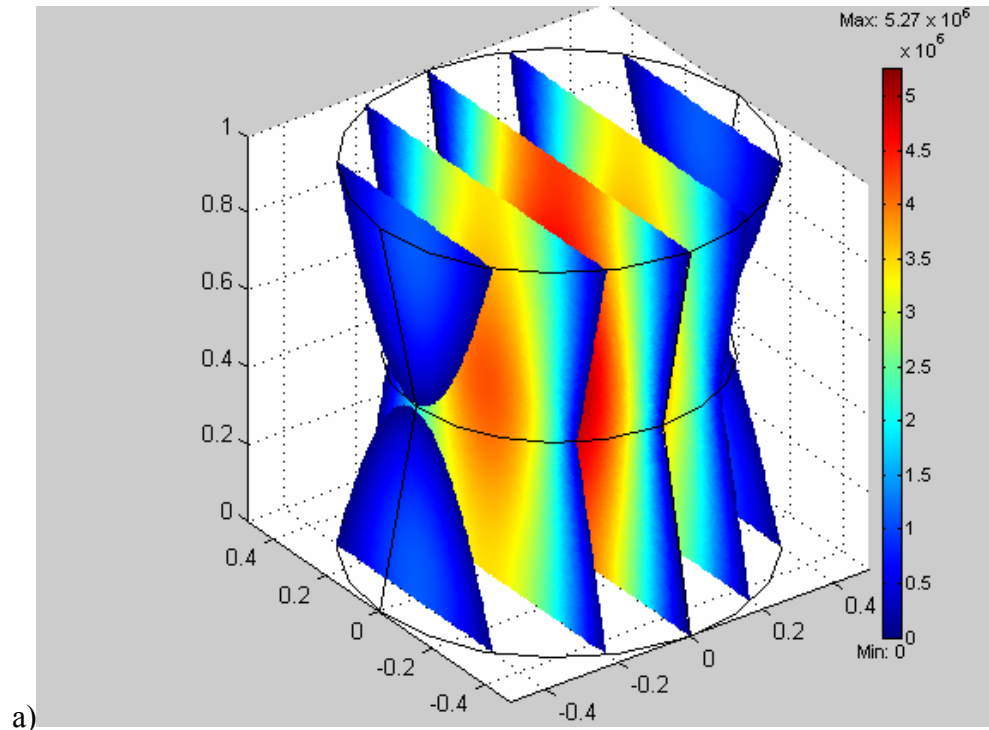
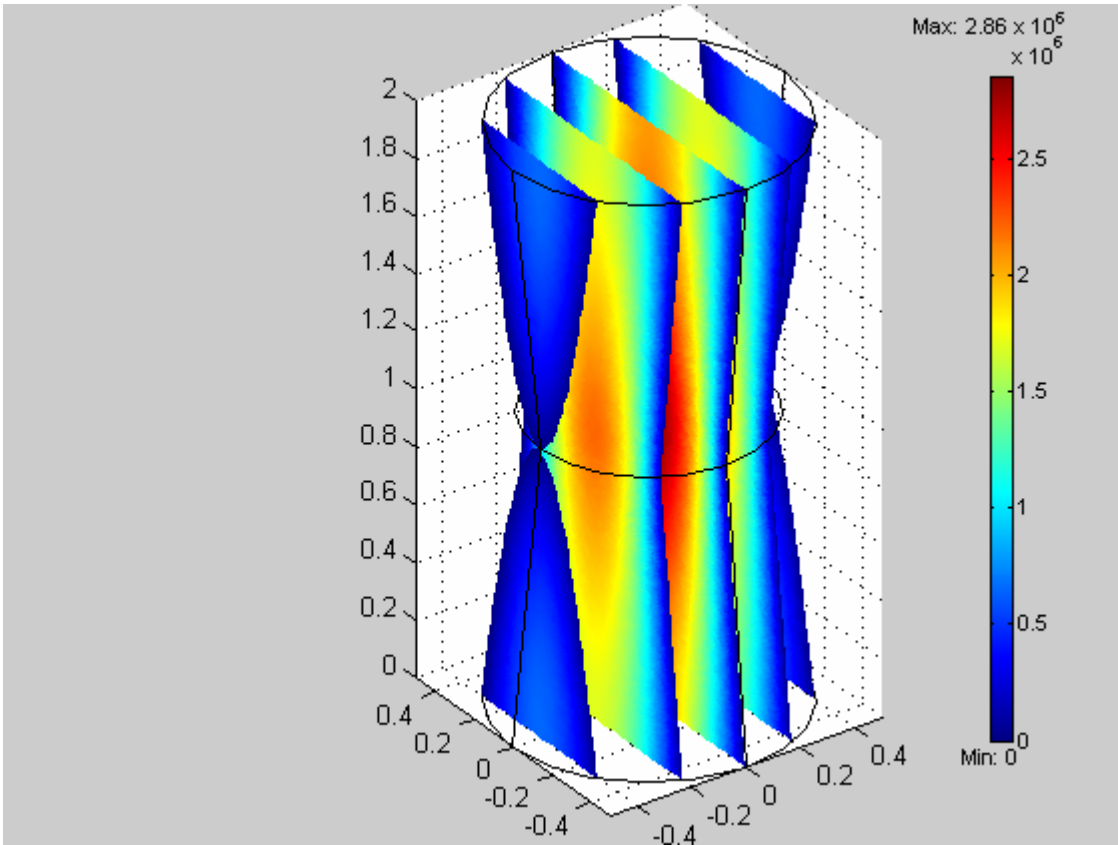


Figure 5.6. Pore throats are also be depicted by radially variant shapes, such as hourglass cylinders (a-c), to account for constriction along the throat length. Within these pore throats the parabolic velocity profile is orders of magnitude higher at the constriction than at the pore body-pore throat connection due to focusing. (figure continued on next page)



c)

2.89 (Fig. 5.5a), 2.35 (Fig. 5.5b), and 2.77 (Fig. 5.5c) times as fast as flow at the entry or exit of the same pore throat.

Pressure differences across a pore throat would likely range from 10^{-3} to 10^0 kPa (10 to 10^4 dynes/cm²). The volumetric fluid flow was linear for all pore throats and scaled with the pressure difference applied across the pore throat (Table 5.2) for pressures that ranged from 10^{-3} to 10^2 kPa (10 to 10^6 dynes/cm²). Flow in this system is linear, creeping flow for all shapes evaluated, as determined by linear increases in velocity with increases in differential pressure and Reynolds's numbers that are $O10^{-2}$, $O10^0$ for $dp = .01$ and 1 kPa, respectively (Table 5.2). However, the flow at higher pressures $O10^2$ kPa is probably linear, since these are straight walled pipes, but would be considered to be outside of the laminar flow regime for flow in porous media bounded by rough walls, diverging/converging pore boundaries, and directional changes.

The average flow rate with distance through the pore throat is shape dependent as evidenced by different velocities at different points in the cone shaped throats. This variability increases linearly in response to increases in pressure difference applied across the pore throat. The volumetric flow rates are relatively similar when the inscribed radius is relatively small (0.2); all shapes have a higher conductance than that of the circle as well as a higher volume to surface area. Flow rates in the circle and cone converge as the constriction factor for the cone approaches unity. The volumetric flow rate for the triangle and the square diverge from the other flow rates; the flow rate for the triangle is a factor of 2 higher than the flow rate for the circle and bent pore throats (Figure 5.5).

Similarly, the flow rates for cone_1 and the square pore throat are 1.5 times greater than

Table 5.2. Volumetric fluid flow for pore throats of commonly used and representative pore throat shapes was linear over a pressure range that spans that which would be expected for pore throats and laminar fluid flow (10^2 to 10^6 dynes/cm²)

dP (kPa) (kg m s⁻²)	circle	square	triangle	Bent	cone_1	cone_1.5	cone_2
Pore throats with a 20 micrometer minimum radius							
0.01	6.28E-14	8.99E-14	1.27E-13	6.26E-14	2.28E-13	1.71E-13	1.36E-13
1.00	6.28E-12	8.99E-12	1.27E-11	6.26E-12	2.28E-11	1.71E-11	1.36E-11
100	6.28E-10	8.99E-10	1.27E-09	6.26E-10	2.28E-09	1.71E-09	1.36E-09
Pore throats with a 30 micrometer minimum radius							
0.01	3.18E-13	4.55E-13	6.04E-13	3.18E-13	7.11E-13	5.02E-13	3.87E-13
1.00	3.18E-11	4.55E-11	6.04E-11	3.18E-11	7.11E-11	5.02E-11	3.87E-11
100	3.18E-09	4.55E-09	6.04E-09	3.18E-09	7.11E-09	5.02E-09	3.87E-09
Pore throats with a 40 micrometer minimum radius							
0.01	1.01E-12	1.44E-12	2.04E-12	1.00E-12	1.47E-12	1.02E-12	7.63E-13
1.00	1.01E-10	1.44E-10	2.04E-10	1.00E-10	1.47E-10	1.02E-10	7.63E-11
100	1.01E-08	1.44E-08	2.04E-08	1.00E-08	1.47E-08	1.02E-08	7.63E-09

the flow in the circle and bent pore throats. The flow rate of cone_1.5 is approximately equivalent to the flow rate for the circle and bent pore throats, while the flow rate of cone_2 is approximately three-fourths of the flow rate in the circle and bent pore throats.

The conductance ratio (circle/other shape) varies dramatically in some cases in which the conductance of the different shapes is always higher than that of the circle. The most obvious difference occurs for a cone that has an inscribed radius of 0.2, for which the conductance is 3.5 times that of the circle with the same radius. And the cone retains an elevated conductance above all the rest until the inscribed radius is 0.3, but becomes roughly equivalent to the conductance of the square at an inscribed radius of 0.4 and equal to the circle at an inscribed radius of 0.5. The conductance ratio is ~1.4 for the

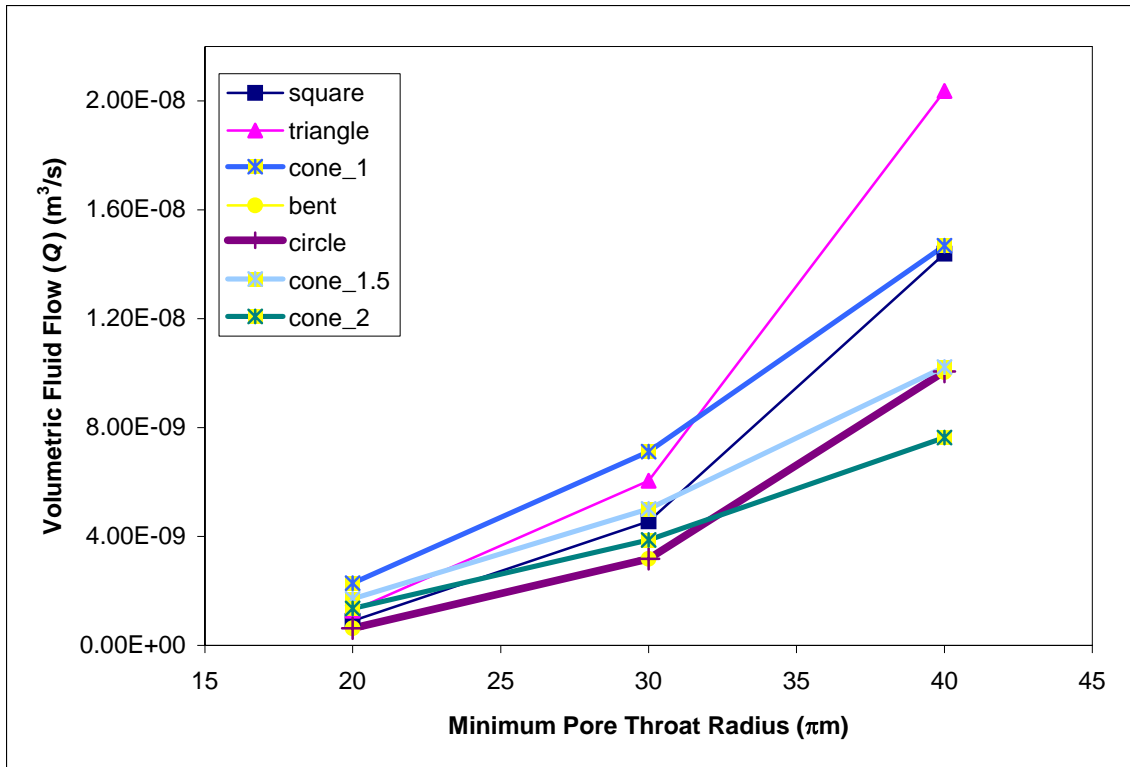


Figure 5.7. Volumetric flow rates for pore shapes with equivalent inscribed circular cylinder, but different cross-sectional shapes for pressure differences of 10^{-3} KPa. Relative relationships of Q to pore throat radius are constant between these shapes. The curve for the bent circular cylinder follows the same curve as the straight circular cylinder and is therefore hidden in this plot.

square ~ 2.0 for the triangle. The conductance ratio for the cones diminishes with increasing minimum inscribed ratio. The conductance ratio of the biconical shapes decreases with decreasing constriction factors and increasing minimum pore throat dimension. Conductance ratio of cone_1.0 diminishes from 3.75 to 2.3 to ~ 1.4 . The conductance ratio of cone_1.5 diminishes from 2.75 to 1.6 to 1.0. The conductance ratio of cone_2.0 diminishes from 2.0 to 1.4 to 0.75 (Figure 5.6).

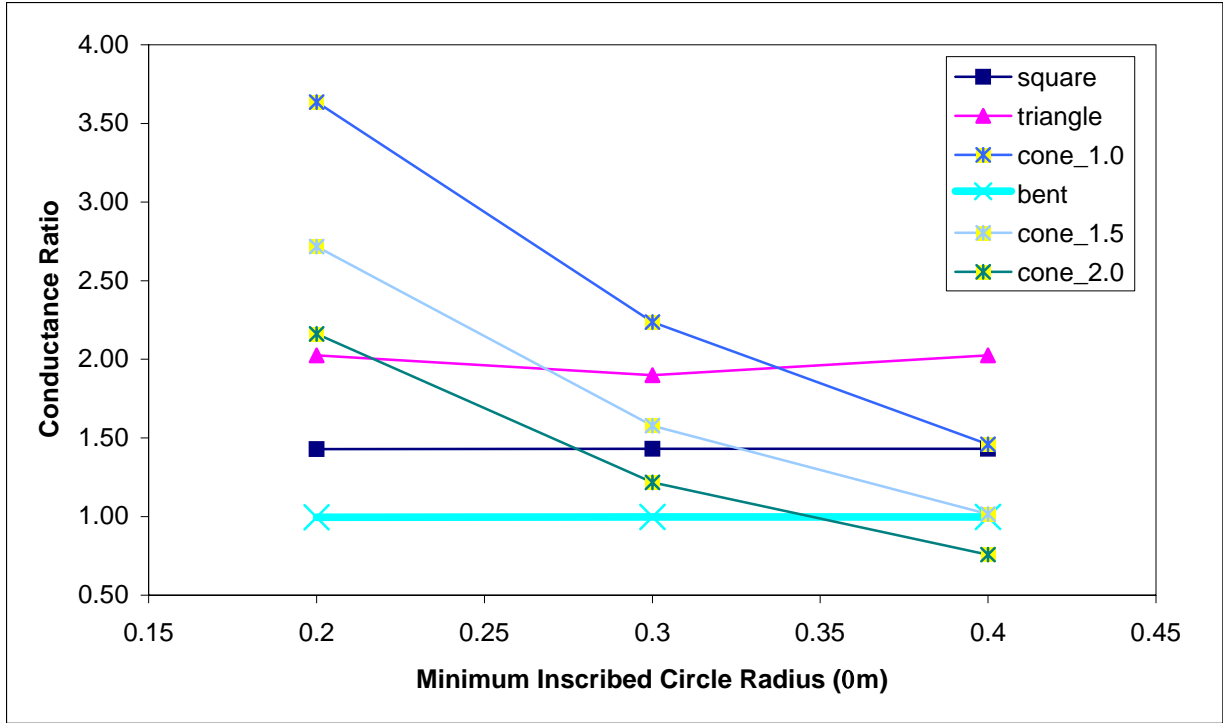


Figure 5.8. Conductance ratio for square, triangle, cone_1.0, cone_1.5, and cone_2.0, and bent circle pore throats to the conductance of the circle with the same radius. Circle, square, triangle, cone_1.0, and bent pore throats have a unit length of 1.0, cone_1.5 has a unit length of 1.5, and cone_2.0 has a unit length of 2.0.

5.4 Discussion

Pore geometry and topology of marine sand is dependent upon the grain boundaries, however, to recreate these boundaries is a complex problem that is not readily addressed from skeletonization and medial axis routines, which depict the sediment pore space as a one dimensional string of pixels/voxels. Therefore the degree to which pore throats can incorporate roughness into discrete pores is somewhat limited. This is apparent in these two sediment types, one of which has fairly smooth walls and the other has rough walls, which are mirrored by the surficial features of individual grains. It is probable that pore throat surfaces are angular at grain contacts as can be easily visualized in cross sections of pore throats bounded by cubic packings of spherical

particles (Thompson and Fogler, 1996; Sisivath et al., 2001; Man and Jing, 2001). The pore throats in natural porous media tend to be even more complex as indicated by cross-sections of Berea sandstone (Sisivath et al., 2001) or in Figures 5.1 and 5.2. Therefore, it is reasonable to evaluate pore throat and pore body dimensions that were determined using image analysis techniques used in this chapter (Table 5.1) and which were taken from over 4 thousand pore bodies and 6 thousand pore throats. These dimensions indicate reasonable bounds for development of a pore network model that represents marine sand and is comprised of pore throats and pore bodies. While these pore sizes were determined from 2D pore geometry dimensions, it is probable that these pore sizes are accurate for 3D porous media as well (see Chapter 4). The most important aspect of these pore sizes and ratios for marine sand, as determined quantitatively from the 2D images (Fig. 5.1) and qualitatively from the 3D images (Fig. 5.2) is that they provide realistic guidelines to bound pore sizes in network models, that they indicate a range of sizes and shapes, and that these data can be extracted from skeleton and medial axis image files.

Two-dimensional cross-sectional determinations of pore roughness and conductance provide a valuable future possibility for assessing conductance in variably shaped pore throats. This will be most valuable if the pore throat shape can be fabricated to a representative shape and still maintain accurate conductance predictions. The development of a boundary element method to construct pore throats with complex 2D polygonal cross-sections has been effective in representing pore throat complexity in 2D images (Sisivath et al., 2001) and adaptation of this technique to provide complex radially invariant pore throats to network models would be a valuable step to incorporate

more roughness to pore throat walls. This remains a future possibility. Currently conductance is based upon simple pore geometries that are commonly represented in network models. Conductance for shapes with an equivalent inscribed circle were determined to be highest for triangles, squares, and circles respectively and scaled with the cross-sectional area of those shapes. The area for the triangles was largest or 1.7 times that of the circles, and the area of the squares was 1.3 times that of the circles. The conductance determinations were accurate to within 2.8, 0.18, and 0.01 % for triangle, square, and circle pore throats, respectively. These values are quite reasonable for circle, somewhat reasonable for square and not unreasonable for triangle, which may have a larger error due to difficulties in drawing the initial shape in the CFD program. The CFD program limits drawings to specific minimum grid spacings, which may not be small enough to accurately depict the triangular shapes. Angles that are not equal to 90° may have inherent errors, because the triangle apexes were forced to a node on the grid, which was refined to a large extent, but not enough to overcome all possible errors in drawing the shape. This problem may be circumvented by creation of shapes from computer code rather than from the GUI (graphical user interface) and CFD based approach. This enabled both the cone shapes and the bent tubes to be drawn with relative ease and a line code would be the way in which the pore throat shapes would be constructed for application within pore network models. Conductance errors in the square and triangle might be removed by incorporating a meshing routine that is dedicated to corner angle refinement and is used in conjunction with the general meshing scheme (Patzek and Silin, 2000).

Pore throat shape plays an intricate and fundamental role of network models (e.g. imbibition and acoustic attenuation studies) and efforts to develop increasingly realistic pore scale network models are vital to the successful understanding of these processes. Typically pore throats are modeled with a bundle of tubes approach where pore throats are modeled as simple cylinders and many of the important geometrical aspects within actual pore throats are ignored. The primary improvement with these models is that the pores are now connected in series and parallel rather than disconnected. This pore throat shape has been widely accepted in part because porosimetry analysis provides an estimate of the minimum pore throat radius and the conductance of cylindrical pore throats is readily solved with the Hagen-Poiseuille equation (Eq. 5.1). The quest for more realism in pore structure and the incorporation of essential pore throat aspects, namely roughness and the capability of the models to allow multiphase flow, led to the development of models with corner angles (Patzek and Silin, 2001; Patzek and Kristensen, 2001; Dillard and Blunt, 2000). As with the cylindrical pore throats the conductance for these shapes is obtained easily and with little ambiguity (Bear, 1972; Sisivath et al., 2001; Patzek and Silin, 2001). The quest for more realism is still more complicated in that it requires testing and knowledge of how specific pore throats control conductance and what aspects of the pore throats are required to aid in accurate assessments of the pore scale process without arbitrary adjustments to pore throat radii to fit bulk conductance. Complexity in pore throat shapes has led to approximations by hourglass (Thompson and Fogler, 1996; Man and Jing, 2000) and biconical pore throats (Reeves and Celia, 1996) that incorporate a constriction typical of pore throats that have a minimum cross-sectional area near the midpoint of the path length. This study determined conductance numerically for shapes

for which empirical equations do not readily exist, such as hourglass shapes, from pore body sizes and the minimum cross-sectional areas that were determined from marine sands. With the flow bounded by these shapes it is then necessary to supply reasonable pressure differences across the pore throat, solve the fluid flow numerically, determine pore throat conductance between all pore bodies, and finally determine total conductance through the pore network system. Then it can be determined if permeability and conductance of the entire porous media fits with experimental data, make adjustments to the pore throat as necessary, and determine pore throat information that is requisite to making sound predictions of acoustic propagation, hydrodynamic dispersion, and multiphase fluid flow (2, 3, or more phases).

This variability is an important aspect of fluid flow, acoustic propagation, and hydrodynamic dispersion, which may all be strongly influenced by the fact that most pore throats have constriction factors that focus fluid flow, create variable flow velocities along the length of the pore throat, and potentially have zones where flow is stagnant (Koplik and Lasseter, 1982; Kitanidis and Dykaar, 1997). Quantifying the conductance for these shapes and determining how these shapes influence fluid flow provides an interesting challenge. A primary cause for acoustic attenuation is the out-of-phase movement between the pore water and the granular frame during an acoustic impulse. The direct impact of the pore shape on the out-of phase movement of sound through pore water and bounding grains is unclear, but it seems reasonable to suggest that the sound may be focused within constricted pores and then dispersed as was determined for electricity in electrical resistivity studies. The conductance for bent pore throats was determined to be the same as that of the circle pore throats, but the fact that the pore

throat redirects fluid may be significant. By analogy, the acoustic pulse that propagates through the sand may be scattered or focused in a different direction due to the shape of these pores. The significance of this potential would need to be examined further, but it may help to explain some of the divergence in modeled and measured results that occurs for attenuation at frequencies greater than 100 kHz (Williams et al., 2002). This constriction may accentuate the out-of-phase fluid movement, which oscillates within the pore space and leads to attenuation of the acoustic signal; it may also contribute to signal loss associated with squeeze-film motion or acoustic attenuation due to expansion/contraction of the granular frame in response to fluid movement that is acted upon by an acoustic signal while the fluid accelerates/decelerates through relatively constricted pore throats.

In each of these cases a network model that would incorporate an evaluation of pore throat shape variability during run time would be required. This would require longer run times, but these should not significantly increase the total run time and should enhance system understanding and prediction accuracy. An FEM solver could facilitate the use of variably shaped pores for which the conductance could be evaluated discretely and the influence of the pore throat shapes be determined more rigorously. Currently the best way to determine the influence of pore shape variability on these processes is to set up network models that uses pore throats that are represented by one or more of these pore throat shapes as dependent upon the salient and quantifiable aspects of the pore geometry and topology, determine the conductance of each pore throat, adjust the pore throat conductance as necessary to agree with the bulk conductance, and then solve

dispersion, multiphase flow, cementation, and acoustic attenuation problems within a well bounded pore structure.

5.5 Summary

Pore throat conductances were accurately determined for simple pore throat shapes for which an exact empirical equation for conductance exists by solving fluid flow rates numerically for a range of pressure gradients using a FEM. This provides confidence that the conductances of pore throats with constrictions would also be determined more accurately. Constricted pore throats, which are common in naturally occurring porous media are found to have variable pore-scale fluid flow, which may in and of itself influence acoustic attenuation, cementation, hydrodynamic dispersion, and electrical resistivity within naturally occurring porous media. These constrictions may also account for much of the acoustic attenuation at high frequency, whereas bent pore throats, or pore throats that veer off from the incident angle of the acoustic pulse, may account for significant redirection (or scattering) and attenuation of sound. The conductance of a bent tube was the same as that of the circle pore throat, however the importance of a bent pore throat can not be overlooked as it would serve to redirect the fluid flow and acoustic pulse and should be incorporated with this in mind and for the fact that it would redirect the fluid or increase the total travel time with respect to a straight line path through the media.

This method will provide increased realism to network model development that is based on increasingly common 1-dimensional depictions of pore space, facilitate the incorporation of realism into network models, and provide a sufficiently easy method to test predictions of acoustic propagation, hydrodynamic dispersion, and relative

permeability that it should be incorporated into pore scale modeling approaches. If this does occur then pore scale modeling will provide increasingly significant and important contributions to the determination of influences by pore geometry on acoustic attenuation, hydrodynamic dispersion, grain cementation, and oil recovery.

CHAPTER 6: SUMMARY AND CONCLUSIONS

Pore geometry of marine sand can be broken down into component and mathematically quantifiable components, which can be used in the assessment and prediction of sediment physical properties and pore throat conductance. This will yield well bounded and improved pore scale network models. These improvements will then aid in increasingly realistic and accurate simulations of pore scale processes, which will facilitate understanding of acoustic propagation, contaminant mitigation, ground water protection, aquifer maintenance, and hydrocarbon extraction.

This study demonstrates the complexity of homogeneous systems at or about the REV scale and displays the utility of using image analysis and EMT modeling to predict sediment physical properties at scales that are unobtainable by traditional measurements. Thus, an effective method for acquiring data that is relevant to high-frequency (100-1000 kHz) acoustic models is presented.

At the culmination of the EMT/permeability prediction study (Chapter 3) it was unclear whether 2D and 3D pore geometry and topology were the same or different. Therefore, comparisons of pore geometry from 2D and 3D images of same sample, at the same resolution, and over the same interval demonstrated that there was a high degree of similarity in 2D and 3D pore geometry. It was also demonstrated that 2D and 3D topology is more similar than traditionally assumed. That is, this study demonstrates that coordination numbers determined from 2D images ($z = 3$) are closer to coordination numbers determined from 3D images ($z = 3.9$) than the coordination number ($z = 6$) commonly used in network models. These two findings indicate that 2D images of homogeneous and isotropic marine sand represent pore scale heterogeneity of 3D images.

This was true for 2D images that have edge lengths of approximately 8 grain diameters (~3 mm). This finding probably cannot be extended to heterogeneous materials, such as fractured rock, layered rock, or clay or platy sediment systems.

Pore throats in the preceding findings and in the majority of pore network models are manifested as circular cylinders, which are radially invariant. However, in 2D and 3D images, pore throats have variable cross-sectional radii. Therefore, the circular cylinders may be too simplified to be valuable to models of acoustic and fluid flow processes, which are influenced by irregularities in sediment geometry. To evaluate the influence of different shapes on fluid flow and conductance, pore throat conductance was determined for representative pore throat shapes, which were constructed from pore geometry data (i.e., pore body and pore throat radii). Conductance for radially invariant pore throats (e.g. circular, square, and triangular cylinders with the same inscribed circle radii) differed by factors of 1.5 and 2. This difference was proportional to the difference in cross-sectional area. In the case of biconical tubes, conductance differed by more than 3.5 (i.e., for the largest constriction factors). This significant difference may be incorporated into network models to adjust or fit the sample to bulk conductance.

If the bulk conductance is increased by incorporating more realistic pore throat geometries, while reducing the number of pathways for fluid flow, by incorporating more realistic coordination numbers, then a balance between increased realism and model accuracy may be obtained. The increased realism in terms of representative pore throats and realistic coordination numbers ought to yield more realistic depictions of acoustic propagation and dispersion, contaminant mitigation, and relative permeability of oil.

REFERENCES

- Al-Raoush, R., Extraction of Physically-Realistic Pore-Network Properties from Three-Dimensional Synchrotron Microtomography Images of Unconsolidated Porous Media, Ph.D. dissertation, Louisiana State University, Baton Rouge, LA, 173 pp., 2002
- Al-Raoush, R., K. E. Thompson, and C. S. Willson, Comparison of network generation techniques for unconsolidated porous media systems, *Soil Sci. Am. J.*, in press.
- Anselmetti, F. S., S. Luthi and G. P. Eberli, Quantitative characterization of carbonate pore systems by digital image analysis, *AAPG Bulletin*, 82, 1815-1836, 1998.
- ASTM Committee D-18, ASTM D 4253-83: Standard test methods for the maximum index density of soils using a vibratory table, *Annual Book of ASTM Standards*, 18, 589-600, 1983.
- Bathurst, R. G, Marine diagenesis of shallow-water calcium-carbonate sediments, *Ann. Rev. of Earth and Planetary Sciences*, 2, 257-274, 1974.
- Bear, J., *Dynamics of Fluids in Porous Media*, Dover Publishing Co., New York, 1972.
- Bell, J.W., 1981, Subsidence in Las Vegas Valley, *Nevada Bureau of Mines and Geology Bulletin*, 95, 84 p.
- Bell, J.W., Price, J.G., and Mifflin, M.D., Subsidence-induced fissuring along preexisting faults in Las Vegas Valley, Nevada: Proceedings, Association of Engineering Geologists, 35th Annual Meeting, Los Angeles, 1992.
- Bennett, R. H., K. M. Fischer, D. L. Lavoie, W. R. Bryant, and R. Rezak, "Porometry and fabric of marine clay and carbonate sediments: Determinants of permeability," *Mar. Geotechnol.*, 89, 127-152, 1989.
- Bennett, R. H., M. H. Hulbert, C. Curry, H. P. Johnson, M. Hutnak, and K. Curry, *In situ* permeameter probe for coastal marine sediments, *IEEE J. Oceanic Eng.*, 27, 362-375, 2002.
- Berryman, J. G., and S. C. Blair, Kozeny-Carman relations and image processing methods for estimating Darcy's constant, *J. Applied Phys.*, 62, 2221-2228, 1987.
- Biot, M. A., Theory of propagation of elastic waves in a fluid saturated porous solid. II. Higher frequency range, *J. Acoust. Soc. Amer.*, 28, 179-189, 1956.
- Biot, M. A., Generalized theory of acoustic propagation in porous dissipative media, *J. Acoust. Soc. Amer.*, 34, 1254-1264, 1962.

- Blunt, M. and P. King, Relative permeabilities from two- and three-dimensional pore-scale network models, *Transport in Porous Media*, 6, 407-433, 1991.
- Blunt, M., Flow in Porous Media --- Pore-Network Models and Multiphase Flow, Current Opinion in Colloid and Interface Science, 6, 197-2007, 2001.
- Bourbie, T., O. Coussy, and B. Zinszner, *Acoustics of Porous Media*, Gulf Publishing Co., Houston, TX, pp. 40-42.
- Brown, W. E., and H. W. Patnode, Plastic lithification of sands *in situ*, *Bull. Amer. Assoc. Petrol. Geol.*, 37, 152-162, 1951.
- Briggs, K. B., High-frequency acoustic scattering from sediment interface roughness and volume inhomogeneities, Ph.D. dissertation, Univ. of Miami, Coral Gables, FL, 1994.
- Briggs, K. B., unpublished data, 2002.
- Bryant, S., and M. Blunt, Predictions of relative permeability in simple porous media, *Phys. Rev. A*, 46, 2004-2011, 1992.
- Bryant, S., P. King and D. Mellor, Network model evaluation of permeability and spatial correlation in a real random sphere packing, *Transp. Por. Media*, 11, 53-70, 1993.
- Carman, P. C., Flow of Gases in Porous Media, Academic Press, NY., 182 pp.
- Celia, M.A., P.C. Reeves, and L.A. Ferrand, Pore-scale Models for Multiphase Flow in Porous Media, *Reviews of Geophysics, Supplement*, 1049-1057, 1995.
- Clark and Kleinberg, Physics in oil exploration, *Physics Today*, 55, 48-53, 2002.
- Clausnitzer, V., and J. W. Hopmans, Determination of phase-flow fractions from tomographic measurements in two-phase systems, *Advances in Water Resources*, 22, 577-584, 1999.
- Clennell, M. B., Tortuosity: a guide through the maze, in M.A. Lovell and P. K. Harvey, *Developments in Petrophysics, Geological Society Special Publication No. 122*, pp. 299-344. *Machine Intell.*, 10, 919-927, 1988.
- Corso, P. S., M. H. Kramer, K. A. Blair, D. G. Addiss, J. P. Davis, A. L. Haddix, Cost of illness in the 1993 waterborne *Cryptosporidium* outbreak, Milwaukee, Wisconsin, *Emerging Infectious Diseases*, 9, 426-431, 2003.
- David, C., Y. Gueguen, and G. Pampoukis, Effective medium theory and network theory applied to transport properties of rock, *J. Geophys. Res.*, 95(B5), 6993-7005, 1990.

- David, C., Geometry of flow paths for fluid transport in rocks, *J. Geophys. Res.*, 98 B7, 12267-12278, 1993.
- De Arcanagelis, L., J. Koplik, S. Redner, D. Wilkinson, Hydrodynamic dispersion in network models of porous-media, *Phys. Rev. Lett.*, 57, 996-999, 1986.
- Dillard, L. A. and M. J. Blunt, Development of a pore network simulation model to study nonaqueous phase liquid dissolution, *Water Resour. Res.*, 36, 439-454, 2000.
- Doyen, P. M., Permeability, conductivity, and pore geometry of sandstone, *J. Geophys. Res.*, 93(B7), 7729-7740, 1988.
- Doyle, L. J., and T. N. Sparks, Sediments of the Mississippi, Alabama and Florida (MAFLA) continental shelf, *J. Sediment. Petrol.*, 50, 905-915, 1980.
- Drake, T. G., Structural features in granular flows, *J. Geophys. Res.*, 95(B6), 8681-8696, 1990.
- Dullien, F. A. L., New network permeability model of porous media, *J. AIChE*, 21, 299-307, 1975.
- Dullien, F. A. L., Characterization of porous media-pore level, *Transp. Por. Media*, 6, 581-606, 1991.
- Dullien, F. A. L., *Porous Media: Fluid Transport and Pore Structure*, Academic Press, Boston, 1992.
- Ehrlich, R., S. Kennedy, S. J. Crabtree, and R. L. Cannon, Petrographic image analysis I. Analysis of reservoir pore complexes, *J. Sediment. Petrol.*, 54, 1365-1378, 1984.
- Ehrlich, R., S.J. Crabtree, K. O. Horkowitz, and J. P. Horkowitz "Petrography and reservoir physics I: objective classification of reservoir porosity," *J. Sediment. Petrol.*, 75, 1547-1562, 1991.
- Ehrlich, R., E. L. Etris, D. Brumfield, L. P. Yuan, and S.J. Crabtree, "Petrography and reservoir physics III: Physical models for permeability and formation factor," *Amer. Assoc. Pet. Geol. Bull.*, 75, 1579-1592, 1991.
- Fatt, I., The network model of porous media I. Dynamic properties of networks with tube radius distribution, *Pet. Trans. AIME*, 207, 144-159, 1956.
- Fenwick, D. H., and M. J. Blunt, Network Modeling of Three-Phase Flow in Porous Media, *SPE J.*, 3, 86-97, 1998a.

- Fenwick, D. H., and M. J. Blunt, Three-dimensional modeling of three phase imbibition and drainage, *Adv. Water Resour.*, 21, 121-143, 1998b.
- Fetter, C. W., *Applied Hydrogeology*, Simon and Schuster, New York, 1994.
- Finney, J. L., Random packings and the structure of simple liquids I. The geometry of random close packing, *Proc. Roy. Soc. Lond. A.*, 319, 479-493, 1970.
- Folk, R. L., *Petrology of Sedimentary Rocks*, Austin, Texas: Hemphills, 1965.
- Frazer, H. J., Experimental study of porosity and permeability of clastic sediments, *J. Geol.*, 43, 910-1010, 1935.
- Gaither, A., A study of porosity and grain relationships in experimental sands, *J. Sediment. Petrol.*, 23, 108-195, 1953.
- Hidajat, I., A. Rastogi, M. Singh, K. K. Mohanty, Transport properties of porous media from thin-sections, *SPE 69623*.
- Hilpert, M, and C. T. Miller, Pore-morphology-based simulation of drainage in totally wetting porous media, *Adv. Water Resour.*, 24, 243-255, 2001.
- Hilpert, M., R. Glantz, and C.T. Miller, Calibration of a pore-network model by a pore-morphological analysis, *Transport in Porous Media*. 51 (3): 267-285, 2003.
- Hounsfield, G. N., Computerized transverse axial scanning (tomography): I. Description of system, *British J. Radiology*, 46:1016-1022, 1973.
- Hui, M., and M. J. Blunt, Effects of wettability on three-phase flow in porous media, *J. of Phys. Chem. B*, 104, 3833-3845, 2000.
- Hyne, N.J., and H. G. Goodell, Origin of the sediments and submarine geomorphology of the inner continental shelf off Choctawhatchee Bay, Florida, *Mar. Geol.*, 5, 299-313, 1967.
- Jackson, P. D., D. Taylor Smith, and P. N. Stanford, Resistivity-porosity-particle shape relationships for marine sands, *Geophysics*, 43, 1250-1268, 1978.
- Jackson, P. D., K. B. Briggs, R. C. Flint, R. J. Holyer, and J. C. Sandidge, Two- and three-dimensional heterogeneity in carbonate sediments using resistivity imaging, *Mar. Geol.*, 182, 55-76, 2001.
- Jerauld G. R. and S. J. Salter, The effect of pore-structure on hysteresis in relative permeability and capillary pressure: pore level modeling, *Transp. Por. Media*, 5, 103-151, 1990.

- Kirkpatrick, S., Percolation and conduction, *Rev. Mod. Phys.*, 45, 574-588, 1973.
- Kitanidis, P. K., and B. P. Dykaar, Stokes Flow in a Slowly Varying Two-Dimensional Periodic Pore, *Transport in Porous Media*, 26, 86-98, 1997.
- Koplik, J., Creeping flow in two-dimensional networks, *J. Fluid Mech.*, 119, 219-247, 1982.
- Koplik, J., C. Lin, and M. Vermette, Conductivity and permeability from microgeometry, *J. Appl. Phys.*, 56, 3127-3131, 1984.
- Krinsley, D. H., and J. C. Doornkamp, *Atlas of Quartz Sand Surface Textures*, Cambridge: University Printing House, 1973.
- Lambe, T. W., *Soil Testing for Engineers*, New York: John Wiley and Sons, 1951.
- Liang, Z., M.A. Ioannidis, and I. Chatzis, Geometric and topological analysis of three-dimensional porous media: pore space partitioning based on morphological skeletonization, *J. Colloid Interf. Sci.*, 221, 13-34, 2000.
- Lindquist, W. B., *3DMA General Users Manual, Report No. SUSB-AMS-99-20*, Dept. Appl. Math. & Stat., SUNY-Stony Brook, 1996.
- Lindquist, W. B., S. M. Lee, D. A., Coker, K. W. Jones, and P. Spanne, Medial axis analysis of void structure in three-dimensional tomographic images of porous media, *J. Geophys. Res.* 101(B4), 82979-8310, 1996.
- Lindquist, W. B., Venkatarangan, Investigating 3D geometry of porous media from high resolution images, *Phys. Chem. Earth Pt. A* 24, 593-599, 1999.
- Lindquist, W. B., A. Venkatarangan, J. Dunsmuir, and T. Wong, Pore and throat size distributions measured from synchrotron X-ray tomographic images of Fountainebleau sandstones, *J. Geophys. Res.* 105(B9), 21509-21527, 2000.
- Lock, P. A., X. Jing, R. W. Zimmerman, and E. M. Schleuter, Predicting the permeability of sandstone from image analysis of pore structure, *J. Applied Phys.* 92, 6311-6319, 2002.
- Locker, S. D., and L. J. Doyle, Neogene to Recent stratigraphy and depositional regimes of the northwest Florida inner continental shelf, *Mar. Geol.*, 104, 123-138, 1992.
- Mair, R. W., G. P. Wang, D. Hoffman, M. D. Hurlimann, S. Patz, L. M. Schwartz, and R. L. Walsworth, Probing porous media with gas diffusion NMR, *Phys. Rev. Lett.*, 83, 3324-3327, 1999.

- Man, H. N., and X. D. Jing, Network Modeling of Strong and Intermediate Wettability on Electrical Resistivity and Capillary Pressure, *Adv. in Water Resources*, 24, 345-363, 2001.
- McBride, J.F., C.S. Simmons, and J.W. Cary, Interfacial spreading effects on one-dimensional organic liquid imbibition in water-wetted porous media, *J. Contaminant Hydrol.*, 11, 1-25, 1992.
- McMullen, R. M., and J. R. L. Allen, Preservation of sedimentary structures in wet unconsolidated sands using polyester casting resins, *Mar. Geol.*, 1, 88-97, 1964.
- Mohanty, The near-term energy challenge, *AIChE J.* 49, 2454-2460, 2003.
- Oh, W., and W. B. Lindquist, Image thresholding by indicator kriging, *IEEE Trans. Pattern Anal. Machine Intell.*, 21, 919-927, 1999.
- Oren, P.E., J. Billiotte, and W.V. Pinczewski, Mobilization of waterflood residual oil by gas injection for water-wet conditions, *Soc. Petr. Eng. Formation Evaluation*, 70-78, 1992.
- Pan, C., M. Hilper and C. T. Miller, Pore-scale modeling of saturated permeabilities in random sphere packings, *Phys. Rev. E.*, 64, 66702:1-9, 2001.
- Patzek, T. W., and D. B. Silin, Shape Factor and Hydraulic Conductance in Noncircular Capillaries—I. One-Phase Creeping Flow, *J. of Colloid and Interface Science*, 236, 295-304, 2001.
- Patzek, T. W., and J. G. Kristensen, Shape Factor and Hydraulic Conductance in Noncircular Capillaries—II. Two-Phase Creeping Flow, *J. of Colloid and Interface Science*, 236, 305-317, 2001.
- Plona, T. J., and D. L. Johnson, Acoustic properties of porous systems: I Phenomenological description, in *Physics and Chemistry of Porous Media*, ed. D. L. Johnson and P. N. Sen, American Institute of Physics NY, 89-104, 1984.
- Poland and Davis, 1967 Las Vegas
- Porter, Naval Mine Warfare: Operational and Technical Challenges for Naval Forces, N Nat. Academic Press, 132 pp., 2001.
- Powers, M. C., A new roundness scale for sedimentary particles, *J. Sediment. Petrol.*, 23, 117-119, 1953.
- Reed, A. H., K. B. Briggs, D. L. Lavoie, Porometric properties of a siliciclastic marine sand: A comparison of traditional laboratory measurements with image analysis and effective medium theory modeling, *IEEE J. Oceanic Eng.*, 27, 581-592, 2002.

- Reed, A. H., R. B. Pandey, and D. L. Lavoie, Fractal dimensionality of pore and grain volume of a siliciclastic marine sand, *Inter. J. Mod. Phys. C*, 11, 1555-1559, 2000.
- Reeves, P. C., and M. A. Celia, A functional relationship between capillary pressure, saturation, and interfacial area as revealed by a pore-scale network model, *Water Resources Research*, 32(8), 2345-2358, 1996.
- Richardson, M. D., K. B. Briggs, D. L. Bibee, P. A. Jumars, W. B. Sawyer, D. B. Albert, R. H. Bennett, T. K. Berger, M. J. Buckingham, N. P. Chotiros, P. H. Dahl, N. T. Dewitt, P. Fleischer, R. Flood, C. F. Greenlaw, D. V. Holliday, M. H. Hulbert, M. P. Hutnak, P. D. Jackson, J. S. Jaffe, H. P. Johnson, D. L. Lavoie, A. P. Lyons, C. S. Martens, D. E. McGhee, K. D. Moore, T. H. Orsi, J. N. Piper, R. I. Ray, A. H. Reed, R. F. L. Self, J. L. Schmidt, S. G. Schock, F. Simonet, R. D. Stoll, D. Tang, D. E. Thistle, E. I. Thorsos, D. J. Walter, and R. A. Wheatcroft, "An overview of SAX99: Environmental considerations," *IEEE J. Oceanic Eng.*, 26, 26-53, 2001a.
- Richardson, M. D., K. B. Briggs, S. J. Bentley, D. J. Walter and T. H. Orsi, Biological and hydrodynamic effects on physical and acoustic properties of sediments off the Eel River, California, *Mar. Geol.*, 182, 121-139, 2001b.
- Rivers, M.L., S. Sutton, and P. Eng, Geoscience applications of x-ray computed microtomography, Proceedings of SPIE, Developments in X-Ray Tomography II, 3772, 78-86, 1999.
- Russ, C., The Image Processing Toolkit 3.0, Reindeer Games Inc. 1990.
- Scheidegger, A. E., *The Physics of Flow Through Porous Media*, New York: MacMillan, 1960.
- Schiffes, S., War in Iraq and the Economy, BBC News 8 November, 2002.
- Schroeder, J. H., and K. Jacob, *In situ* impregnation of cores and profiles in coastal sediments, *Senckenberg. marit.*, 8, 81-89, 1976.
- Shepherd, R. G., Correlations of permeability and grain size, *Ground Water*, 5, 633-638, 1989.
- Sisivath, S, X. Jing, and R. W. Zimmerman, Laminar Flow Through Irregularly-Shaped Pores in Sedimentary Rocks, *Transport in Porous Media*, 45, 41-62, 2001.
- Soll, W.E. and M.A. Celia, A modified percolation approach to simulating three-fluid capillary pressure---saturation relationships, *Adv. Water Resour.*, 16, 107-126, 1993.
- Soll, W.E., M.A. Celia, and J.L. Wilson, Micromodel studies of three-fluid porous media

- systems: pore-scale processes relating to capillary pressure---saturation relationships, *Water Resour. Res.*, 29(9), 2963-2974, 1993.
- Stoll, R. D., Sediment Acoustics, in *Lecture Notes in Earth Sciences*, S. Bhattacharji, G. M. Friedman, H. J. Neugebauer, and A. Seilacher, Eds. New York: Springer-Verlag, 1989.
- Tang, D., K. B. Briggs, K. L. Williams, D. Jackson, E. I. Thorsos and D. B. Percival, Fine-scale volume heterogeneity measurements in sand, *IEEE J. Oceanic Eng.*, 27, 2002.
- Thompson, K. E., and H. S. Fogler, Modeling Flow in Disordered Packed Beds from Pore-Scale Fluid Mechanics, *AIChE J.*, 43, 1377-1389, 1996.
- Thorsos, E. I., K. L. Williams, N. P. Chotiros, J. T. Christoff, K. W. Commander, C. F. Greenlaw, D. V. Holliday, D. R. Jackson, J. L. Lopes, D. E. McGhee, M. D. Richardson, J. Piper, and D. Tang, An overview of SAX99: Acoustic measurements, *IEEE J. Oceanic Eng.*, 26, 4-25, 2001.
- Van Geet, M, R. Swennen, and M. Wevers, Towards 3-D petrography: Application of microfocus computer tomography in geological science, *Comput. Geosci.*, 27, 1091-1099, 2001.
- Wellington, S. L., and H. J. Vinegar, X-ray Computerized Tomography, *J. Petroleum Technology*, 885-897, 1987.
- Wevers, M., P. De Meester, R. Swennen, Microfocus X-ray computer tomography in materials research, *Insight, J. Brit. Inst. Non-Destruct.Test.*, 43 (10), 658-663, 2001.
- Wheatcroft, R. A., *In situ* measurements of near-surface porosity in shallow marine sands, *IEEE J. Oceanic Eng.*, this issue.
- White, J. V., B. L. Kirkland, and J. P. Gournay, Quantitative porosity determination of thin sections using digitized images, *J. Sediment. Res.*, 68, 220-222, 1998.
- Wilcox, D. C., B. S. Dove, W. D. McDavid, and D. D. Greer, *UTHSCA Image Tool 2.0*, University of Texas Health and Science Center, San Antonio, TX, 1989.
- Williams, K. L., D. R. Jackson, E. I. Thorsos, D. Tang, and K. B. Briggs, Acoustic backscatter experiments in a well characterized sand sediment: Data/model comparison using sediment fluid and Biot models, *IEEE J. Oceanic Eng.*, 27, 362-375, 2002.
- Williams, K. L., D. R. Jackson, E. I. Thorsos and D. Tang, Comparison of sound speed and attenuation measured in a sandy sediment to predictions based on the Biot theory of porous media, *IEEE J. Oceanic Eng.*, 27, 2002.

Wilkinson, B. H., and E. Landing, Eggshell diagenesis and primary radial fabric in calcite ooids, *J. Sed. Pet.*, 48,1129-1137, 1978.

Yamamoto, T. and A. Turgut, Acoustic-wave propagation through porous-media with arbitrary pore-size distributions, *J. Am. Soc. Acoust.*, 83, 1744-1751, 1988.

APPENDIX: COPYRIGHT PERMISSION

Comments/Response to Case ID: 006C9C94

ReplyTo: Pubs-Permissions@ieee.org

From: Jacqueline Hansson

Date: 09/08/2003

Subject: Re: RE: Using IEEE-OE paper in
<areed@earthquake.nrlssc.navy.mil>
dissertation

Send To: "Reed, Allen"

cc:

SUBJECT: " Porometric properties of siliciclastic marine sand: a comparison of traditional laboratory measurements with image analysis and effective medium modeling", IEEE J.Oceanic Eng., IEEE J. Oceanic Eng., vol. 27, pp. 581-592, 2002.

Dear Mr. Reed:

This is in response to your letter of 5 September 2003 in which you have requested permission to reprint, in your upcoming dissertation, the above IEEE copyrighted material. We are happy to grant this permission.

Our only requirement is that the following copyright/credit notice appears prominently on the first page of each reprinted paper, with the appropriate details filled in:

© 2002 IEEE. Reprinted, with permission, from (complete publication information).

Sincerely yours,

Jacqueline Hansson
IEEE Intellectual Property

IEEE Intellectual Property Rights Office
445 Hoes Lane, Piscataway, NJ 08855
Telephone: (732) 562-3966
E-Mail: copyrights@ieee.org
FAX: (732) 981-8062

VITA

Allen Hagerman Reed was born in Lynn, Massachusetts, on 9 November 1962, to Catherine Ellis Hagerman Reed and Allen Eugene Reed Junior. He graduated from Westminster High School, in Simsbury, Connecticut, in 1981. He then graduated from Gordon College, in Wenham, Massachusetts, in 1985, where he earned a Bachelor of Arts in biblical studies. He took a hiatus from his educational pursuits as he trekked in the Appalachian Mountains of Northern New York and the Sierra Nevada of Eastern California. Following this hiatus, he attended Humboldt State University where he graduated with a Bachelor of Science in oceanography in 1996. He then ventured to his mother's childhood state and graduated from her alma mater, the University of Southern Mississippi, with a Master of Science degree in marine geology in 1999. While attending USM he worked for the Naval Research Laboratory at Stennis Space Center. NRL committed to paying for his education at Louisiana State University in a quid pro quo agreement. He receives the degree of Doctor of Philosophy from the Department of Oceanography and Coastal Sciences. He continues to work at NRL as a geologist. His principle task is to develop research applications of microComputed Tomography to marine geosciences. He has a wonderful wife, Catherine Ann Ruland, a fantastically curious and creative daughter, Sarah Elisabeth Reed, three cats, one rabbit, eleven chickens, and seven koi. For morale, welfare, and recreation, he partakes in topwater trout fishing while wading off the local beach, crawfish and shrimp boils, oysters and redfish on the half shell, and boat rides in the marsh.